

## ARTICLE

# Cooperative C-H Activation of Pyridine by PBP Complexes of Rh and Ir Can Lead to Bridging 2-Pyridyls with Different Connectivity to the B-M Unit

Received 00th January 20xx,  
Accepted 00th January 20xx

DOI: 10.1039/x0xx00000x

Yihan Cao<sup>a</sup>, Wei-Chun Shih<sup>a</sup>, Nattamai Bhuvanesh<sup>a</sup>, Jia Zhou<sup>b\*</sup> and Oleg V. Ozerov<sup>a\*</sup>

Pyridine and quinoline undergo selective C-H activation in the 2-position with Rh and Ir complexes of a boryl/bis(phosphine) PBP pincer ligand, resulting in a 2-pyridyl bridging the transition metal and the boron center. Examination of this reactivity with Rh and Ir complexes carrying different non-pincer ligands on the transition metal led to the realization of the possible isomerism derived from the 2-pyridyl fragment connecting either via B-N/C-M bonds or via B-C/N-M bonds. This M-C/M-N isomerism was systematically examined for four structural Types. Each of these types has a defined set of ligands on Rh/Ir besides 2-pyridyl and PBP. A pair of M-C/M-N isomers for each type was computationally examined for Rh and for Ir, totaling 16 compounds. Several of these compounds were isolated or observed in solution by experimental methods, in addition to a few 2-quinolyl variants. The DFT predictions concerning the thermodynamic preference within each M-C/M-N isomeric match the experimental findings very well. In two cases where DFT predicts <2 kcal/mol difference in free energy, both isomers were experimentally observed in solution. Analysis of the structural data, of the relevant Wiberg bond indices, and of the ETS-NOCV partitioning of the interaction of the 2-pyridyl fragment with the rest of the molecule points to the strength of the M-C(pyridyl) bond as the dominant parameter determining the relative M-C/M-N isomer favorability. This M-C bond is always stronger for the analogous Ir vs Rh compounds, but the nature of the ligand *trans* to it has a significant influence, as well.

## Introduction

Selective C-H activation and functionalization of pyridines and other azines presents special challenges, in part because these heterocycles can function as good ligands towards many transition metals.<sup>1,2</sup> Selectivity for the 3- (or *meta*-) position is more common with transition metals,<sup>35</sup> but studies of selective 2-position functionalization are also known.<sup>612</sup> In many specific cases, the scope may be limited, and a particular substitution pattern on the azine is often required for selectivity.

In 2017, we reported a new approach to the directed activation of C-H bonds in pyridine derivatives using an Ir system supported by a boryl/bis(phosphine) PBP<sup>13</sup> pincer<sup>14,15</sup> ligand.<sup>16</sup> The binding of the pyridine (or quinoline) nitrogen to the Lewis acidic boryl site directs Ir to the 2-position in the heterocycle. This approach is distinct from the more classical directed C-H activation, where the directing group donor binds to the same atom (transition metal) which effects C-H cleavage (Figure 1).<sup>17-21</sup> Pyridine derivatives have played a prominent role in the development of classical directed C-H activation,<sup>19,20</sup> but they

typically direct the metal not to the C-H bonds of the pyridine ring itself, but to the more remote C-H bonds in a substituent, such as in the 2-phenyl group. We reasoned that the (PBP)Ir system preferred the C-H activation of the pyridine ring because of the favorability of the Ir/C/N/B trapezoidal four-membered ring formation.<sup>16</sup> Some of the aspects of the mechanism of pyridine activation in our PBP system were recently studied computationally by Ke and coworkers.<sup>22</sup> A similar selectivity was observed by Nakao et al. in the C-H activation of pyridines with a Rh complex<sup>23</sup> supported by a closely related aluminy/bis(phosphine) PAIP pincer (Figure 1).<sup>24,25</sup> Given Nakao's precedent with Rh, we wished to explore the reactivity with pyridine using the (PBP)Rh system,<sup>26,27</sup> as well as the variations of the Rh and Ir systems with and without the carbonyl ligand. While exploring the analogous reactivity with (PBP)Rh, we came across an unexpected finding. As with Ir, C-H activation of pyridine resulted in the formation of a 2-pyridyl that is bridging the B-Rh bond. However, the connectivity was reversed, with C of the pyridyl attached to B and the N atom of the pyridyl attached to Rh. This prompted us to explore this M-C/M-N isomerism in more systematic detail, as it does not appear to have been considered in the literature. This report describes our analysis of the isomeric preference of the 2-pyridyl (or 2-quinolyl) fragment bridging the B-Ir or B-Rh bond in a series of compounds supported by the PBP pincer.

<sup>a</sup> Department of Chemistry, Texas A&M University, 3255 TAMU, College Station, Texas 77842, USA.

<sup>b</sup> State Key Laboratory of Urban Water Resource and Environment, Harbin Institute of Technology, Harbin 150090, China

Electronic Supplementary Information (ESI) available: experimental details and pictorial NMR spectra, details of the computational studies and the coordinate files. Crystallographic information: CCDC 2014200, 2014201, 2014203-2014205. See DOI: 10.1039/x0xx00000x

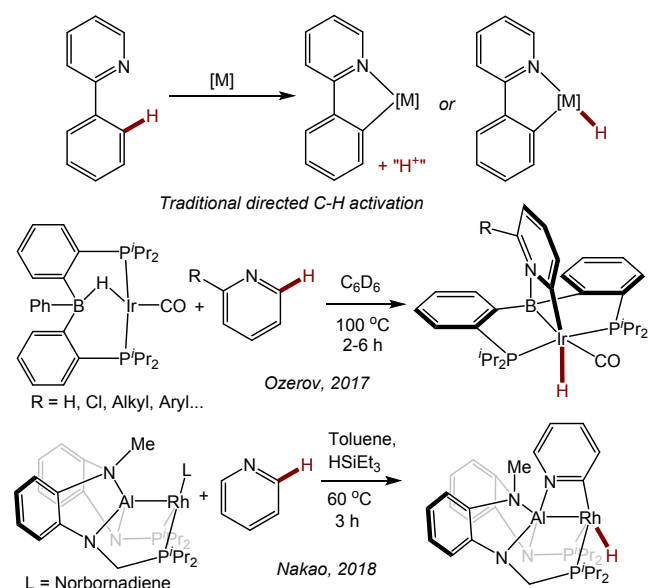


**Figure 1.** Traditional directed C-H activation of 2-phenylpyridine (top) and boryl- or aluminyl-directed C-H activation of the 2-position of a pyridine ring.

## Results and Discussion

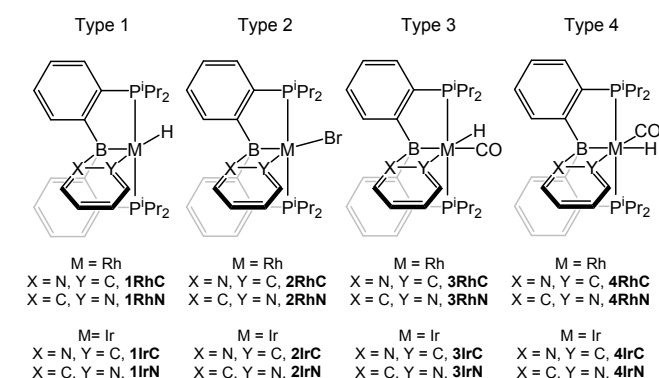
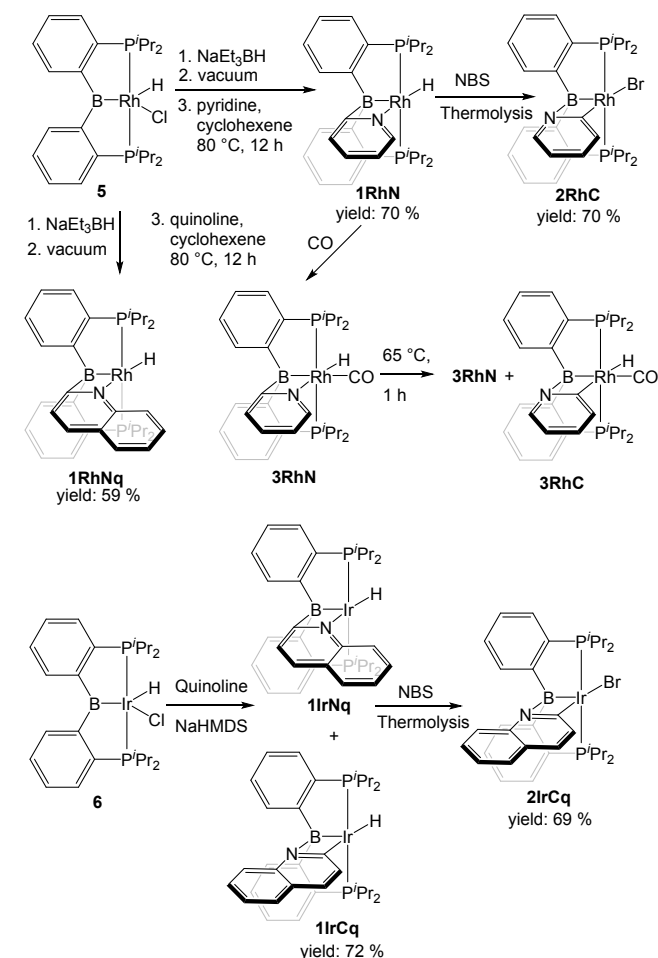


**Figure 2.** The four structural types under study in this work.

### Compounds under consideration and nomenclature

We selected four structural types for analysis (Figure 2). For each type, we considered M-C/M-N isomerism for the Rh and for the Ir version, resulting in sixteen 2-pyridyl compounds that were whose structures were optimized computationally. The compound labels (Figure 2) are derived from the general type (numeral) and the bond present between the metal (Rh or Ir) and C or N. Some of these compounds were isolated or observed experimentally in this (Scheme 1) or the previous report.<sup>16</sup> In addition, we synthesized a few 2-quinolyl analogs of the 2-pyridyl compounds (Scheme 1); they are denoted by adding a “q” to the compound label. The Type 3 and Type 4 compounds are isomeric. We did not attempt the syntheses of the Type 4 compounds because DFT calculations indicated that they are considerably higher in energy than the corresponding Type 3 isomers (vide infra).



**Scheme 1.** Synthesis of (PBP)Rh/Ir pyridyl complexes

### Synthesis of Rh and Ir complexes

In order to access a Rh species capable of C-H activation, the previously reported **5** was treated with NaEt<sub>3</sub>BH followed by the removal of volatiles. Although the stoichiometry suggests the formation of “(PBP)RhH<sub>2</sub>”, we have not established the nature of the resultant species; from the in-situ NMR observations, it appears that a mixture of a few complexes forms (Figure S1). Nonetheless, thermolysis of this mixture in the presence of cyclohexene and either pyridine or quinoline led to the formation of complexes **1RhN** and **1RhNq**, with an isolated yield of 70% and 59% respectively. The corresponding Type 1 Ir compound **1IrCq** was prepared by the treatment of (PBP)IrHCl with NaN(SiMe<sub>3</sub>)<sub>2</sub> in the presence of quinoline. Compound **1IrCq** exists in equilibrium with the minor isomer **1IrNq** (1.00:0.055 ratio at 25 °C and 1.00:0.095 at 65 °C). Attempts to prepare **1IrC** in a pure form were not successful. Unlike **1RhN**, **1IrC** appears to bind an extra equivalent of pyridine, which resulted in a mixture of products when one equiv. of pyridine was used. Utilization of 3 equiv. of pyridine permitted observation of the pyridine adduct of **1IrC** as the dominant product by NMR spectroscopy, but we did not pursue its isolation in a pure solid form (compound **7**, Figure S4). The conversion of the hydride complexes **1RhN** and **1IrCq** to the bromide derivatives **2RhC** and **2IrCq** was effected by

thermolysis with NBS. Good isolated yields (70% and 69% respectively) were obtained after workup. No evidence of the presence of **2RhN** or **2IrNq** was noted.

The carbonyl adduct **3RhN** was prepared by exposure of **1RhN** to carbon monoxide and characterized in situ in solution after 10 min. After removing carbon monoxide under vacuum, thermolysis of the solution of **3RhN** in C<sub>6</sub>D<sub>6</sub> for 1 h at 65 °C resulted in the formation of a mixture of **3RhN** and **3RhC** in a 1.0:0.08 ratio. Extended thermolysis for 24 h at 65 °C led to the formation of multiple complexes along with **3RhN** and **3RhC**, but in that mixture **3RhN** was still present in a much higher concentration than **3RhC**. The synthesis of the analogous Ir complex **3IrC** was previously reported. The synthesis involved extended thermolysis at 100 °C and no evidence of the presence of **3IrN** was noted.

### Spectroscopic characterization

The compounds explored in this study are rich in NMR active nuclei (<sup>1</sup>H, <sup>13</sup>C, <sup>31</sup>P, <sup>11</sup>B, and <sup>103</sup>Rh). All of the compounds possess C<sub>s</sub>-symmetry on the NMR time scale. The M-C/M-N isomers can be distinguished based on the relative <sup>1</sup>H NMR chemical shift of the Rh/Ir-H signal. Since N of pyridyl is less *trans*-influencing than C of 2-pyridyl, a hydride *trans* to N appears at a more upfield frequency vs a hydride *trans* to C. For the Rh compounds **1RhN**, **1RhNq**, and **3RhN** with a hydride *trans* to N, its <sup>1</sup>H NMR chemical shift falls into a narrow range of -15.7 to -17.3 ppm, but for **3RhC**, the hydride resonates considerably upfield at δ -11.04 ppm. The contrast is even greater for the Ir pair **1IrCq** (δ -0.20 ppm) and **1IrNq** (δ -17.10 ppm).

The shape of the <sup>13</sup>C{<sup>1</sup>H} NMR resonance corresponding to the boron- or metal-bound carbon of the 2-pyridyl or 2-quinolyl unit is also telling. In compounds **1RhN**, **1RhNq**, and **3RhN**, this carbon is bound to boron and the corresponding <sup>13</sup>C NMR resonances in these compounds possess some broadness. In compounds **RhBr-C** and **IrH-Cq**, this carbon is bound to the metal and displays coupling to the two equivalent <sup>31</sup>P nuclei, as well as to <sup>103</sup>Rh in **RhBr-C**.

**Table 1.** Selected NMR chemical shift data (in ppm, C<sub>6</sub>D<sub>6</sub>, solvent) for the experimentally observed complexes of types 1-3.

Complexes	Rh/Ir-H	<sup>11</sup> B{ <sup>1</sup> H}	Ir/Rh-C	B-C
<b>1RhN</b>	-17.25	3.5	/	188.2
<b>1RhNq</b>	-16.81	4.5	/	189.5
<b>1IrCq</b>	-0.20	-8.5	201.3	/
<b>1IrNq</b>	-17.10	/ <sup>d</sup>	/	/ <sup>d</sup>
<b>2RhC</b>	/	1.7	178.0	/
<b>2IrCq<sup>e</sup></b>	/	-6.8	176.9	/
<b>3RhN</b>	-15.69	2	/	193.5
<b>3RhC</b>	-11.04	/ <sup>d</sup>	/ <sup>d</sup>	/
<b>3IrC</b>	-14.15		164.9	

<sup>a</sup> <sup>1</sup>H NMR chemical shift of the metal-bound hydride. <sup>b</sup> <sup>13</sup>C NMR chemical shift of the metal-bound carbon. <sup>c</sup> <sup>13</sup>C NMR chemical shift of the boron-bound carbon in the bridging pyridyl or quinolyl. <sup>d</sup> Resonance was not observed due to low concentration. <sup>e</sup> Spectra of **2IrCq** were recorded in CDCl<sub>3</sub>.

### XRD structural characterization

Single crystal X-ray diffractometry permitted the determination of the solid-state structures of **1RhN**, **1RhNq**, **1IrCq**, **2RhC**, and **3RhN**. The solid-state structure of **3IrC** was reported in 2017. The Ir-B (2.209 (2) and 2.195 (2) Å) and the Ir-C distances (2.034(3) and 2.029(3) Å) in the two crystallographically independent molecules of **1IrCq** are slightly shorter than the Ir-B distance of 2.285(2) Å and the Ir-C distance of 2.079(2) Å in the previously reported **3IrC**. The B-N and N-C distances in these molecules are very similar. Comparing the Rh-B distances in **1RhN** (2.229(2) Å) and **3RhN** (2.319(1) Å) also shows that the presence of CO is correlated with the elongation of the M-B bond (*trans* to CO) by almost 0.1 Å. However, the Rh-N distances (2.163(1) Å in **1RhN** and 2.158(1) Å in **3RhN**) seem to be unaffected by the presence of the CO ligand.

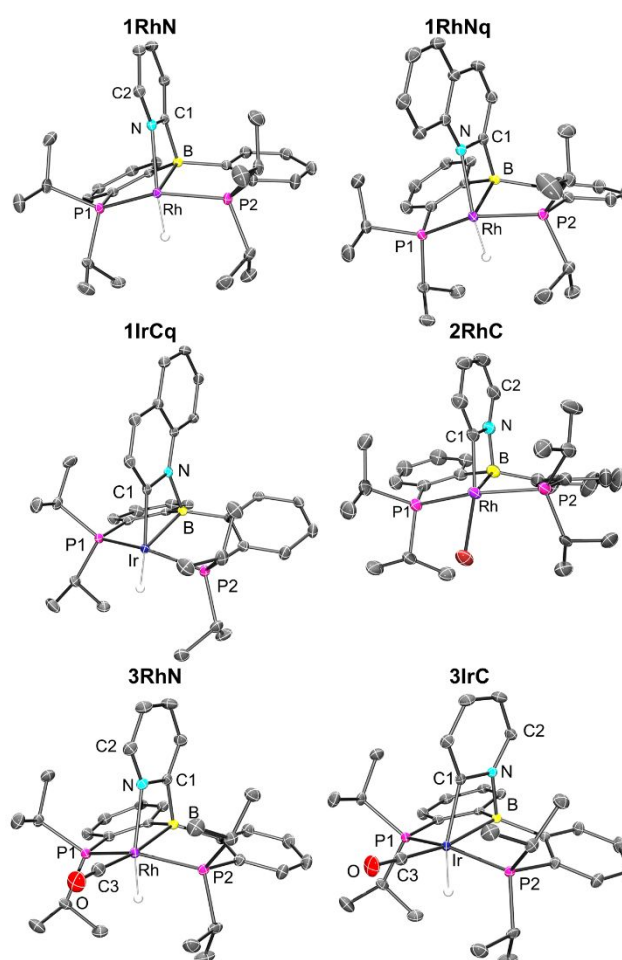


**Figure 3.** POV-Ray rendition of the ORTEP drawing (50% thermal ellipsoids) of **1RhN**, **1RhNq**, **1IrCq**, **2RhC**, and **3RhN** showing selected atom labelling. Hydrogen atoms, disorders of <sup>1</sup>Pr groups in **1IrCq** and **2RhC** crystals, and solvent molecules (toluene) in **1RhNq** and **1IrCq** crystals are omitted for clarity. Only one of the **1IrCq** in the asymmetric unit is shown in the ORTEP drawing above.

The values for the sum of angles that exclude the pyridyl/quinolyl nitrogen about the boron atom in **1RhN**, **1RhNq** and **3RhN** are in the ca. 339.4°-343.8° range. The range of the corresponding values (excluding the pyridyl/quinolyl carbon) in **1IrCq**, **2RhC** and **3IrC** is ca. 335.6°-341.9°. Likewise, the P-M-P angles in the six structures in Figure 3 all fall within the ca. 151-

161° range. Thus, while there are significant differences in the metrics of the M-C/N-B cycle among the six structures, the conformation of the (PBP)M fragment is close to constant. The hydride ligand in **1RhN**, **1RhNq**, **1IrCq**, **3RhN**, and **3IrC** is close to being *trans* to either C or N of the pyridyl (161–174° angle range). In the structure of **2RhC**, the C-Rh-Br angle deviates from linearity to a greater extent (149.57(11)°) and **2RhC** can be viewed as adopting a Y-shaped geometry as opposed to square-pyramidal for the five-coordinate hydride complexes **1RhN**, **1RhNq**, **1IrCq**.<sup>28</sup>

### DFT studies

The structures of the 16 molecules shown in Figure 2 were optimized using the B97D3/LANL2DZ/6-31G(d) method (see details in the SI). Figure 4 summarizes the results of the calculations, showing the Wiberg bond indices (WBI) within the four-membered rings, as well as the calculated free energies of the isomerization from the M-C to the M-N isomer. The metric details of the DFT-optimized geometries matched those from the XRD structures reasonably well.

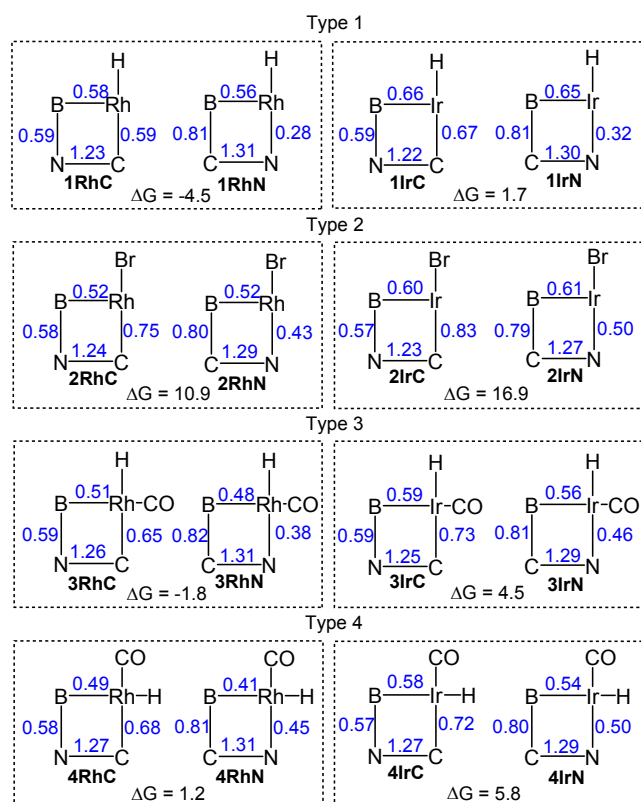


**Figure 4.** DFT-calculated Wiberg bond indices shown in blue for the bonds within the four-membered metallacycle.  $\Delta G_{298}$  values (in kcal/mol) are given for the isomerization from left to right within each box (negative  $\Delta G$  value favors the isomer with the M-N bond).

Calculations indicate that the isomers with the carbon bound to the transition metal are more favorable for all Ir complexes and for the Rh complexes of Types 2 and 4. For the other Rh complexes, the isomer with the nitrogen bound to Rh is preferred. Across all four types, the relative free energy

preference of Ir for the metal-carbon bonded isomer is very consistently 5–7 kcal/mol higher than that of Rh.

Overall, the calculated thermodynamic parameters are consistent with the experimental observations we have for the Rh and Ir compounds of Types 1–3. Moreover, the calculated free energy preferences for **1IrC** (over **1IrN**) and for **3RhN** (over **3RhC**) are <2 kcal/mol, suggesting that both isomers in these two pairs should be present at observable concentrations. This is precisely what we observed for **1IrCq/1IrNq** and for **3RhN/3RhC** (*vide supra*), with the isomer predicted to be more favorable by DFT present in a higher proportion.

Type 3 (CO *trans* to B) compounds are isomeric to Type 4 (H *trans* to B), and DFT calculations predict that any of the four Type 3 compounds (**3IrC**, **3IrN**, **3RhC**, **3RhN**) is lower in free energy than their corresponding Type 4 analog (**4IrC**, **4IrN**, **4RhC**, **4RhN**, respectively) by 13–19 kcal/mol. This is consistent with the lack of observation of **4RhC** or **4RhN** in the thermolysis of the **3RhC/3RhN** mixture.

The calculated Wiberg bond indices (WBI) allow a way to analyze the changes in the nature of the bonds in the four-membered cycle for the pairs of isomers. The WBI for the M-B bond in any Ir compound is 0.08–0.13 higher than for the exact Rh analog. Higher WBI values in Ir (vs Rh) compounds are also notable for the M-C and M-N bonds (by 0.04–0.08). This is in general expected for a 5d metal (Ir) compared to its 4d congener (Rh).

Within each M-C/M-N isomeric pair with the same metal, the M-B bond WBI values differ only by 0.04 or less, except for the **4RhC/4RhN** pair (0.08 difference). The WBI vary even less for the C-B bonds (0.79–0.82 range) and for the N-B bonds (0.57–0.59) throughout the whole array of compounds. It can be concluded that the changes in the M-B, C-B, and N-B bonding contribute little to the thermodynamic preferences for the M-C vs M-N isomers.

The WBI values for the CN bond vary within a range of 1.22–1.31 for all 16 compounds. Within every M-C/M-N isomeric pair, this value is higher for the N-M bound isomer, by 0.02–0.08, suggesting that coordination to Ir or Rh strengthens the C-N bond slightly, but to a similar degree across all four types of compounds.

Considering the M-C bonds, there appears to be a surprisingly linear correlation (Figure 5) between the WBI values and the thermodynamic isomeric preference, that covers both the Rh and the Ir examples. Higher M-C WBI corresponds to higher preference for the M-C isomer, with ergoneutrality of the isomerization predicted at ca. 0.65 M-C WBI. The WBI values of the M-N bonds trend in the same direction. However, the correlation is more diffuse and not as steep, likely reflecting the intrinsically weaker nature of the M-N bond and its lesser dependence on the environment about the metal center (see Figure S5).

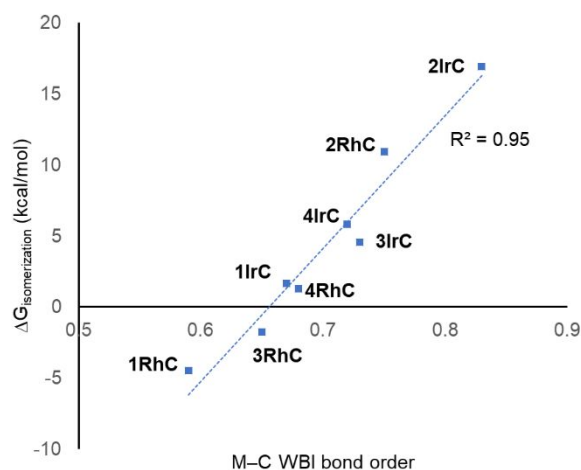


**Figure 5.** Correlation between the free energy of isomerization and the M-C WBI values for compounds under study.

These observations lead us to conclude that the main factor controlling the thermodynamics of the M-C/M-N isomerization is the quality of the M-C bond, or in other words, the capacity of the metal site for making the strongest M-C bond. This capacity is always greater for Ir than for Rh, but it is also strongly influenced by the nature of the ligand *trans* to C. A hydride *trans* to C (Types 1 and 3) is a maximal *trans*-influence conflict, leading to the weakest M-C bonds. A bromide *trans* to C (type 2) is much less *trans*-influencing than a hydride, leading to the strongest M-C bonds. A carbonyl ligand *trans* to C (Type 4) represents an intermediate situation. Type 3 can be viewed as Type 1 with additional CO ligand coordinated; apparently, CO coordination increases the M-C bond strength and therefore the preference for the M-C bound isomer. Notably, the WBI for the Rh-C bond in **2RhC** is higher than the WBI values for all the Ir complexes except **2IrC**, meaning that the weak *trans*-influence of Br (vs H or CO) can strengthen the M-C bond *trans* to it to a degree that can overcome the 4d/5d metal handicap. We have also analyzed the bonding using the extended-transition-state natural orbitals for chemical valence (ETS-NOCV) partitioning of the interaction of the closed shell 2-pyridyl anionic fragment with the formally cationic (PBP)Ir framework (see details in the SI). The findings dovetailed the WBI analysis: greater energy of interaction was calculated for 1) Ir vs Rh, 2) M-C vs M-N isomers, and 3) for Type 2 vs the other Types.

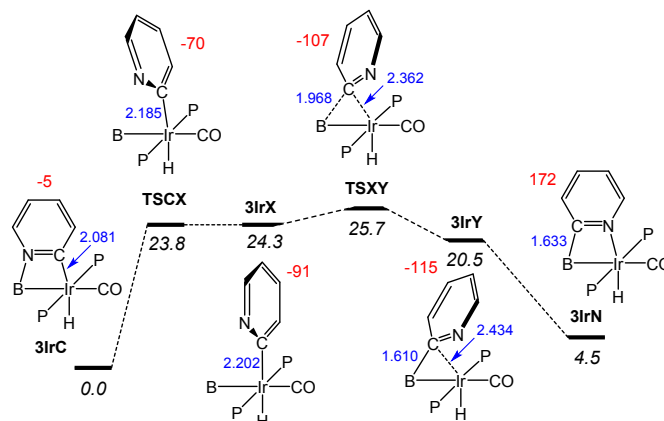


**Figure 6.** Calculated reaction coordinate for the isomerization of **3IrC** into **3IrN**. The relative free energy values in kcal/mol are given in italics. The numbers in blue (in Å) show the B-C and Ir-C distances while the numbers in red show the values (in °) for the dihedral angles N-C-Ir-B.

Next, we examined the mechanism<sup>29</sup> of the interconversion between **3IrC** and **3IrN** as a representative example (Figure 6). From **3IrC**, the reaction proceeds via dissociation of the pyridine N from B with concomitant ca. 90° rotation about the Ir-C bond, resulting in **3IrX**. The structure of the intermediate **3IrX** evinces no bonding interactions between the pyridyl fragment and B, but a full-fledged Ir-C bond. The transition state connecting it with **3IrC** (**TSCX**) possesses both a similar energy and geometry, with an incomplete rotation. The migration of the pyridyl from Ir in **3IrX** to B in intermediate **3IrY** proceeds via **TSXY**. In **3IrY**, the pyridyl C is connected to the B by means of well-developed C-B bond, which is even 0.023 Å shorter than the calculated C-B distance in **3IrN**. The pyridyl C in **3IrY** can also be viewed as weakly interacting with Ir. We did not locate a transition state for the conversion of **3IrY** into **3IrN**; this process is also simply a rotation of the pyridyl with coordination to Ir. It is clear that most of the barrier for the interconversion between **3IrC** and **3IrN** is owing to the dissociation of N from B/Ir, corresponding to the rotation of N away from B/Ir. Once the N is free, the barrier for the migration of the C-pyridyl between B and Ir is only a few kcal/mol. This likely also applies to the other Types presented in this paper.

## Conclusion

In summary, we have examined the unusual isomerization of a bridging 2-pyridyl unit in an array of Rh and Ir complexes supported by a PBP pincer ligand. The main factor governing the thermodynamic preference appears to be the strength of the M-C bond in the M-C bonded isomer. It was observed that the thermodynamic preference for the M-N vs M-C bond depends both on the nature of the metal center and on the nature of the ligand *trans* to the M-N/M-C bond. The M-C isomer is favored for the 5d metal Ir vs Rh and by the presence of a more weakly *trans*-influencing ligand *trans* to the M-N/M-C bond. For some of the complexes, both isomers were observed experimentally, in close agreement with theoretical analysis. The interconversion between isomers of similar



thermodynamic stability appears to be easily accessible on the experimental timescale, consistent with the computational analysis of a representative system. These findings suggest that the possibility of M-C/M-N isomerization of 2-pyridyl and other closely related fragments should be taken into account when investigating C-H bond activation in azines using a combination of a late transition metal and an embedded main group Lewis acid.

## Conflicts of interest

There are no conflicts to declare.

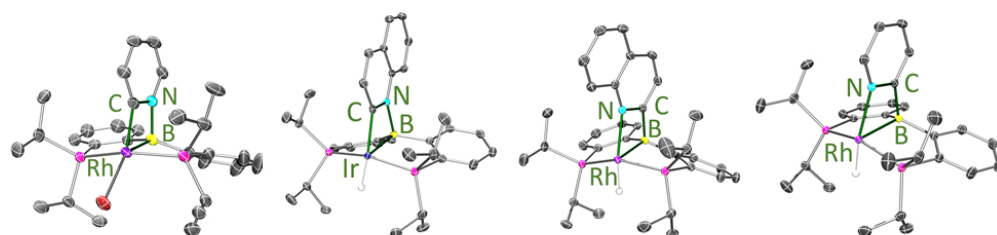
## Acknowledgements

We are grateful for the support of this work by the US National Science Foundation (grant CHE-2102095). This work was also supported by Open Project of State Key Laboratory of Urban Water Resource and Environment, Harbin Institute of Technology (No. QA202009). Computer time made available by the National Supercomputing Center of China in Shenzhen (Shenzhen Cloud Computing Center) is gratefully acknowledged. We thank R. A. Gholson for assistance with manuscript formatting.

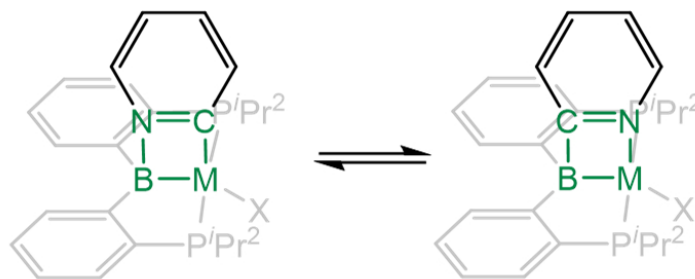
## Notes and references

- <sup>1</sup> Y. Nakao, *Synthesis*, 2011, **2011**, 3209–3219.
- <sup>2</sup> K. Murakami, S. Yamada, T. Kaneda and K. Itami, *Chem. Rev.*, 2017, **117**, 9302–9332.
- <sup>3</sup> J. C. Lewis, R. G. Bergman and J. A. Ellman, *J. Am. Chem. Soc.*, 2007, **129**, 5332–5333.
- <sup>4</sup> B.-T. Guan and Z. Hou, *J. Am. Chem. Soc.*, 2011, **133**, 18086–18089.
- <sup>5</sup> G. Tran, K. D. Hesp, V. Mascitti and J. A. Ellman, *Angew. Chem. Int. Ed.*, 2017, **56**, 5899.
- <sup>6</sup> H.-Q. Do and O. Daugulis, *J. Am. Chem. Soc.*, 2011, **133**, 13577–13586.
- <sup>7</sup> A. M. Berman, J. C. Lewis, R. G. Bergman and J. A. Ellman, *J. Am. Chem. Soc.*, 2008, **130**, 14926–14927.
- <sup>8</sup> M. Li and R. Hua, *Tetrahedron Lett.*, 2009, **50**, 1478–1481.
- <sup>9</sup> I. B. Seiple, S. Su, R. A. Rodriguez, R. Gianatassio, Y. Fujiwara, A. L. Sobel and P. S. Baran, *J. Am. Chem. Soc.*, 2010, **132**, 13194–13196.
- <sup>10</sup> J. Wen, S. Qin, L.-F. Ma, L. Dong, J. Zhang, S.-S. Liu, Y.-S. Duan, S.-Y. Chen, C.-W. Hu and X.-Q. Yu, *Org. Lett.*, 2010, **12**, 2694–2697.
- <sup>11</sup> M. Tobisu, I. Hyodo and N. Chatani, *J. Am. Chem. Soc.*, 2009, **131**, 12070–12071.
- <sup>12</sup> C. Yin, K. Zhong, W. Li, X. Yang, R. Sun, C. Zhang, X. Zheng, M. Yuan, R. Li, Y. Lan, H. Fu and H. Chen, *Adv. Synth. Cat.*, 2018, **360**, 3990–3998.
- <sup>13</sup> For the reports on other boryl-centered pincer complexes, see: (a) Y. Segawa, M. Yamashita and K. Nozaki, *J. Am. Chem. Soc.*, 2009, **131**, 9201–9203. (b) T.-P. Lin and J. C. Peters, *J. Am. Chem. Soc.*, 2014, **136**, 13672–13683. (c) A. F. Hill and C. M. A. McQueen, *Organometallics*, 2014, **33**, 1977–1985. (d) E. H. Kwan, Y. J. Kawai, S. Kamakura and M. Yamashita, *Dalton Trans.*, 2016, **45**, 15931–15941. (e) A. M. Spokoyny, M. G. Reuter, C. L. Stern, M. A. Ratner, T. Seideman and C. A. Mirkin, *J. Am. Chem. Soc.*, 2009, **131**, 9482–9483. (f) M. E. El-Zaria, H. Arai and H. Nakamura, *Inorg. Chem.*, 2011, **50**, 4149–4161. (g) B. J. Eleazer, M. D. Smith, A. A. Popov and D. V. Peryshkov, *J. Am. Chem. Soc.*, 2016, **138**, 10531–10538. (h) D. Schuhknecht, F. Ritter and M. E. Tauchert, *Chem. Commun.*, 2016, **52**, 11823–11826.
- <sup>14</sup> ed. G. Van Koten, and D. Milstein, *Organometallic Pincer Chemistry*. Springer: Heidelberg, 2013.
- <sup>15</sup> E. Peris and R. H. Crabtree, *Chem. Soc. Rev.*, 2018, **47**, 1959–1968.
- <sup>16</sup> W.-C. Shih and O. V. Ozerov, *J. Am. Chem. Soc.*, 2017, **139**, 17297–17300.
- <sup>17</sup> V. Snieckus, *Chem. Rev.*, 1990, **90**, 879–933.
- <sup>18</sup> S. Murai, F. Kakiuchi, S. Sekine, Y. Tanaka, A. Kamatani, M. Sonoda and N. Chatani, *Nature*, 1993, **366**, 529–531.
- <sup>19</sup> T. W. Lyons and M. S. Sanford, *Chem. Rev.*, 2010, **110**, 1147–1169.
- <sup>20</sup> M. Zhang, Y. Zhang, X. Jie, H. Zhao, G. Li, G. and W. Su, *Org. Chem. Front.*, 2014, **1**, 843–895.
- <sup>21</sup> J. He, M. Wasa, K. S. L. Chan, Q. Shao and J.-Q. Yu, *Chem. Rev.*, 2017, **117**, 8754–8786.
- <sup>22</sup> J. Liu, Y. Li, J. Jiang, Y. Liu, and Z. Ke, *ACS Catalysis*, 2021, **11**, 6186–6192.
- <sup>23</sup> N. Hara, T. Saito, K. Semba, N. Kuroakose, H. Zheng, S. Sakaki and Y. Nakao, *J. Am. Chem. Soc.*, 2018, **140**, 7070–7073.

- <sup>24</sup> I. Fujii, K. Semba, Q.-Z. Li, S. Sakaki and Nakao, *J. Am. Chem. Soc.*, 2020, **142**, 11647-11652.
- <sup>25</sup> Q.-Z. Li, N. Hara and S. Sakaki, *Inorg. Chem.*, 2020, **59**, 15862-15876.
- <sup>26</sup> W.-C. Shih, W. Gu, M. C. MacInnis, S. D. Timpa, N. Bhuvanesh, J. Zhou and O. V. Ozerov, *J. Am. Chem. Soc.*, 2016, **138**, 2086-2089.
- <sup>27</sup> W.-C. Shih, W. Gu, M. C. MacInnis, D. E. Herbert and O. V. Ozerov, *Organometallics*, 2017, **36**, 1718-1726.
- <sup>28</sup> J.-F. Riehl, Y. Jean, O. Eisenstein and M. Pelissier, *Organometallics*, 1992, **11**, 729-737.
- <sup>29</sup> A part of the sequence presented in Figure 6 was also calculated by Ke et al. (ref 22), while considering other processes. The sequence **3IrC-TSCX-3IrX-TSXY-3IrY** in Figure 6 corresponds to PC-TS6-B-IM5-B-TS5-B-IM4-B in the paper by Ke et al. They did not consider **3IrN**. The calculations by Ke et al. resulted in lower barriers relative to **Ir3C**; this is likely owing to a combination of a different chosen functional and basis set, continuum model solvation and a different isopropyl group conformation chosen in the work by Ke et al.



M–C vs M–N  
Isomerism



82x44mm (300 x 300 DPI)



# Supporting Information

## Cooperative C-H Activation of Pyridine by PBP Complexes of Rh and Ir Can Lead to Bridging 2- Pyridyls with Different Connectivity to the B-M Unit

Yihan Cao<sup>a</sup>, Wei-Chun Shih<sup>a</sup>, Nattamai Bhuvanesh<sup>a</sup>, Jia Zhou<sup>b\*</sup> and Oleg V.

Ozerov<sup>a\*</sup>

<sup>a</sup> Department of Chemistry, Texas A&M University, 3255 TAMU, College Station, TX 77842.

<sup>b</sup> State Key Laboratory of Urban Water Resource and Environment, Harbin Institute of  
Technology, Harbin 150090, China.

[ozarov@chem.tamu.edu](mailto:ozarov@chem.tamu.edu), [jiazhou@hit.edu.cn](mailto:jiazhou@hit.edu.cn)

**Table of Contents.**

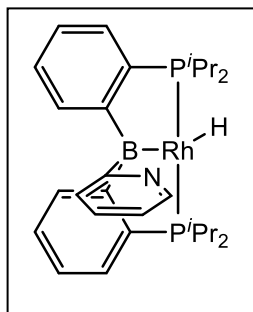
<b>1. General Considerations.</b>	<b>S3</b>
<b>2. Synthesis and Characterization of Rhodium and Iridium Complexes.</b>	<b>S4</b>
<b>3. X-Ray Structural Determination Details.</b>	<b>S16</b>
<b>4. DFT Calculations.</b>	<b>S22</b>
<b>5. NMR Spectra.</b>	<b>S32</b>
<b>6. SI References.</b>	<b>S63</b>

## 1. General Considerations.

**General Considerations.** Unless specified otherwise, all manipulations were performed under an Ar atmosphere using standard Schlenk line or glovebox techniques. Toluene and pentane were dried and deoxygenated (by purging) using a solvent purification system (Innovative Technology Pure Solv MD-5 Solvent Purification System) and stored over molecular sieves in an Ar-filled glove box.  $C_6D_6$  and  $CDCl_3$  was dried over NaK/ $Ph_2CO$ /18-crown-6, distilled and stored over molecular sieves in an Ar-filled glovebox. Pyridine derivatives and cyclohexene were dried over  $CaH_2$ , vacuum transferred and stored over molecular sieves in an Ar-filled glove box. (PBP)RhHCl (**5**) and (PBP)IrHCl (**6**) were prepared via literature procedures.<sup>1</sup> All other chemicals were used as received from commercial vendors.

**Physical Methods.** NMR spectra were recorded on Mercury 300 ( $^1H$  NMR, 299.952 MHz;  $^{31}P$  NMR, 121.422 MHz), Bruker 400MHz ( $^{11}B$  NMR, 128.185 MHz,  $^1H$  NMR, 399.535 MHz;  $^{31}P$  NMR, 161.734 MHz) and Varian Inova 500 ( $^1H$  NMR, 499.703 MHz;  $^{13}C$  NMR, 125.697 MHz;  $^{31}P$  NMR, 202.265 MHz) spectrometer. Chemical shifts are reported in  $\delta$  (ppm). For  $^1H$  and  $^{13}C$  NMR spectra, the residual solvent peak was used as an internal reference ( $^1H$  NMR:  $\delta$  7.16 for  $C_6D_6$ ,  $\delta$  7.26 for  $CDCl_3$ ,  $^{13}C$  NMR:  $\delta$  128.06 for  $C_6D_6$ ,  $\delta$  77.2 for  $CDCl_3$ ).  $^{11}B$  NMR spectra were referenced externally with  $BF_3$  etherate at  $\delta$  0.  $^{31}P$  NMR spectra were referenced externally with 85% phosphoric acid at  $\delta$  0. FT-IR spectra were recorded on an Agilent Cary 630 ATR-IR spectrometer in a glovebox. Elemental analyses were performed by CALI Labs, Inc. (Highland Park, NJ)

## 2. Synthesis and Characterization of Rhodium and Iridium Complexes.



**(PB<sup>Py</sup>P)Rh(H) (1RhN).** In a 50 mL PTFE screw-capped reaction tube, NaEt<sub>3</sub>BH (0.40 mL, 0.40 mmol, 1.0 M in toluene) was added to a toluene solution (5 mL) of **5** (0.22 g, 0.40 mmol). The solution changed color from orange to dark red immediately. After stirring at room temperature for 5 min, a <sup>31</sup>P{<sup>1</sup>H} NMR spectrum was recorded, showing two or more complexes

formed (**Figure S1**). Volatiles were removed under vacuum to remove BEt<sub>3</sub> that was generated. The resulting red solid was directly dissolved in toluene (10 mL), to which were added pyridine (35 μL, 0.44 mmol) and cyclohexene (44 μL, 0.44 mmol). The reaction mixture was stirred at 80 °C for 12 h, and gradually changed from dark-red to brown color. The solution was filtered through Celite, and volatiles were removed under vacuum. The resulting brown solid was recrystallized in toluene/pentane (1:3), yielding a pale-yellow solid (163 mg, 70%).

<sup>1</sup>H NMR (300 MHz, C<sub>6</sub>D<sub>6</sub>): δ 8.46 (d, J<sub>H-H</sub> = 7.5 Hz, 2H, PB<sup>Py</sup>P-*Phenyl*), 8.34 (d, J<sub>H-H</sub> = 4.8 Hz, 1H, PB<sup>Py</sup>P-*Pyridyl*), 7.31 (t, J<sub>H-H</sub> = 7.2 Hz, 2H, PB<sup>Py</sup>P-*Phenyl*), 7.18 (m, 4H, PB<sup>Py</sup>P-*Phenyl*), 6.68 (m, 2H, PB<sup>Py</sup>P-*Pyridyl*), 6.45 (m, 1H, PB<sup>Py</sup>P-*Pyridyl*), 2.29 (m, 2H, CHMe<sub>2</sub>), 1.92 (m, 2H, CHMe<sub>2</sub>), 1.32 (dvt, J<sub>H-H</sub> = J<sub>H-P</sub> = 7.6 Hz, 6H, CHMe<sub>2</sub>), 1.12 (dvt, J<sub>H-H</sub> = J<sub>H-P</sub> = 7.0 Hz, 6H, CHMe<sub>2</sub>), 1.04 (dvt, J<sub>H-H</sub> = J<sub>H-P</sub> = 7.4 Hz, 6H, CHMe<sub>2</sub>), 0.57 (dvt, J<sub>H-H</sub> = J<sub>H-P</sub> = 7.1 Hz, 6H, CHMe<sub>2</sub>), -17.25 (dt, J<sub>H-P</sub> = 18.5 Hz, J<sub>H-Rh</sub> = 22.9 Hz, 1H, Rh-H). <sup>31</sup>P{<sup>1</sup>H} NMR (121 MHz, C<sub>6</sub>D<sub>6</sub>): δ 60.6 (d, J<sub>P-Rh</sub> = 141.4 Hz). <sup>11</sup>B{<sup>1</sup>H} NMR (128 MHz, C<sub>6</sub>D<sub>6</sub>): δ 3.5. <sup>13</sup>C{<sup>1</sup>H} NMR (126 MHz, C<sub>6</sub>D<sub>6</sub>): δ 188.2 (br, Rh-B-C-N), 165.4 (br, B-*Phenyl*), 149.6 (s, *Pyridyl*), 137.9 (td, J<sub>P-C</sub> = 19.8 Hz, J<sub>Rh-C</sub> = 3.5 Hz, P-*Phenyl*), 132.8 (s, *Pyridyl*), 129.9 (t, J<sub>P-C</sub> = 9.9 Hz, *Phenyl*), 129.2 (s, *Phenyl*), 125.1 (t, J<sub>P-C</sub> = 3.1 Hz, *Phenyl*), 122.2 (s, *Pyridyl*), 121.0 (s, *Pyridyl*), 30.0 (t, J<sub>P-C</sub> = 8.3 Hz, CHMe<sub>2</sub>), 27.7 (t, J<sub>P-C</sub> = 14.5 Hz, CHMe<sub>2</sub>), 21.3 (t, J<sub>P-C</sub> = 4.8 Hz, CHMe<sub>2</sub>), 20.4 (t, J<sub>P-C</sub> = 2.1 Hz, CHMe<sub>2</sub>), 20.1 (s, CHMe<sub>2</sub>),

20.0 (t,  $J_{\text{P-C}} = 3.6$  Hz,  $\text{CHMe}_2$ ). Anal. Calc. for  $\text{C}_{29}\text{H}_{41}\text{BNP}_2\text{Rh}$ : C, 60.13; H, 7.13; N, 2.42. Found: C, 60.25; H, 6.97; N, 2.34.

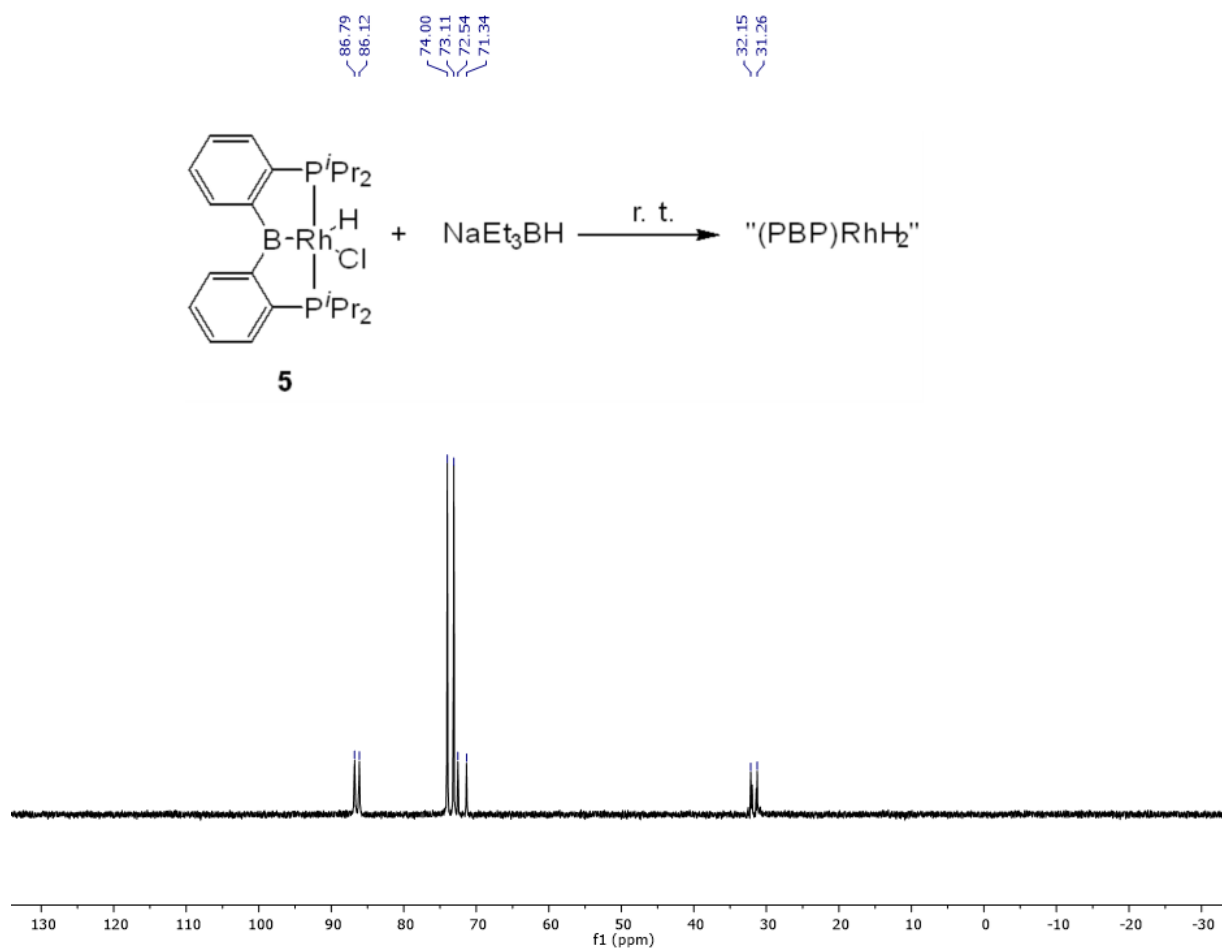
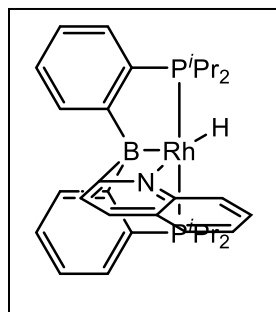


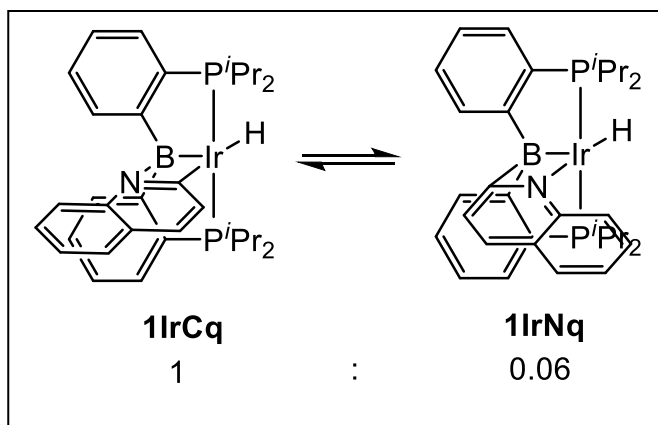
**Figure S1.**  $^{31}\text{P}\{^1\text{H}\}$  NMR spectrum record on a 500 MHz Varian NMR after 1 equiv. of  $\text{NaEt}_3\text{BH}$  were added to **5** in toluene, showing four or more complexes formed.



**(PB<sup>Qu</sup>P)Rh(H) (1RhNq).** In a 50 mL PTFE screw-capped reaction tube,  $\text{NaEt}_3\text{BH}$  (0.52 mL, 0.52 mmol, 1.0 M in toluene) was added to a toluene solution (5 mL) of **5** (0.27 g, 0.50 mmol). The solution changed color from orange to dark-red immediately. After stirring at room temperature for 5 min, volatiles were removed under vacuum to remove  $\text{BEt}_3$  that was

generated. The resulting red solid was dissolved in toluene (10 mL), to which were added quinoline (62  $\mu$ L, 0.52 mmol) and cyclohexene (53  $\mu$ L, 0.52 mmol). The reaction mixture was stirred at 80  $^{\circ}$ C for 12 h, and gradually changed from dark-red to brown color. The solution was filtered through Celite, and volatiles were removed under vacuum. The resulting brown solid was recrystallized in toluene/pentane 1:3, yielding a pale-yellow solid (0.19 g, 59%).

$^1\text{H}$  NMR (400 MHz,  $\text{C}_6\text{D}_6$ ):  $\delta$  8.52 (d,  $J_{\text{H-H}} = 7.5$  Hz, 2H,  $\text{PB}^{\text{Py}}\text{P-Phenyl}$ ), 8.08 (d,  $J_{\text{H-H}} = 8.3$  Hz, 1H,  $\text{PB}^{\text{Qu}}\text{P-Quinoly}$ ), 7.39 (t,  $J_{\text{H-H}} = 7.4$  Hz, 1H,  $\text{PB}^{\text{Qu}}\text{P-Quinoly}$ ), 7.33 (t,  $J_{\text{H-H}} = 7.0$  Hz, 2H,  $\text{PB}^{\text{Py}}\text{P-Phenyl}$ ), 7.15 (m, 6H,  $\text{PB}^{\text{Py}}\text{P-Phenyl}$  &  $\text{Quinoly}$ ), 7.03 (t,  $J_{\text{H-H}} = 7.4$  Hz, 1H,  $\text{PB}^{\text{Qu}}\text{P-Quinoly}$ ), 6.94 (d,  $J_{\text{H-H}} = 8.2$  Hz, 1H,  $\text{PB}^{\text{Qu}}\text{P-Quinoly}$ ), 2.24 (m, 2H,  $\text{CHMe}_2$ ), 1.84 (m, 2H,  $\text{CHMe}_2$ ), 1.37 (dvt,  $J_{\text{H-H}} = J_{\text{H-P}} = 7.5$  Hz, 6H,  $\text{CHMe}_2$ ), 1.06 (m, 12H,  $\text{CHMe}_2$ ), 0.19 (dvt,  $J_{\text{H-H}} = J_{\text{H-P}} = 6.9$  Hz, 6H,  $\text{CHMe}_2$ ), -16.81 (dt,  $J_{\text{H-P}} = 18.5$  Hz,  $J_{\text{H-Rh}} = 23.2$  Hz, 1H,  $\text{Rh-H}$ ).  $^{31}\text{P}\{^1\text{H}\}$  NMR (121 MHz,  $\text{C}_6\text{D}_6$ ):  $\delta$  60.3 (d,  $J_{\text{P-Rh}} = 141.1$  Hz).  $^{11}\text{B}\{^1\text{H}\}$  NMR (128 MHz,  $\text{C}_6\text{D}_6$ ):  $\delta$  4.5.  $^{13}\text{C}\{^1\text{H}\}$  NMR (126 MHz,  $\text{C}_6\text{D}_6$ ):  $\delta$  189.5 (br,  $\text{Rh-B-C-N}$ ), 164.8 (br,  $\text{B-Phenyl}$ ), 148.5 (s,  $\text{Quinoly}$ ), 138.3 (td,  $J_{\text{P-C}} = 19.5$  Hz,  $J_{\text{Rh-C}} = 3.7$  Hz,  $\text{P-Phenyl}$ ), 132.2 (s,  $\text{Quinoly}$ ), 129.8 (t,  $J_{\text{P-C}} = 9.7$  Hz,  $\text{Phenyl}$ ), 129.4 (s,  $\text{Phenyl}$ ), 128.7 (s,  $\text{Quinoly}$ ), 128.6 (s,  $\text{Quinoly}$ ), 128.5 (s,  $\text{Quinoly}$ ), 125.3 (t,  $J_{\text{P-C}} = 3.3$  Hz,  $\text{Phenyl}$ ), 124.9 (s,  $\text{Quinoly}$ ), 121.3 (s,  $\text{Quinoly}$ ), 29.8 (t,  $J_{\text{P-C}} = 8.4$  Hz,  $\text{CHMe}_2$ ), 28.6 (t,  $J_{\text{P-C}} = 14.6$  Hz,  $\text{CHMe}_2$ ), 21.6 (t,  $J_{\text{P-C}} = 4.6$  Hz,  $\text{CHMe}_2$ ), 20.3 (t,  $J_{\text{P-C}} = 4.2$  Hz,  $\text{CHMe}_2$ ), 20.1 (s,  $\text{CHMe}_2$ ), 19.8 (s,  $\text{CHMe}_2$ ). Anal. Calc. for  $\text{C}_{33}\text{H}_{43}\text{BNP}_2\text{Rh}$ : C, 62.98; H, 6.89; N, 2.23. Found: C, 62.35; H, 6.59; N, 2.25.



**Synthesis of (PBP)Ir(Qu)H/(PB<sup>Qu</sup>P)IrH (1IrCq/1IrNq).** **6** (0.30 g, 0.48 mmol) and quinoline (63  $\mu$ L, 0.53 mmol) was dissolved in 2 mL toluene, to which was added sodium bis(trimethylsilyl)amide (88 mg, 0.48 mmol). The reaction mixture was stirred at r. t. for 1 h, and passed through Celite. Volatiles were removed under vacuum, and the resulting solid was recrystallized in toluene/pentane 1:10, yielding an orange solid (0.25 g, 72%). The resulting product exists as an equilibrium in solution, and the ratio was calculated to be **1IrCq/1IrNq** = 1/0.06 by integration of the most downfield PBP-*Phenyl* signal in  $^1\text{H}$  NMR spectrum. NMR spectroscopic data for **1IrCq**:  $^1\text{H}$  NMR (500 MHz,  $\text{C}_6\text{D}_6$ )  $\delta$  8.80 (d,  $J_{\text{H-H}} = 7.6$  Hz, 2H, PBP-*Phenyl*), 8.19 (d,  $J_{\text{H-H}} = 8.4$  Hz, 1H, *Quinolyl*), 8.00 (d,  $J_{\text{H-H}} = 8.5$  Hz, 1H, *Quinolyl*), 7.24 (t,  $J_{\text{H-H}} = 7.3$  Hz, 2H, PBP-*Phenyl*), 7.20 (m, 2H, PBP-*Phenyl*), 7.10 (m, 5H, PBP-*Phenyl* & *Quinolyl*), 6.78 (t,  $J_{\text{H-H}} = 7.4$  Hz, 1H, *Quinolyl*), 2.47 (m, 2H,  $\text{CHMe}_2$ ), 2.17 (m, 2H,  $\text{CHMe}_2$ ), 1.36 (dvt,  $J_{\text{H-H}} = J_{\text{H-P}} = 7.5$  Hz, 6H,  $\text{CHMe}_2$ ), 1.14 (dvt,  $J_{\text{H-H}} = J_{\text{H-P}} = 7.2$  Hz, 6H,  $\text{CHMe}_2$ ), 1.03 (dvt,  $J_{\text{H-H}} = J_{\text{H-P}} = 7.1$  Hz, 6H,  $\text{CHMe}_2$ ), 0.61 (dvt,  $J_{\text{H-H}} = J_{\text{H-P}} = 7.0$  Hz, 6H,  $\text{CHMe}_2$ ), -0.20 (t,  $J_{\text{H-P}} = 23.2$  Hz, 1H, Ir-H).  $^{31}\text{P}$  NMR (202 MHz,  $\text{C}_6\text{D}_6$ , with selected range of  $^1\text{H}$  decoupled)  $\delta$  59.0 (s).  $^{11}\text{B}\{^1\text{H}\}$  NMR (128 MHz,  $\text{C}_6\text{D}_6$ )  $\delta$  -8.5.  $^{13}\text{C}\{^1\text{H}\}$  NMR (126 MHz,  $\text{C}_6\text{D}_6$ )  $\delta$  201.3 (t,  $J_{\text{P-C}} = 6.2$  Hz, Ir-C), 159.0 (br, B-*Phenyl*), 141.6 (s, *Quinolyl*), 141.0 (t,  $J_{\text{P-C}} = 23.9$  Hz, P-*Phenyl*), 135.6 (s, *Quinolyl*), 130.2 (s, *Phenyl*), 130.1 (s, *Quinolyl*), 129.8 (t,  $J_{\text{P-C}} = 8.2$  Hz, *Phenyl*), 129.5 (s, *Quinolyl*), 129.0 (s,



*Quinolyl*), 126.0 (t,  $J_{\text{P-C}} = 3.6$  Hz, *Phenyl*), 127.7 (s, *Phenyl*), 124.1 (s, *Quinolyl*), 122.9 (s, *Quinolyl*), 117.7 (s, *Quinolyl*), 30.5 (t,  $J_{\text{P-C}} = 11.7$  Hz,  $\text{CHMe}_2$ ), 29.0 (t,  $J_{\text{P-C}} = 18.1$  Hz,  $\text{CHMe}_2$ ), 20.6 (s,  $\text{CHMe}_2$ ), 20.5 (t,  $J_{\text{P-C}} = 3.5$  Hz,  $\text{CHMe}_2$ ), 20.3 (m,  $\text{CHMe}_2$ ), 19.60 (s,  $\text{CHMe}_2$ ). Selected NMR spectroscopic data for **1IrNq**.  $^1\text{H}$  NMR (500 MHz,  $\text{C}_6\text{D}_6$ )  $\delta$  8.64 (d,  $J_{\text{H-H}} = 7.6$  Hz, 2H, PBP-*Phenyl*), 8.14 (d,  $J_{\text{H-H}} = 7.8$  Hz, 1H, *Quinolyl*), 6.84 (d,  $J_{\text{H-H}} = 8.4$  Hz, 2H, PBP-*Phenyl*), 2.00 (m, 2H,  $\text{CHMe}_2$ ), 0.19 (dvt,  $J_{\text{H-H}} = J_{\text{H-P}} = 7.1$  Hz, 6H,  $\text{CHMe}_2$ ), -17.10 (t,  $J_{\text{P-H}} = 19.5$  Hz, Ir-H).  $^{31}\text{P}$  NMR (202 MHz,  $\text{C}_6\text{D}_6$ , with selected range of  $^1\text{H}$  decoupled)  $\delta$  59.0 (d,  $J_{\text{P-H}} = 19.3$  Hz, Ir-H). Anal. Calc. for  $\text{C}_{33}\text{H}_{43}\text{BIrNP}_2$ : C, 55.15; H, 6.03; N, 1.95. Found: C, 55.21; H, 6.23; N, 2.01.

**VT-NMR experiment of 1IrCq/1IrNq in  $\text{C}_6\text{D}_6$ .** In a J. Young tube, **1IrCq/1IrNq** was dissolved in 0.4 mL  $\text{C}_6\text{D}_6$ .  $^1\text{H}$  NMR were recorded at different temperature using a 500 MHz Varian NMR. **1IrCq/1IrNq** exists as an equilibrium in solution, and the ratio was calculated by integration of the most downfield PBP-*Phenyl* signal in  $^1\text{H}$  NMR spectrum. (**Figure S2**)

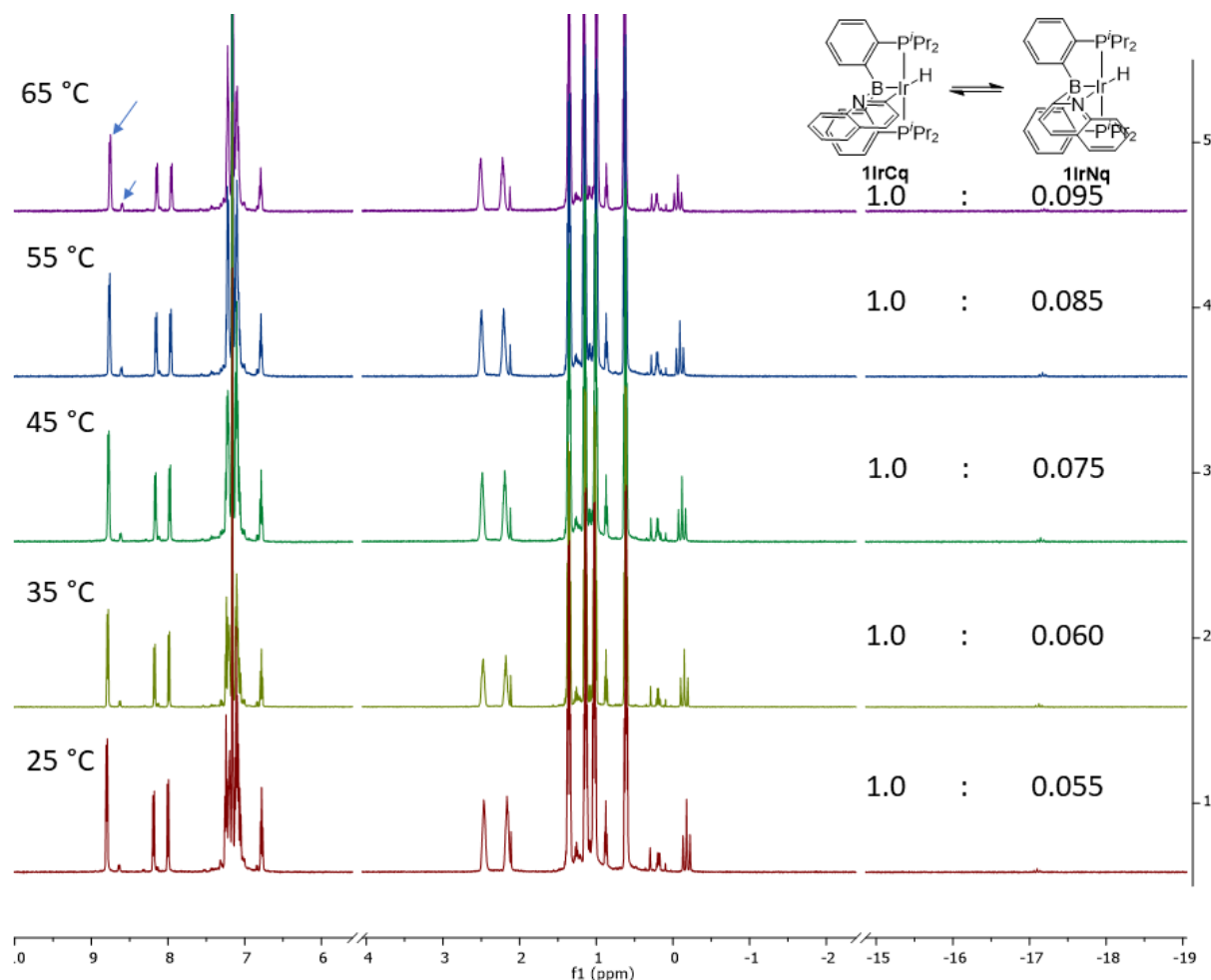
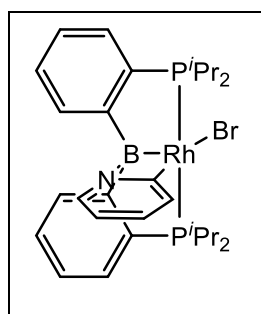


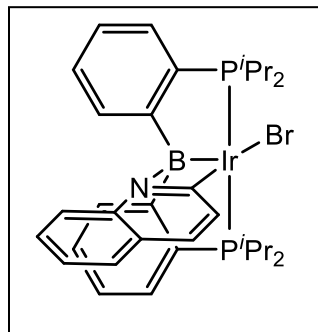
**Figure S2.** VT-NMR experiment of **1IrCq/1IrNq** on a 500 MHz Varian NMR.



**(PBP)RhPyBr (2RhC).** In a J. Young tube, N-bromosuccinimide (0.17 mmol, 30 mg) was added to a solution of **1RhN** (100 mg, 0.17 mmol) in 0.40 mL C<sub>6</sub>D<sub>6</sub>. This reaction mixture was stirred at room temperature for 24 h and heated at 100 °C for 12 h until all **1RhN** were consumed. (monitored by <sup>31</sup>P{<sup>1</sup>H} NMR). The resulting mixture was filtered over a pad of silica

gel and washed through with dichloromethane. All volatiles were removed under vacuum and the resulting solid was recrystallized from toluene/pentane (1:3), yield an orange solid (80 mg, 70%)

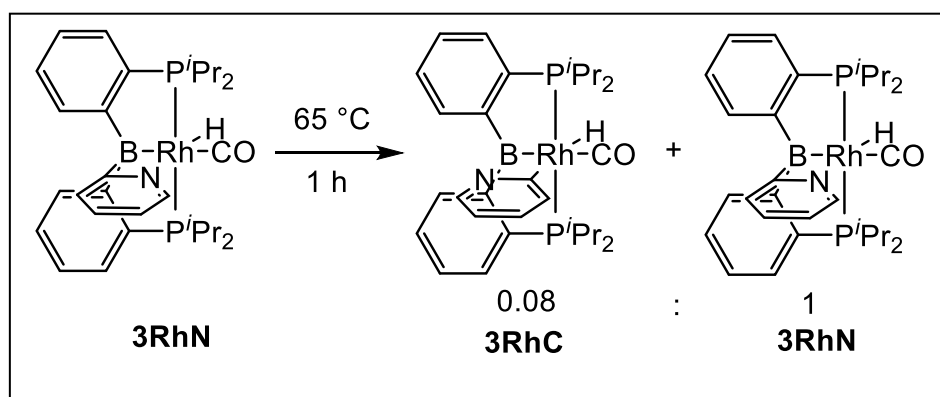
$^1\text{H}$  NMR (500 MHz,  $\text{C}_6\text{D}_6$ )  $\delta$  8.44 (d,  $J_{\text{H-H}} = 7.5$  Hz, 2H, PBP-*Phenyl*), 7.61 (d,  $J_{\text{H-H}} = 8.2$  Hz, 1H, *Pyridyl*), 7.32 (t,  $J_{\text{H-H}} = 6.8$  Hz, 2H, PBP-*Phenyl*), 7.13 (m, 4H, PBP-*Phenyl*), 6.62 (d,  $J_{\text{H-H}} = 5.6$  Hz, 1H, *Pyridyl*), 6.09 (t,  $J_{\text{H-H}} = 7.7$  Hz, 1H, *Pyridyl*), 5.59 (t,  $J_{\text{H-H}} = 6.5$  Hz, 1H, *Pyridyl*), 3.56 (m, 2H,  $\text{CHMe}_2$ ), 2.14 (m, 2H,  $\text{CHMe}_2$ ), 1.56 (dvt,  $J_{\text{H-H}} = J_{\text{H-P}} = 7.3$  Hz, 6H,  $\text{CHMe}_2$ ), 1.15 (dvt,  $J_{\text{H-H}} = J_{\text{H-P}} = 7.5$  Hz, 6H,  $\text{CHMe}_2$ ), 1.08 (dvt,  $J_{\text{H-H}} = J_{\text{H-P}} = 6.5$  Hz, 6H,  $\text{CHMe}_2$ ), 0.49 (dvt,  $J_{\text{H-H}} = J_{\text{H-P}} = 7.5$  Hz, 6H,  $\text{CHMe}_2$ ).  $^{31}\text{P}\{^1\text{H}\}$  NMR (202 MHz,  $\text{C}_6\text{D}_6$ ):  $\delta$  42.8 (d,  $J_{\text{P-Rh}} = 129.2$  Hz).  $^{11}\text{B}\{^1\text{H}\}$  NMR (128 MHz,  $\text{C}_6\text{D}_6$ ):  $\delta$  1.7.  $^{13}\text{C}\{^1\text{H}\}$  NMR (126 MHz,  $\text{C}_6\text{D}_6$ )  $\delta$  178.0 (dt,  $J_{\text{C-Rh}} = 34.8$  Hz,  $J_{\text{C-P}} = 10.2$  Hz, C-Rh), 160.1 (br, B-*Phenyl*), 138.5 (s, *Pyridyl*), 137.3 (td,  $J_{\text{P-C}} = 19.0$  Hz,  $J_{\text{Rh-C}} = 3.4$  Hz, P-*Phenyl*), 134.0 (s, *Pyridyl*), 131.8 (s, *Pyridyl*), 131.7 (s, *Phenyl*), 131.2 (t,  $J_{\text{P-C}} = 9.1$  Hz, *Phenyl*), 129.5 (s, *Phenyl*), 127.4 (t,  $J_{\text{P-C}} = 3.2$  Hz, *Phenyl*), 116.0 (s, *Pyridyl*), 27.6 (t,  $J_{\text{P-C}} = 12.3$  Hz,  $\text{CHMe}_2$ ), 25.6 (t,  $J_{\text{P-C}} = 10.3$  Hz,  $\text{CHMe}_2$ ), 20.6 (s,  $\text{CHMe}_2$ ), 19.9 (t,  $J_{\text{P-C}} = 2.3$  Hz,  $\text{CHMe}_2$ ), 19.3 (t,  $J_{\text{P-C}} = 3.1$  Hz,  $\text{CHMe}_2$ ), 18.4 (s,  $\text{CHMe}_2$ ). Anal. Calc. for  $\text{C}_{29}\text{H}_{40}\text{BBrNP}_2\text{Rh}$ : C, 52.92; H, 6.13; N, 2.13. Found: C, 52.40; H, 5.81; N, 1.85.



**(PBP)Ir(Qu)Br. (2IrCq).** To **1IrCq/1IrNq** (0.14 mmol, 100 mg) in 2 mL toluene was added N-bromosuccinimide (0.14 mmol, 25 mg). The reaction mixture was heated at 50 °C for 12 h. The resulting mixture was filtered over a pad of silica gel and washed through with dichloromethane. All volatiles were removed under vacuum and the

resulting solid was recrystallized from THF/pentane (1:5), yield an orange solid (77 mg, 69%).  $^1\text{H}$  NMR (500 MHz,  $\text{C}_6\text{D}_6$ )  $\delta$  8.86 (d,  $J_{\text{H-H}} = 7.7$  Hz, 2H, PBP-*Phenyl*), 7.67 (d,  $J_{\text{H-H}} = 8.8$  Hz, 1H, *Quinolyl*), 7.64 (d,  $J_{\text{H-H}} = 8.3$  Hz, 1H, *Quinolyl*), 7.30 (m, 2H, PBP-*Phenyl*), 7.07 (m, 4H, PBP-*Phenyl*), 6.89 (m, 2H, *Quinolyl*), 6.65 (t,  $J_{\text{H-H}} = 7.5$  Hz, 1H, *Quinolyl*), 6.52 (d,  $J_{\text{H-H}} = 8.8$  Hz, 1H, *Quinolyl*), 3.79 (m, 2H,  $\text{CHMe}_2$ ), 2.50 (m, 2H,  $\text{CHMe}_2$ ), 1.51 (dvt,  $J_{\text{H-H}} = J_{\text{H-P}} = 7.3$  Hz, 6H,

CHMe<sub>2</sub>), 1.10 (m, 12H, CHMe<sub>2</sub>), 0.44 (dvt,  $J_{H-H} = J_{H-P} = 7.5$  Hz, 6H, CHMe<sub>2</sub>).  $^{31}\text{P}\{^1\text{H}\}$  NMR (202 MHz, CDCl<sub>3</sub>)  $\delta$  40.0 (s).  $^{11}\text{B}\{^1\text{H}\}$  NMR (128 MHz, CDCl<sub>3</sub>)  $\delta$  -6.8.  $^{13}\text{C}\{^1\text{H}\}$  NMR (126 MHz, CDCl<sub>3</sub>)  $\delta$  176.9 (s, Ir-C), 157.7 (br, B-Phenyl), 152.0 (t,  $J_{C-P} = 6.2$  Hz, Quinolyl), 141.0 (s, Quinolyl), 136.1 (t,  $J_{C-P} = 24.4$  Hz, P-Phenyl), 131.1 (t,  $J_{C-P} = 1.8$  Hz, Phenyl), 131.1 (s, Quinolyl), 130.3 (t,  $J_{C-P} = 8.3$  Hz, Phenyl), 129.8 (s, Quinolyl), 128.7 (s, Quinolyl), 128.4 (s, Phenyl), 126.3 (t,  $J_{C-P} = 3.8$  Hz, Phenyl), 123.7 (s, Quinolyl), 123.6 (s, Quinolyl), 117.0 (s, Quinolyl), 25.6 (t,  $J_{C-P} = 15.9$  Hz, CHMe<sub>2</sub>), 25.0 (t,  $J_{C-P} = 12.6$  Hz, CHMe<sub>2</sub>), 19.4 (s, CHMe<sub>2</sub>), 18.9 (t,  $J_{C-P} = 1.6$  Hz, CHMe<sub>2</sub>), 18.6 (t,  $J_{C-P} = 2.8$  Hz, CHMe<sub>2</sub>), 17.9 (s, CHMe<sub>2</sub>). Anal. Calc. for C<sub>29</sub>H<sub>40</sub>BBrNP<sub>2</sub>Ir: C, 49.70; H, 5.31; N, 1.36. Found: C, 48.95; H, 5.06; N, 1.68.



**In situ generation of (PB<sup>Py</sup>P)RhH(CO) and observation of the mixture of (PB<sup>Py</sup>P)RhH(CO)/(PBP)RhPyH(CO) after heating (3RhN/3RhC).** In a J. Young tube, 1 atm of CO was added to a solution of **1RhN** (40 mg, 0.086 mmol) in 0.40 mL C<sub>6</sub>D<sub>6</sub> after 3 rounds of freeze-pump-thaw. After stirring at room temperature for 10 min, NMR spectra were recorded, showing the generation of **3RhN**. All volatiles were removed and 0.40 mL C<sub>6</sub>D<sub>6</sub> was added. ATR-IR spectrum were recorded. The solution was heated at 65 °C for 1 h.  $^1\text{H}$  NMR and  $^{31}\text{P}\{^1\text{H}\}$  NMR spectra were recorded at room temperature after heating, showing a mixture of **3RhC/3RhN** (0.08:1). (calculated by integration of methyl signals in  $^1\text{H}$  NMR spectrum). The mixture was

further heated at 65 °C for 24 h. It resulted in a mixture of four different compounds: an unidentified complex, **3RhC**, **3RhN**, and **1RhN** (1:3:17:1). ( $^{31}\text{P}\{^1\text{H}\}$  NMR evidence, **Figure S3**).

Spectroscopic data for **3RhN** under CO atmosphere:  $^1\text{H}$  NMR (500 MHz,  $\text{C}_6\text{D}_6$ )  $\delta$  8.41 (d,  $J_{\text{H-H}} = 7.6$  Hz, 2H,  $\text{PB}^{\text{Py}}\text{P-Phenyl}$ ), 7.90 (d,  $J_{\text{H-H}} = 5.0$  Hz, 1H,  $\text{PB}^{\text{Py}}\text{P-Pyridyl}$ ), 7.36 (t,  $J_{\text{H-H}} = 7.0$  Hz, 2H,  $\text{PB}^{\text{Py}}\text{P-Phenyl}$ ), 7.15 (m, 4H,  $\text{PB}^{\text{Py}}\text{P-Phenyl}$ ), 6.67 (t,  $J_{\text{H-H}} = 7.6$  Hz, 1H,  $\text{PB}^{\text{Py}}\text{P-Pyridyl}$ ), 6.58 (d,  $J_{\text{H-H}} = 7.7$  Hz, 1H,  $\text{PB}^{\text{Py}}\text{P-Pyridyl}$ ), 6.28 (dd,  $J_{\text{H-H}} = 7.2, 5.2$  Hz, 1H,  $\text{PB}^{\text{Py}}\text{P-Pyridyl}$ ), 2.17 (m, 2H,  $\text{CHMe}_2$ ), 2.03 (m, 2H,  $\text{CHMe}_2$ ), 1.26 (dvt,  $J_{\text{H-H}} = J_{\text{H-P}} = 7.0$  Hz, 6H,  $\text{CHMe}_2$ ), 1.18 (dvt,  $J_{\text{H-H}} = J_{\text{H-P}} = 7.2$  Hz, 6H,  $\text{CHMe}_2$ ), 0.86 (dvt,  $J_{\text{H-H}} = J_{\text{H-P}} = 7.1$  Hz, 6H,  $\text{CHMe}_2$ ), 0.58 (dvt,  $J_{\text{H-H}} = J_{\text{H-P}} = 7.2$  Hz, 6H,  $\text{CHMe}_2$ ), -15.69 (br, 1H, Rh-H).  $^{31}\text{P}\{^1\text{H}\}$  NMR (202 MHz,  $\text{C}_6\text{D}_6$ )  $\delta$  71.6 (d,  $J_{\text{P-Rh}} = 130.2$  Hz).  $^{11}\text{B}\{^1\text{H}\}$  NMR (160 MHz,  $\text{C}_6\text{D}_6$ )  $\delta$  2.0.  $^{13}\text{C}\{^1\text{H}\}$  NMR (126 MHz,  $\text{C}_6\text{D}_6$ )  $\delta$  221.6 (s, free CO), 193.5 (br, Rh-B-C-N), 165.8 (br, B-Phenyl), 150.1 (s, Pyridyl), 141.0 (t,  $J_{\text{P-C}} = 21.7$  Hz, P-Phenyl), 132.9 (s, Pyridyl), 132.2 (t,  $J_{\text{P-C}} = 9.1$  Hz, Phenyl), 129.3 (s, Phenyl), 129.2 (s, Phenyl), 125.1 (t,  $J_{\text{P-C}} = 3.2$  Hz, Phenyl), 125.0 (s, Pyridyl), 120.4 (s, Pyridyl), 30.1 (t,  $J_{\text{P-C}} = 10.1$  Hz,  $\text{CHMe}_2$ ), 29.2 (t,  $J_{\text{P-C}} = 15.1$  Hz,  $\text{CHMe}_2$ ), 20.2 (s,  $\text{CHMe}_2$ ), 19.9 (t,  $J_{\text{P-C}} = 2.6$  Hz,  $\text{CHMe}_2$ ), 19.8 (t,  $J_{\text{P-C}} = 2.9$  Hz,  $\text{CHMe}_2$ ), 19.6 (s,  $\text{CHMe}_2$ ). (Rh-CO signals were not observed due to broadness). ATR-IR:  $\nu_{\text{CO}}$  1968  $\text{cm}^{-1}$  Selected spectroscopic data for **3RhC**:  $^1\text{H}$  NMR (500 MHz,  $\text{C}_6\text{D}_6$ )  $\delta$  7.67 (d,  $J_{\text{H-H}} = 7.7$  Hz, 1H, Pyridyl), 7.32 (t,  $J_{\text{H-H}} = 5.6$  Hz, 2H,  $\text{PBP-Phenyl}$ ), 6.51 (t,  $J_{\text{H-H}} = 7.5$  Hz, 1H, Pyridyl), 5.92 (t,  $J_{\text{H-H}} = 6.5$  Hz, 1H, Pyridyl), 1.98 (m, 2H,  $\text{CHMe}_2$ ), 0.93 (dvt,  $J_{\text{H-H}} = J_{\text{H-P}} = 7.1$  Hz, 6H,  $\text{CHMe}_2$ ), 0.40 (dvt,  $J_{\text{H-H}} = J_{\text{H-P}} = 7.1$  Hz, 6H,  $\text{CHMe}_2$ ), -11.04 (dt,  $J_{\text{H-P}} = 12.6$  Hz,  $J_{\text{H-Rh}} = 10.4$  Hz, 1H, Rh-H).  $^{31}\text{P}\{^1\text{H}\}$  NMR (202 MHz,  $\text{C}_6\text{D}_6$ )  $\delta$  78.8 (d,  $J_{\text{P-Rh}} = 126.1$  Hz). Other signals overlapped with **3RhN**.

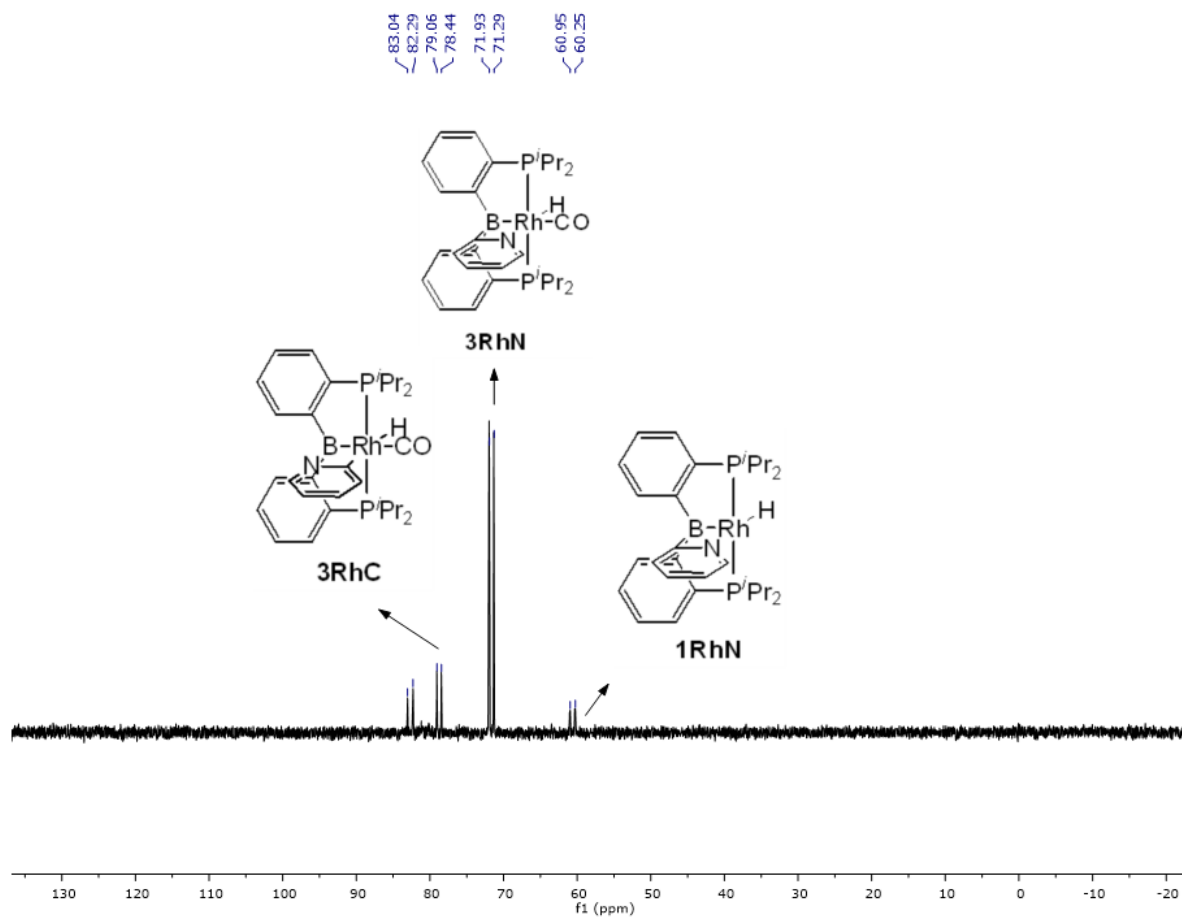
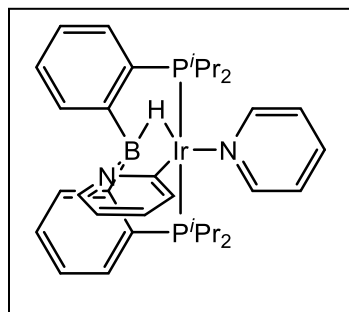


**Figure S3.**  $^{31}\text{P}\{^1\text{H}\}$  NMR (202 MHz,  $\text{C}_6\text{D}_6$ ) spectrum recorded at room temperature after the reaction mixture were heated at 65 °C for 24 h. The sample contains a mixture of an unidentified complex, **3RhC**, **3RhN**, and **1RhN** at a ratio of 1:3:17:1.



**(PBP)Ir(Py)H(Py) (7).** To **6** (0.10 mmol, 63 mg) in 2 mL toluene was added pyridine (9.0  $\mu$ L, 0.10 mmol) and sodium bis(trimethylsilyl)amide (19 mg, 0.10 mmol). After being heated at 45  $^{\circ}$ C for 12 h,  $^{31}\text{P}\{^1\text{H}\}$  NMR spectrum were recorded, showing a mixture of three unidentified complexes. Additional pyridine (18  $\mu$ L,

0.10 mmol) were added, and the mixture was heated at 45  $^{\circ}$ C for 12 h. The reaction mixture was filtered through Celite, and volatiles were removed under vacuum.  $\text{C}_6\text{D}_6$  were added and NMR spectra were recorded for characterization.  $^1\text{H}$  NMR (500 MHz,  $\text{C}_6\text{D}_6$ )  $\delta$  8.97 (dt,  $J_{\text{H-H}} = 1.6$  Hz, 4.4 Hz, 2H, PBP-Phenyl), 8.53 (d,  $J_{\text{H-H}} = 7.5$  Hz, 2H, Ir-Pyridine), 7.85 (d,  $J_{\text{H-H}} = 7.8$  Hz, 1H, Pyridyl), 7.30 (m, 5H, PBP-Phenyl & Pyridyl), 7.18 (m, 2H, PBP-Phenyl), 6.94 (tt,  $J_{\text{H-H}} = 1.8$  Hz, 7.6 Hz, 1H, Ir-Pyridine), 6.72 (td,  $J_{\text{H-H}} = 1.6$  Hz, 7.6 Hz, 1H, Pyridyl), 6.58 (ddd,  $J_{\text{H-H}} = 1.5$  Hz, 4.5 Hz, 7.6 Hz, 2H, Ir-Pyridine), 5.93 (t,  $J_{\text{H-H}} = 6.3$  Hz, 1H, Pyridyl), 2.48 (m, 2H,  $\text{CHMe}_2$ ), 2.33 (m, 2H,  $\text{CHMe}_2$ ), 1.24 (dvt,  $J_{\text{H-H}} = J_{\text{H-P}} = 7.6$  Hz, 6H,  $\text{CHMe}_2$ ), 1.09 (dvt,  $J_{\text{H-H}} = J_{\text{H-P}} = 6.9$  Hz, 6H,  $\text{CHMe}_2$ ), 0.98 (dvt,  $J_{\text{H-H}} = J_{\text{H-P}} = 7.0$  Hz, 6H,  $\text{CHMe}_2$ ), 0.62 (dvt,  $J_{\text{H-H}} = J_{\text{H-P}} = 7.1$  Hz, 6H,  $\text{CHMe}_2$ ), -7.17 (br, 1H, Ir-H).  $^{31}\text{P}\{^1\text{H}\}$  NMR (202 MHz,  $\text{C}_6\text{D}_6$ )  $\delta$  50.0 (s).  $^{11}\text{B}\{^1\text{H}\}$  NMR (128 MHz,  $\text{C}_6\text{D}_6$ )  $\delta$  -7.4.  $^{13}\text{C}\{^1\text{H}\}$  NMR (126 MHz,  $\text{C}_6\text{D}_6$ )  $\delta$  153.4 (s), 142.5 (t,  $J_{\text{P-C}} = 3.2$  Hz), 139.3 (s), 136.4 (s), 134.8 (s), 131.7 (s), 129.6 (s), 129.2 (t,  $J_{\text{P-C}} = 8.8$  Hz), 125.7 (t,  $J_{\text{P-C}} = 3.4$  Hz), 123.7 (s), 117.9 (s), 113.4 (s), 30.6 (t,  $J_{\text{P-C}} = 11.2$  Hz), 30.2 (t,  $J_{\text{P-C}} = 17.2$  Hz), 20.2 (m, 2C), 19.9 (t,  $J_{\text{P-C}} = 2.8$  Hz), 19.6 (s).



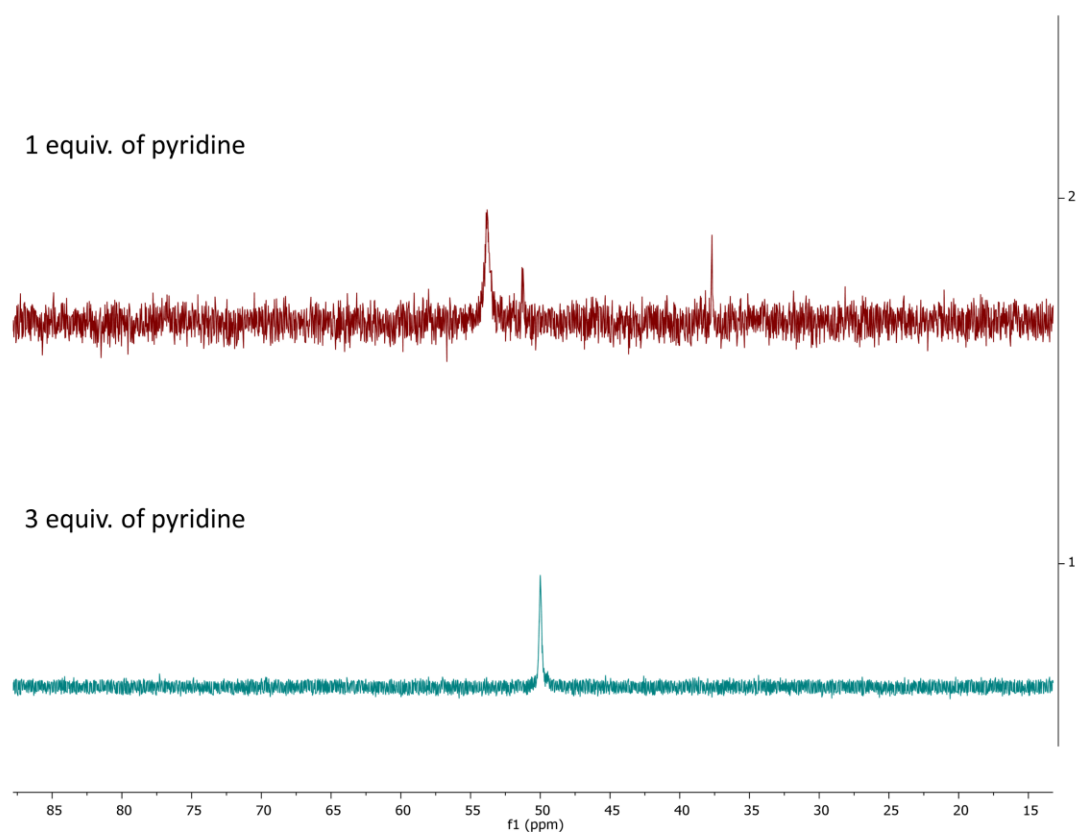


**Figure S4.** Top:  $^{31}\text{P}\{^1\text{H}\}$  NMR recorded at room temperature on a 500 MHz Varian NMR for a mixture of **6** (0.10 mmol), pyridine (0.10 mmol) and sodium bis(trimethylsilyl)amide (0.10 mmol) in 2 mL toluene after being heated at 45 °C for 12 h. Bottom:  $^{31}\text{P}\{^1\text{H}\}$  NMR recorded at room temperature on a 500 MHz Varian NMR for the same mixture after adding additional pyridine (0.20 mmol) and being heated at 45 °C for another 12 h.

### 3. X-ray Structural Determination Details.

**1RhN.** A light yellow, multi-faceted block of suitable size ( $0.46 \times 0.22 \times 0.16 \text{ mm}^3$ ) was selected from a representative sample of crystals of the same habit using an optical microscope and mounted onto a nylon loop. Low temperature (110 K) X-ray data were obtained on a Bruker APEXII CCD based diffractometer (Mo sealed X-ray tube,  $K_{\alpha} = 0.71073 \text{ \AA}$ ). All diffractometer manipulations, including data collection, integration and scaling were carried out using the Bruker APEXII software.<sup>2</sup> An absorption correction was applied using SADABS.<sup>3</sup> The space group was determined on the basis of systematic absences and intensity statistics and the structure was solved by direct methods and refined by full-matrix least squares on  $F^2$ . The structure was solved in the monoclinic  $P 2_1/c$  space group using XS<sup>4</sup> (incorporated in Olex). All non-hydrogen atoms were refined with anisotropic thermal parameters. All hydrogen atoms were placed in idealized positions and refined using riding model with the exception of the hydrogen bound to rhodium which was located from the difference map. The structure was refined (weighted least squares refinement on  $F^2$ ) and the final least-squares refinement converged. No additional symmetry was found using ADDSYM incorporated in PLATON program.<sup>5</sup> CCDC 2014200 contain the supplementary crystallographic data.

**1RhNq.** A Leica MZ 7<sub>5</sub> microscope was used to identify a suitable yellow block with very well-defined faces with dimensions (max, intermediate, and min)  $0.368 \times 0.36 \times 0.164 \text{ mm}^3$  from a representative sample of crystals of the same habit. The crystal mounted on a nylon loop was then placed in a cold nitrogen stream (Oxford) maintained at 110 K. A BRUKER APEX 2 X-ray (three-circle) diffractometer was employed for crystal screening, unit cell determination, and data collection. The goniometer was controlled using the APEX2 software suite, v2008-6.0.<sup>6</sup> The sample was optically centered with the aid of a video camera such that no translations were

observed as the crystal was rotated through all positions. The detector was set at 6.0 cm from the crystal sample (APEX2, 512x512 pixel). The X-ray radiation employed was generated from a Mo sealed X-ray tube ( $K_{\alpha} = 0.70173\text{\AA}$  with a potential of 40 kV and a current of 40 mA). Sixty data frames were taken at widths of  $1.0^{\circ}$ . These reflections were used in the auto-indexing procedure to determine the unit cell. A suitable cell was found and refined by nonlinear least squares and Bravais lattice procedures. The unit cell was verified by examination of the  $hkl$  overlays on several frames of data. No super-cell or erroneous reflections were observed. After careful examination of the unit cell, an extended data collection procedure (4 sets) was initiated using omega scans. Integrated intensity information for each reflection was obtained by reduction of the data frames with the program APEX2.<sup>6</sup> The integration method employed a three-dimensional profiling algorithm and all data were corrected for Lorentz and polarization factors, as well as for crystal decay effects. Finally, the data was merged and scaled to produce a suitable data set. The absorption correction program SADABS<sup>3</sup> was employed to correct the data for absorption effects. Systematic reflection conditions and statistical tests of the data suggested the space group  $P-1$ . A solution was obtained readily using XT/XS in APEX2.<sup>4,6</sup> Hydrogen atoms were placed in idealized positions and were set riding on the respective parent atoms. All non-hydrogen atoms were refined with anisotropic thermal parameters. Absence of additional symmetry and voids were confirmed using PLATON (ADDSYM).<sup>5</sup> The structure was refined (weighted least squares refinement on  $F^2$ ) to convergence.<sup>4,7</sup> CCDC 2014201 contain the supplementary crystallographic data.

**1IrCq.** A Leica MZ 75 microscope was used to identify an orange plate with very well-defined faces with dimensions (max, intermediate, and min)  $0.528 \times 0.213 \times 0.046 \text{ mm}^3$  from a representative sample of crystals of the same habit. The crystal mounted on a nylon loop was then placed in a cold nitrogen stream (Oxford) maintained at 110 K. A BRUKER APEX 2 Duo X-ray

(three-circle) diffractometer was employed for crystal screening, unit cell determination, and data collection. The goniometer was controlled using the APEX3 software suite, v2017.3-0.<sup>8</sup> The sample was optically centered with the aid of a video camera such that no translations were observed as the crystal was rotated through all positions. The detector (Bruker - PHOTON) was set at 6.0 cm from the crystal sample. The X-ray radiation employed was generated from a Mo sealed X-ray tube ( $K_{\alpha} = 0.71073 \text{ \AA}$  with a potential of 40 kV and a current of 40 mA). 45 data frames were taken at widths of  $1.0^{\circ}$ . These reflections were used in the auto-indexing procedure to determine the unit cell. A suitable cell was found and refined by nonlinear least squares and Bravais lattice procedures. The unit cell was verified by examination of the  $hkl$  overlays on several frames of data. No super-cell or erroneous reflections were observed. After careful examination of the unit cell, an extended data collection procedure (16 sets) was initiated using omega scans. Integrated intensity information for each reflection was obtained by reduction of the data frames with the program APEX3.<sup>8</sup> The integration method employed a three-dimensional profiling algorithm and all data were corrected for Lorentz and polarization factors, as well as for crystal decay effects. Finally, the data was merged and scaled to produce a suitable data set. The absorption correction program SADABS<sup>3</sup> was employed to correct the data for absorption effects. Systematic reflection conditions and statistical tests of the data suggested the space group  $P-1$ . A solution was obtained readily ( $Z=4$ ;  $Z'=2$ ) using XT/XS in APEX2.<sup>4,8</sup> A molecule of toluene was found solvated (1/2 a molecule per Ir-complex). Hydrogen atoms were placed in idealized positions and were set riding on the respective parent atoms. All non-hydrogen atoms were refined with anisotropic thermal parameters. Elongated ellipsoids and nearby residual electron density peaks for C64 – C66 indicated disorder which was modeled between two positions with an occupancy ratio of 0.77:0.23. Appropriate restraints and constraints were added to keep the bond

distances, angles, and thermal ellipsoids meaningful. Absence of additional symmetry and voids were confirmed using PLATON (ADDSYM). The structure was refined (weighted least squares refinement on  $F^2$ ) to convergence.<sup>4,7</sup> CCDC 2014205 contain the supplementary crystallographic data.

**2RhC.** A Leica MZ 7<sub>5</sub> microscope was used to identify a suitable yellow block with very well-defined faces with dimensions (max, intermediate, and min) 0.222 x 0.19 x 0.182 mm<sup>3</sup> from a representative sample of crystals of the same habit. The crystal mounted on a nylon loop was then placed in a cold nitrogen stream (Oxford) maintained at 110 K. A BRUKER APEX 2 X-ray (three-circle) diffractometer was employed for crystal screening, unit cell determination, and data collection. The goniometer was controlled using the APEX2 software suite, v2008-6.0.<sup>6</sup> The sample was optically centered with the aid of a video camera such that no translations were observed as the crystal was rotated through all positions. The detector was set at 6.0 cm from the crystal sample (APEX2, 512x512 pixel). The X-ray radiation employed was generated from a Mo sealed X-ray tube ( $K_{\alpha} = 0.70173\text{\AA}$  with a potential of 40 kV and a current of 40 mA). Sixty data frames were taken at widths of 1.0°. These reflections were used in the auto-indexing procedure to determine the unit cell. A suitable cell was found and refined by nonlinear least squares and Bravais lattice procedures. The unit cell was verified by examination of the  $hkl$  overlays on several frames of data. No super-cell or erroneous reflections were observed. After careful examination of the unit cell, an extended data collection procedure (4 sets) was initiated using omega scans. Integrated intensity information for each reflection was obtained by reduction of the data frames with the program APEX2.<sup>6</sup> The integration method employed a three-dimensional profiling algorithm and all data were corrected for Lorentz and polarization factors, as well as for crystal decay effects. Finally, the data was merged and scaled to produce a suitable data set. The

absorption correction program SADABS<sup>3</sup> was employed to correct the data for absorption effects. Systematic reflection conditions and statistical tests of the data suggested the space group  $P4_3$ . A solution was obtained readily using XT/XS in APEX2.<sup>4,6</sup> Hydrogen atoms were placed in idealized positions and were set riding on the respective parent atoms. All non-hydrogen atoms were refined with anisotropic thermal parameters. Elongated thermal ellipsoids on C27 and C28 suggested disorder, which was modeled successfully between two positions with an occupancy ratio of 0.42 to 0.58. Appropriate restraints were added to keep the bond distances, angles and thermal ellipsoids meaningful. Absence of additional symmetry and voids were confirmed using PLATON (ADDSYM).<sup>5</sup> The structure was refined (weighted least squares refinement on  $F^2$ ) to convergence.<sup>4,7</sup> CCDC 2014203 contain the supplementary crystallographic data.

**3RhN.** A Leica MZ 7<sub>5</sub> microscope was used to identify a suitable colorless block with very well-defined faces with dimensions (max, intermediate, and min) 0.774 x 0.706 x 0.429 mm<sup>3</sup> from a representative sample of crystals of the same habit. The crystal mounted on a nylon loop was then placed in a cold nitrogen stream (Oxford) maintained at 110 K. A BRUKER APEX 2 Duo X-ray (three-circle) diffractometer was employed for crystal screening, unit cell determination, and data collection. The goniometer was controlled using the APEX3 software suite, v2017.3-0.<sup>8</sup> The sample was optically centered with the aid of a video camera such that no translations were observed as the crystal was rotated through all positions. The detector was set at 6.0 cm from the crystal sample (APEX2, 512x512 pixel). The X-ray radiation employed was generated from a Mo sealed X-ray tube ( $K_{\alpha} = 0.70173\text{\AA}$  with a potential of 40 kV and a current of 40 mA). 45 data frames were taken at widths of 1.0°. These reflections were used in the auto-indexing procedure to determine the unit cell. A suitable cell was found and refined by nonlinear least squares and Bravais lattice procedures. The unit cell was verified by examination of the  $hkl$  overlays on several

frames of data. No super-cell or erroneous reflections were observed. After careful examination of the unit cell, an extended data collection procedure (24 sets) was initiated using omega and phi scans. Integrated intensity information for each reflection was obtained by reduction of the data frames with the program APEX3.<sup>8</sup> The integration method employed a three-dimensional profiling algorithm and all data were corrected for Lorentz and polarization factors, as well as for crystal decay effects. Finally, the data was merged and scaled to produce a suitable data set. The absorption correction program SADABS<sup>3</sup> was employed to correct the data for absorption effects. Systematic reflection conditions and statistical tests of the data suggested the space group  $P2_1/n$ . A solution was obtained readily using XT/XS in APEX2.<sup>4,8</sup> Hydrogen atoms were placed in idealized positions (the one connected to Rh was refined independently) and were set riding on the respective parent atoms. All non-hydrogen atoms were refined with anisotropic thermal parameters. Absence of additional symmetry and voids were confirmed using PLATON (ADDSYM).<sup>5</sup> The structure was refined (weighted least squares refinement on  $F^2$ ) to convergence.<sup>4,7</sup> CCDC 2014204 contain the supplementary crystallographic data.

ORTEP-3 for Windows and POV-Ray were employed for the final data presentation and structure plots.<sup>9,10</sup>



#### 4. DFT Calculations.

The Gaussian suite of programs<sup>11</sup> was used for the ab initio electronic structure calculations. All structures were fully optimized by the B97D3<sup>12</sup> functional in the gas phase, and harmonic vibrational frequency calculations were performed to ensure that either a minimum was obtained. The Los Alamos basis set and the associated effective core potential (ECP) was used for Ru and Ir atoms, and an all-electron 6-31G(d) basis set was used for all the other atoms. Unless otherwise stated, the energies reported in this paper are Gibbs free energies under 298.15 K and 1 atm with solvent effect corrections.

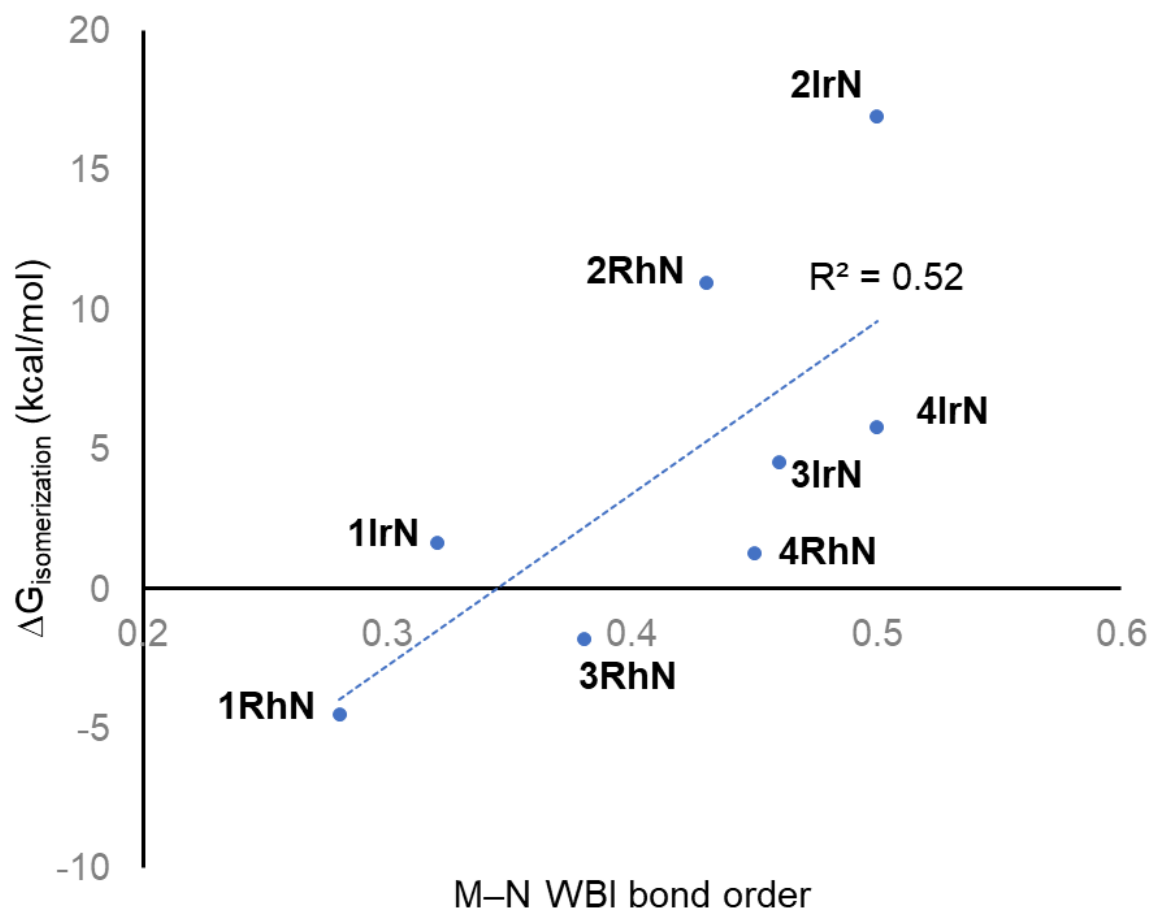
The more recent natural orbitals for chemical valence (NOCV) analyses<sup>13</sup> implemented as part of the ORCA program<sup>14</sup> were applied to study the chemical bonds in terms of the electron density rearrangement taking place upon bond formation at the B97D3/def2-TZVP level using the Extended Transition State (ETS) method of Ziegler. The figures of NOCV deformation densities are generated by Multiwfn code.<sup>15</sup>

**Table S1.** Absolute free energies and enthalpies in the gas phase at 298K and free energies and enthalpies for the M–C/M–N isomerizations (negative values favor the M–N isomer) calculated at the B97D3/LANL2DZ/6-31G(d) level in gas phase.

	Absolute values of Gibbs free energy (G) at 298 K (a. u.)	Absolute values of enthalpy (H) (a. u.)	$\Delta G_{\text{isomerization}}$ (kcal/mol)	$\Delta H_{\text{isomerization}} =$ (kcal/mol)
<b>1RhC</b>	-2000.592744	-2000.486785		
<b>1RhN</b>	-2000.599909	-2000.492665	-4.5	-3.7
<b>1IrC</b>	-1995.792319	-1995.686313		
<b>1IrN</b>	-1995.789668	-1995.681918	1.7	2.8
<b>2RhC</b>	-4572.779866	-4572.670542		
<b>2RhN</b>	-4572.762453	-4572.652586	10.9	11.3
<b>2IrC</b>	-4567.973024	-4567.863829		
<b>2IrN</b>	-4567.946079	-4567.836552	16.9	17.1
<b>3RhC</b>	-2113.872887	-2113.761183		
<b>3RhN</b>	-2113.875726	-2113.763486	-1.8	-1.4
<b>3IrC</b>	-2109.088223	-2108.977483		
<b>3IrN</b>	-2109.081008	-2108.969473	4.5	5.0
<b>4RhC</b>	-2113.847909	-2113.738511		
<b>4RhN</b>	-2113.84592	-2113.73573	1.2	1.7
<b>4IrC</b>	-2109.06682	-2108.958266		
<b>4IrN</b>	-2109.057584	-2108.948267	5.8	6.3

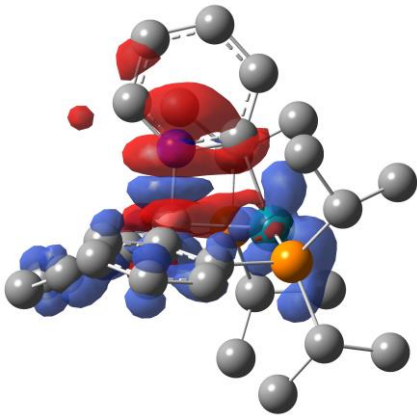
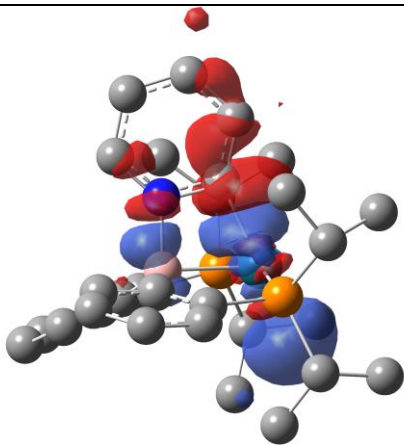
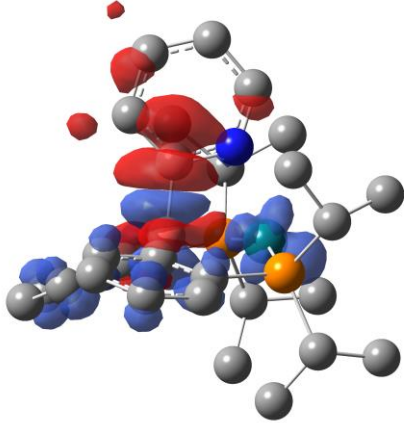
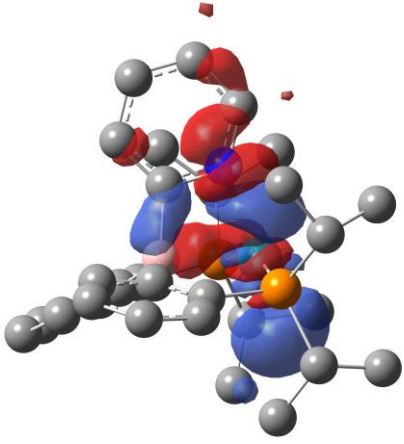
**Table S2.** Wiberg bond indices calculated at the B97D3/LANL2DZ/6-31G(d) level of theory for Type 1-4 Rh and Ir complexes.

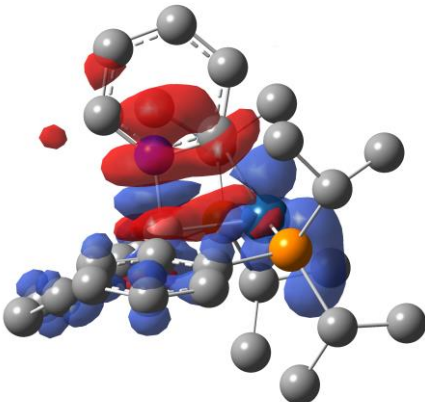
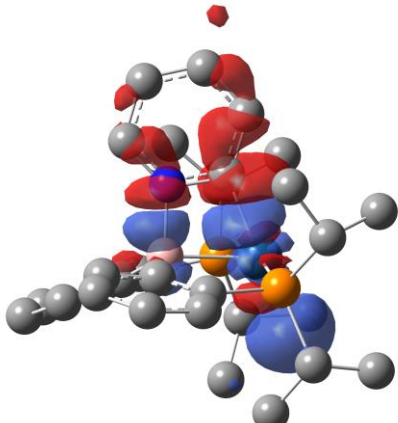
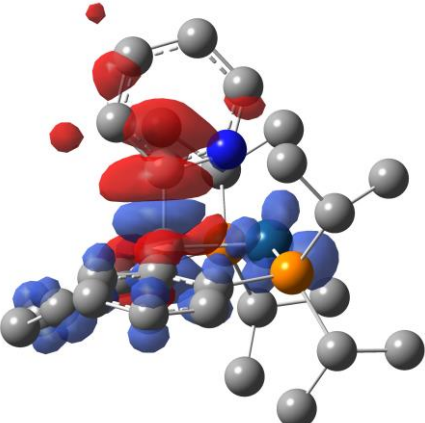
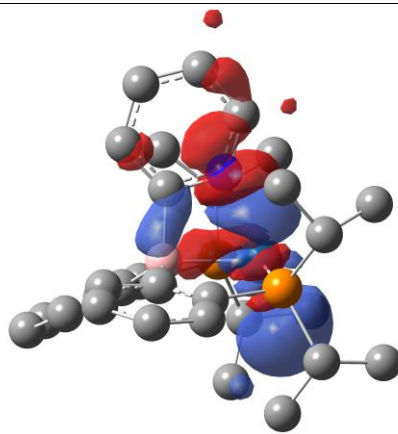
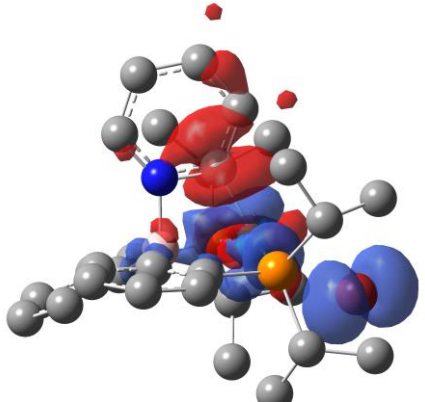
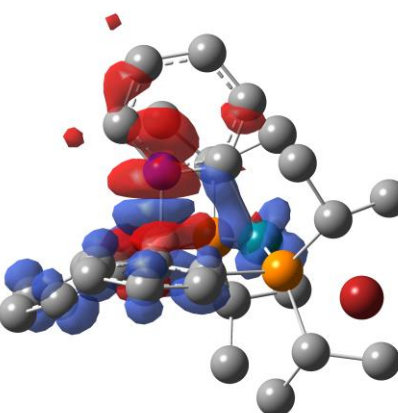
	Wiberg Bond Index			
	M-B	B-C/N	C-N	M-N/C
<b>1RhC</b>	0.58	0.59	1.23	0.59
<b>1RhN</b>	0.56	0.81	1.31	0.28
<b>1IrC</b>	0.66	0.59	1.22	0.67
<b>1IrN</b>	0.65	0.81	1.30	0.32
<b>2RhC</b>	0.52	0.58	1.24	0.75
<b>2RhN</b>	0.52	0.80	1.29	0.43
<b>2IrC</b>	0.60	0.57	1.23	0.83
<b>2IrN</b>	0.61	0.79	1.27	0.50
<b>3RhC</b>	0.51	0.59	1.26	0.65
<b>3RhN</b>	0.48	0.82	1.31	0.38
<b>3IrC</b>	0.59	0.59	1.25	0.73
<b>3IrN</b>	0.56	0.81	1.29	0.46
<b>4RhC</b>	0.49	0.58	1.27	0.68
<b>4RhN</b>	0.41	0.81	1.31	0.45
<b>4IrC</b>	0.58	0.57	1.27	0.72
<b>4IrN</b>	0.54	0.80	1.29	0.50

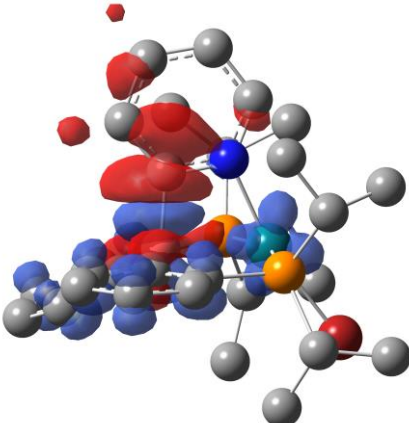
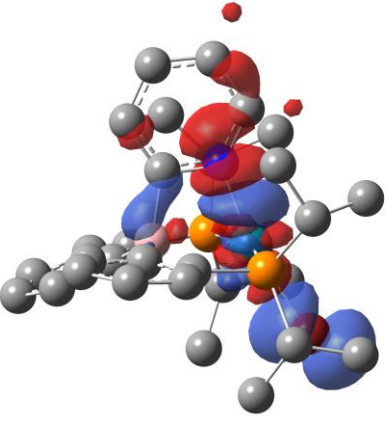
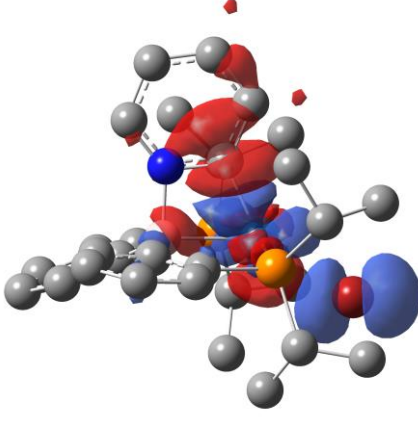
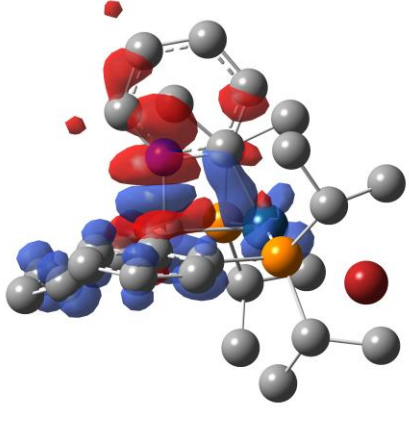
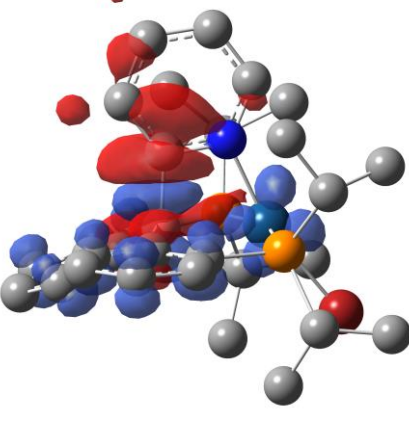
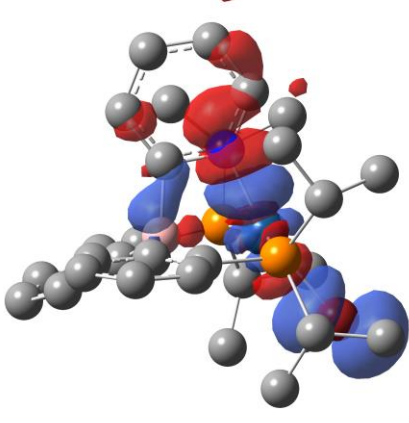


**Figure S5.** Correlation between  $\Delta G_{\text{isomerization}}$  and M-N WBI bond order.

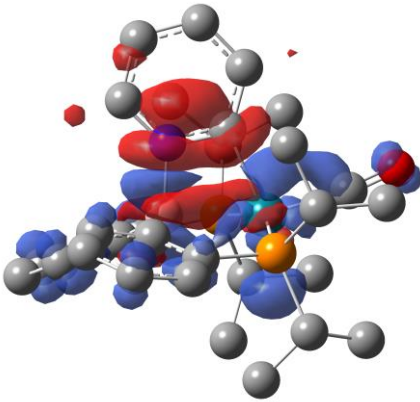
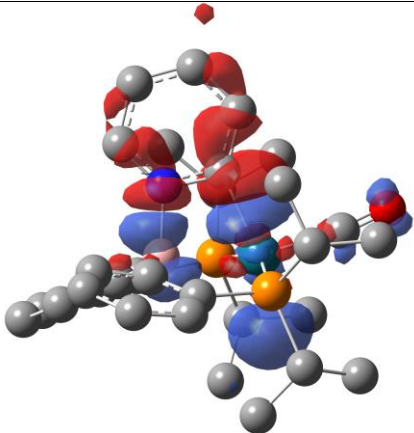
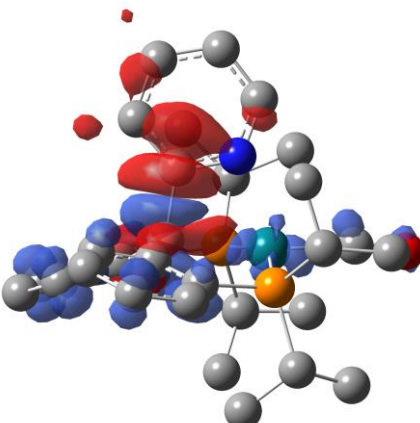
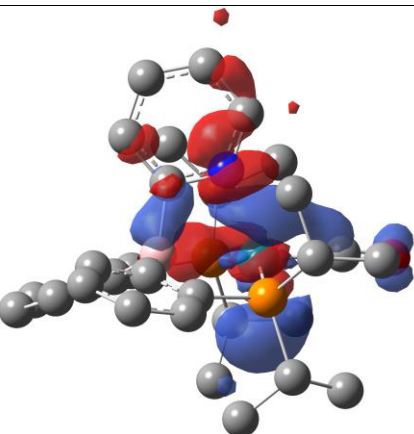
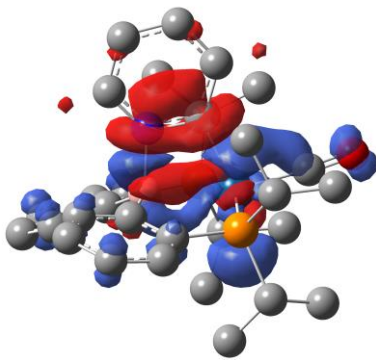
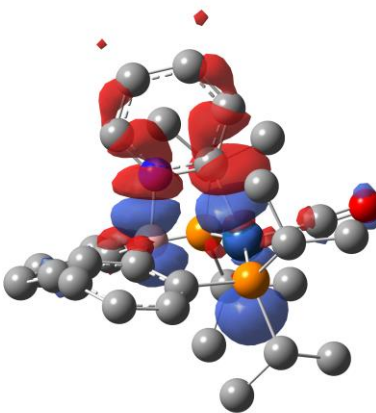
**Table S3.** ETS-NOCV analysis of the interaction between 2-pyridyl anion and the formally positive charged rest of the molecule. The two largest decomposed NOCV contributions ( $\Delta\rho_1$  and  $\Delta\rho_2$ ) constructed with the density isosurface contour value of 0.002 are shown. Blue and red surfaces identify regions of electron density accumulation and depletion, respectively. It is clear the electrons “flow” from CN anion to metal cation.

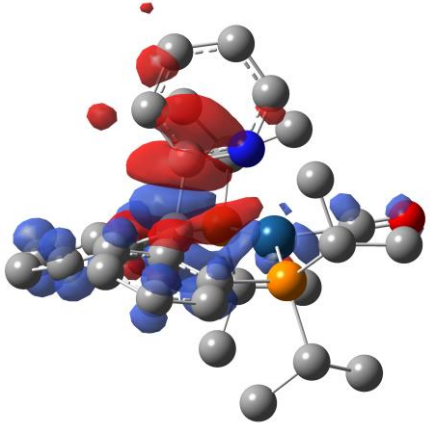
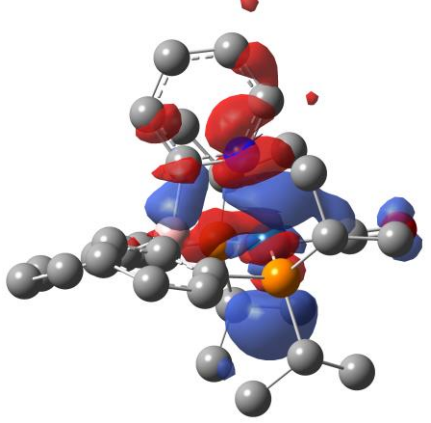
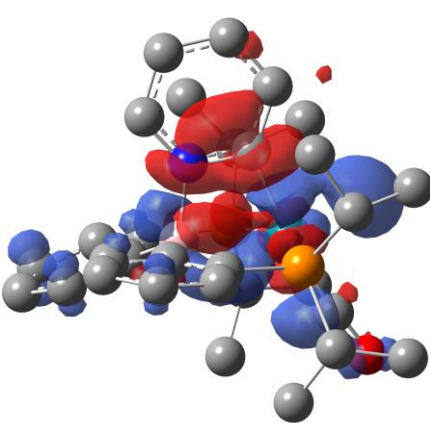
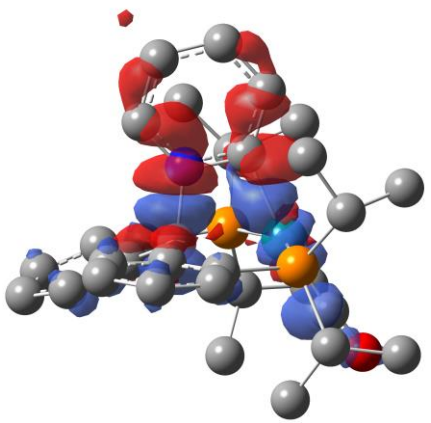
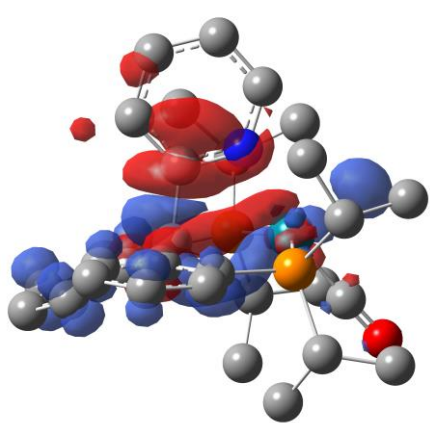
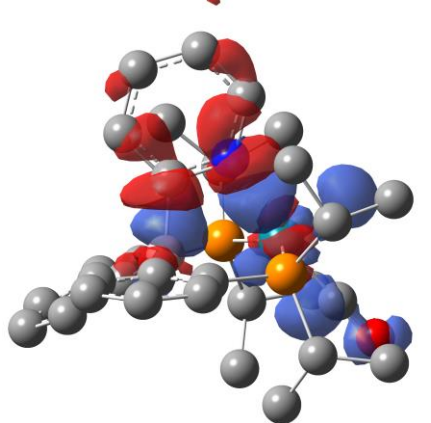
	Sum of decomposition energy by ETS-NOCV (kcal/mol)	The Two Major Components	
<b>1RhC</b>	-243.2	 $\Delta\rho_1 = -105 \text{ kcal/mol}$	 $\Delta\rho_2 = -76 \text{ kcal/mol}$
<b>1RhN</b>	-232.0	 $\Delta\rho_1 = -153 \text{ kcal/mol}$	 $\Delta\rho_2 = -30 \text{ kcal/mol}$

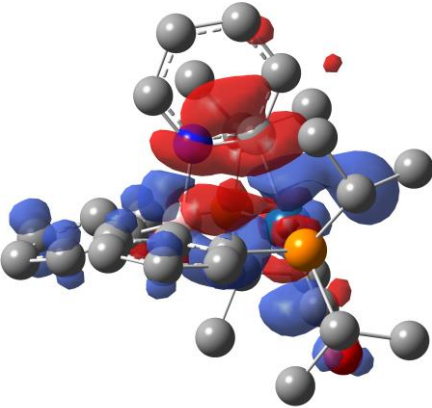
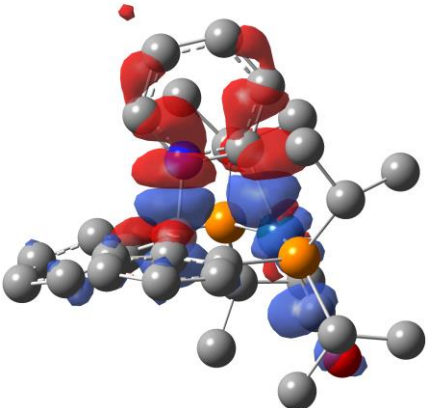
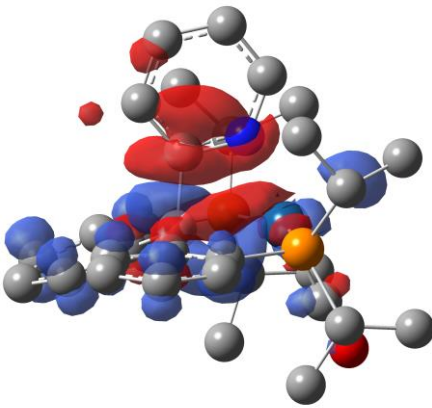
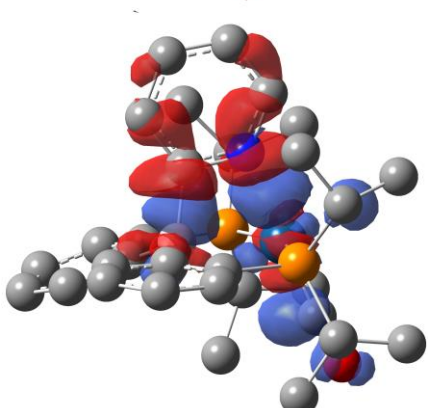
<b>1IrC</b>	-343.7	 $\Delta \rho 1 = -155 \text{ kcal/mol}$	 $\Delta \rho 2 = -117 \text{ kcal/mol}$
<b>1IrN</b>	-255.3	 $\Delta \rho 1 = -150 \text{ kcal/mol}$	 $\Delta \rho 2 = -51 \text{ kcal/mol}$
<b>2RhC</b>	-310.9	 $\Delta \rho 1 = -131 \text{ kcal/mol}$	 $\Delta \rho 2 = -106 \text{ kcal/mol}$

<b>2RhN</b>	-271.0	 $\Delta \rho 1 = -157 \text{ kcal/mol}$	 $\Delta \rho 2 = -56 \text{ kcal/mol}$
<b>2IrC</b>	-467.0	 $\Delta \rho 1 = -260 \text{ kcal/mol}$	 $\Delta \rho 2 = -111 \text{ kcal/mol}$
<b>2IrN</b>	-313.1	 $\Delta \rho 1 = -153 \text{ kcal/mol}$	 $\Delta \rho 2 = -96 \text{ kcal/mol}$



<b>3RhC</b>	-241.0	 $\Delta \rho 1 = -101 \text{ kcal/mol}$	 $\Delta \rho 2 = -83 \text{ kcal/mol}$
<b>3RhN</b>	-236.3	 $\Delta \rho 1 = -153 \text{ kcal/mol}$	 $\Delta \rho 2 = -36 \text{ kcal/mol}$
<b>3IrC</b>	-329.8	 $\Delta \rho 1 = -135 \text{ kcal/mol}$	 $\Delta \rho 2 = -129 \text{ kcal/mol}$

<b>3IrN</b>	-259.6	 $\Delta \rho 1 = -148 \text{ kcal/mol}$	 $\Delta \rho 2 = -58 \text{ kcal/mol}$
<b>4RhC</b>	-282.6	 $\Delta \rho 1 = -125 \text{ kcal/mol}$	 $\Delta \rho 2 = -97 \text{ kcal/mol}$
<b>4RhN</b>	-274.6	 $\Delta \rho 1 = -159 \text{ kcal/mol}$	 $\Delta \rho 2 = -65 \text{ kcal/mol}$

<b>4IrC</b>	-366.9	 $\Delta \rho 1 = -162 \text{ kcal/mol}$	 $\Delta \rho 2 = -131 \text{ kcal/mol}$
<b>4IrN</b>	-297.1	 $\Delta \rho 1 = -154 \text{ kcal/mol}$	 $\Delta \rho 2 = -82 \text{ kcal/mol}$

## 5. NMR Spectra.

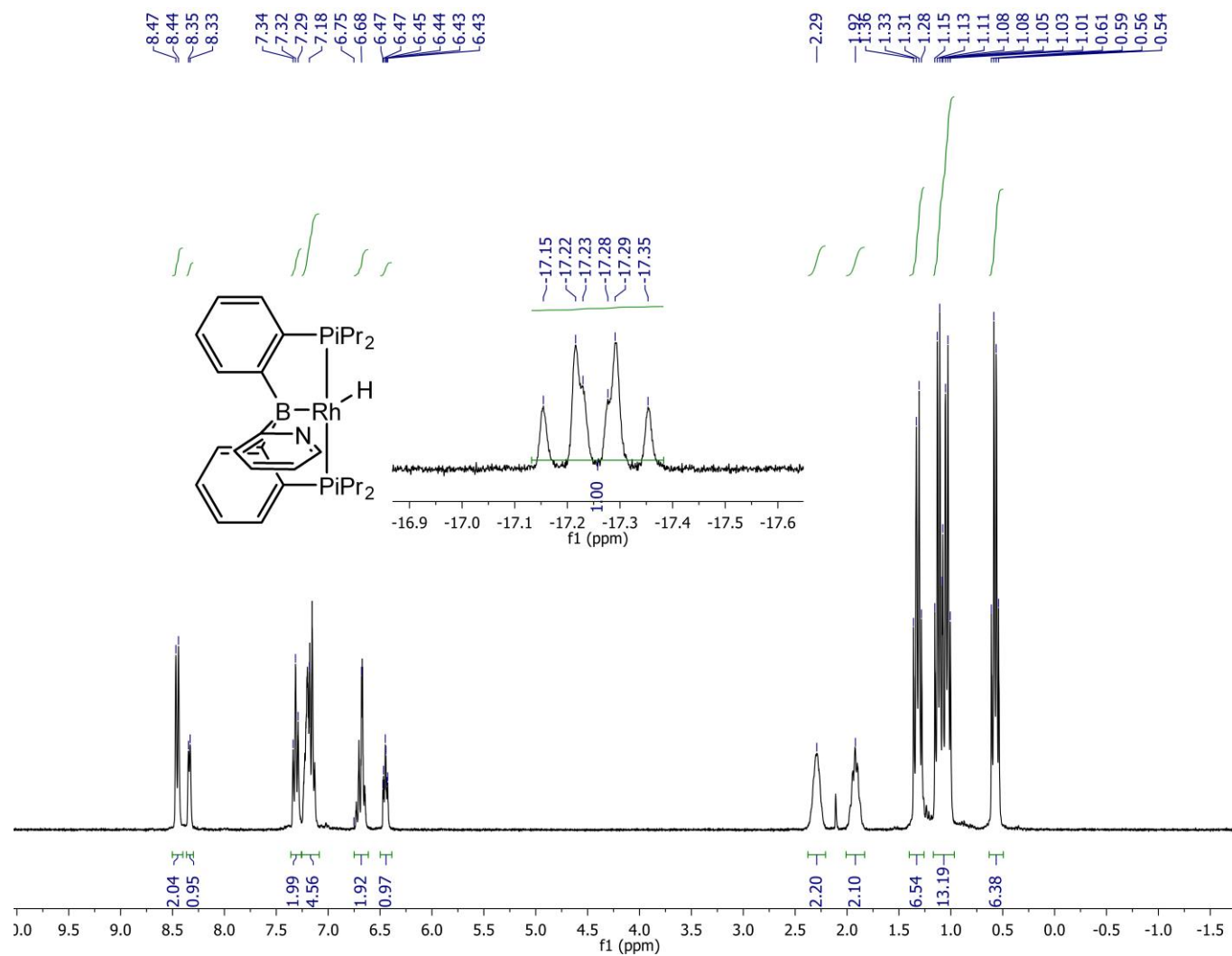


**Figure S6.**  $^1\text{H}$  NMR spectrum of **1RhN** in  $\text{C}_6\text{D}_6$  measured on a 300 MHz Mercury NMR

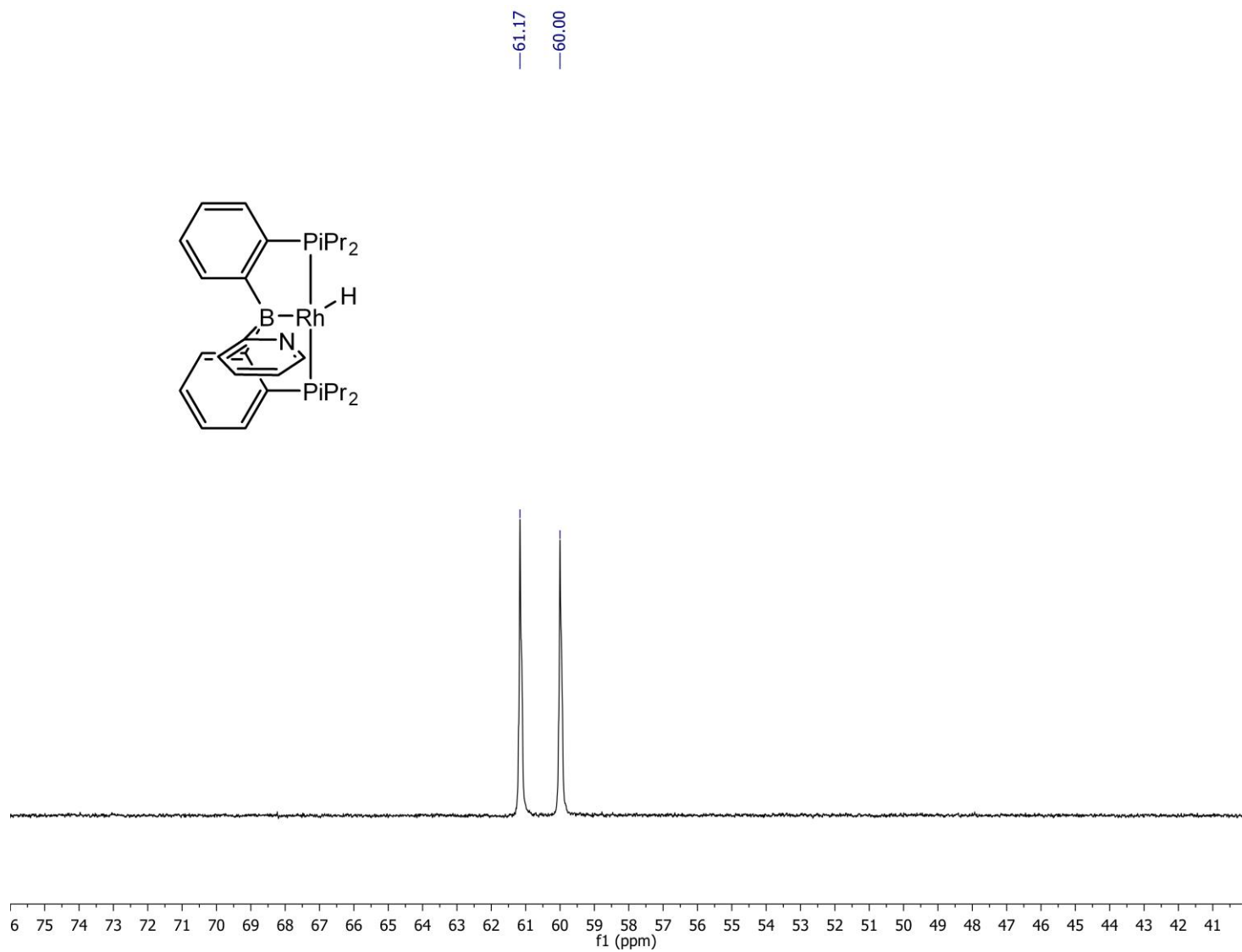


**Figure S7.**  $^{31}\text{P}\{^1\text{H}\}$  NMR spectrum of **1RhN** in  $\text{C}_6\text{D}_6$  measured on a 300 MHz Mercury NMR

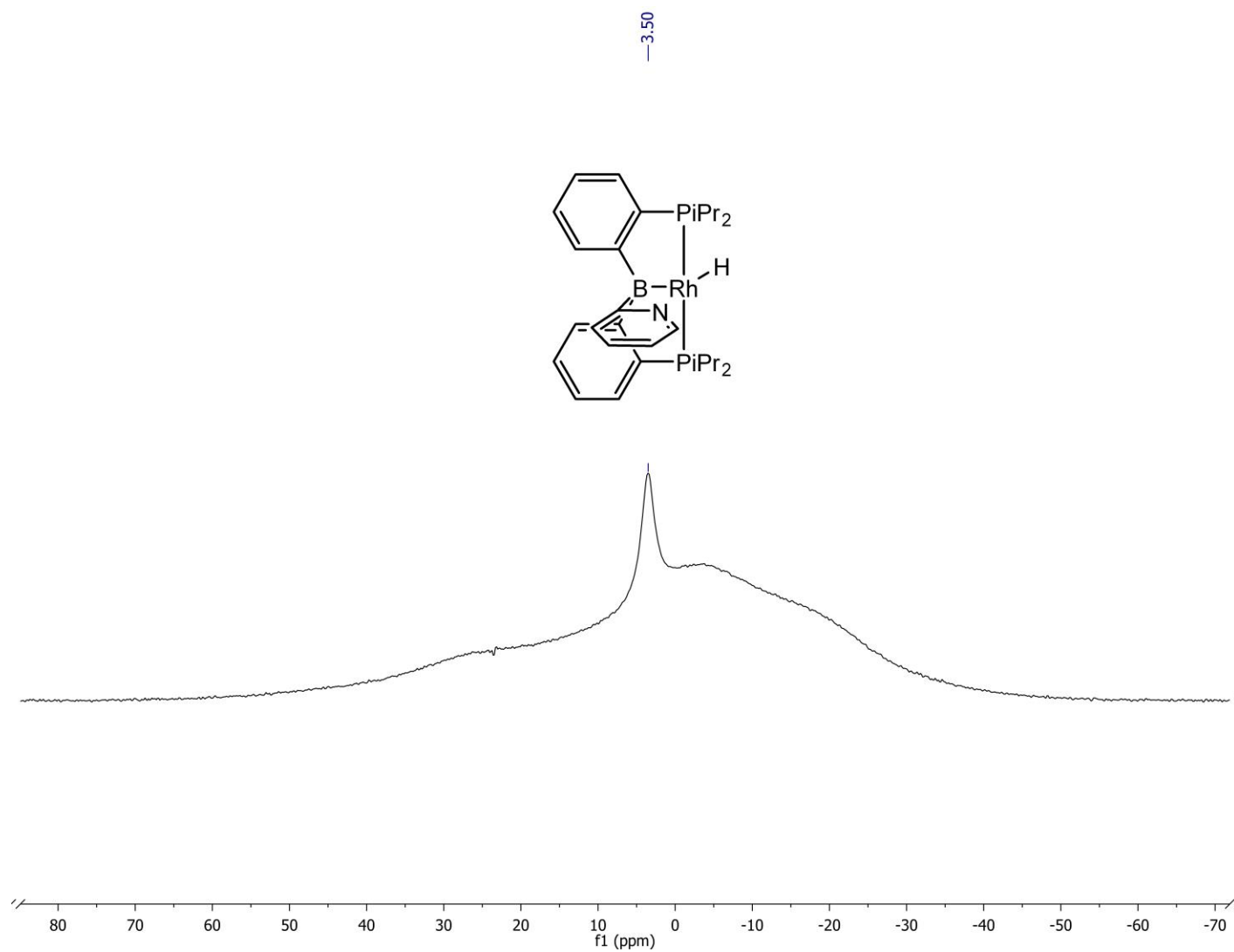


**Figure S8.**  $^{11}\text{B}\{^1\text{H}\}$  NMR spectrum of **1RhN** in  $\text{C}_6\text{D}_6$  measured on a 400 MHz Varian NMR

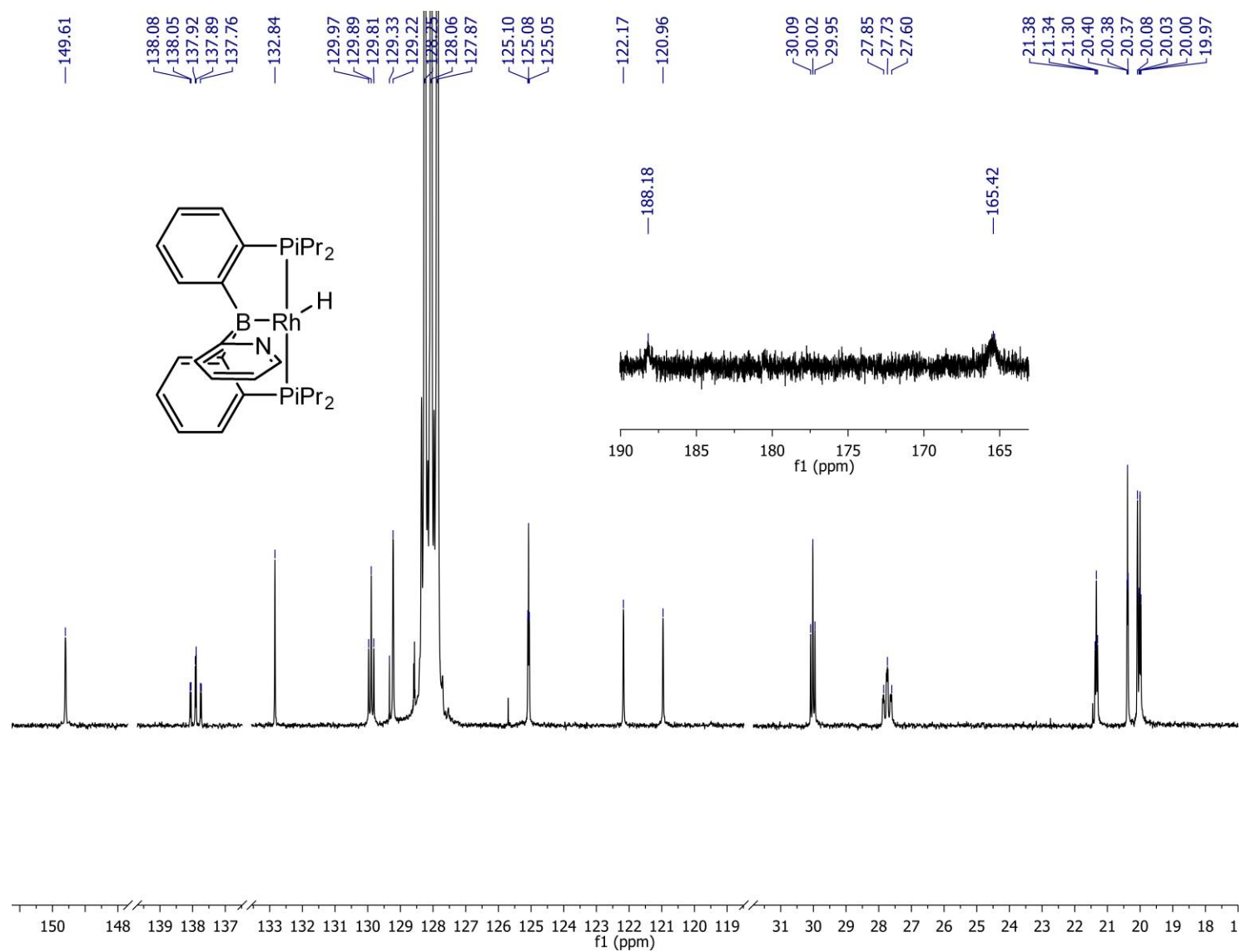


**Figure S9.**  $^{13}\text{C}\{^1\text{H}\}$  NMR of **1RhN** in  $\text{C}_6\text{D}_6$  measured on a 500 MHz Varian NMR.

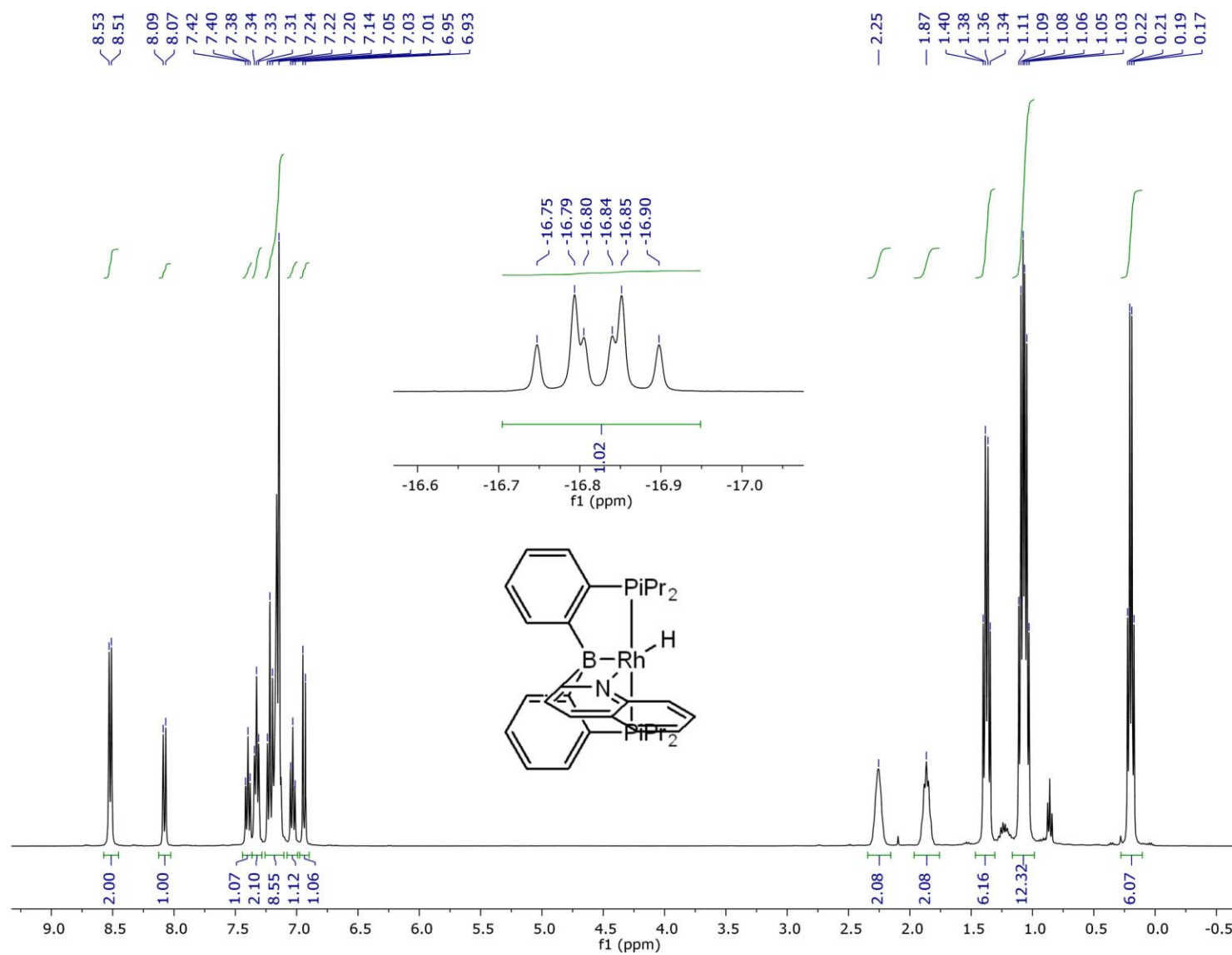


**Figure S10.** <sup>1</sup>H NMR spectrum of **1RhNq** in C<sub>6</sub>D<sub>6</sub> measured on a 400 MHz Bruker NMR



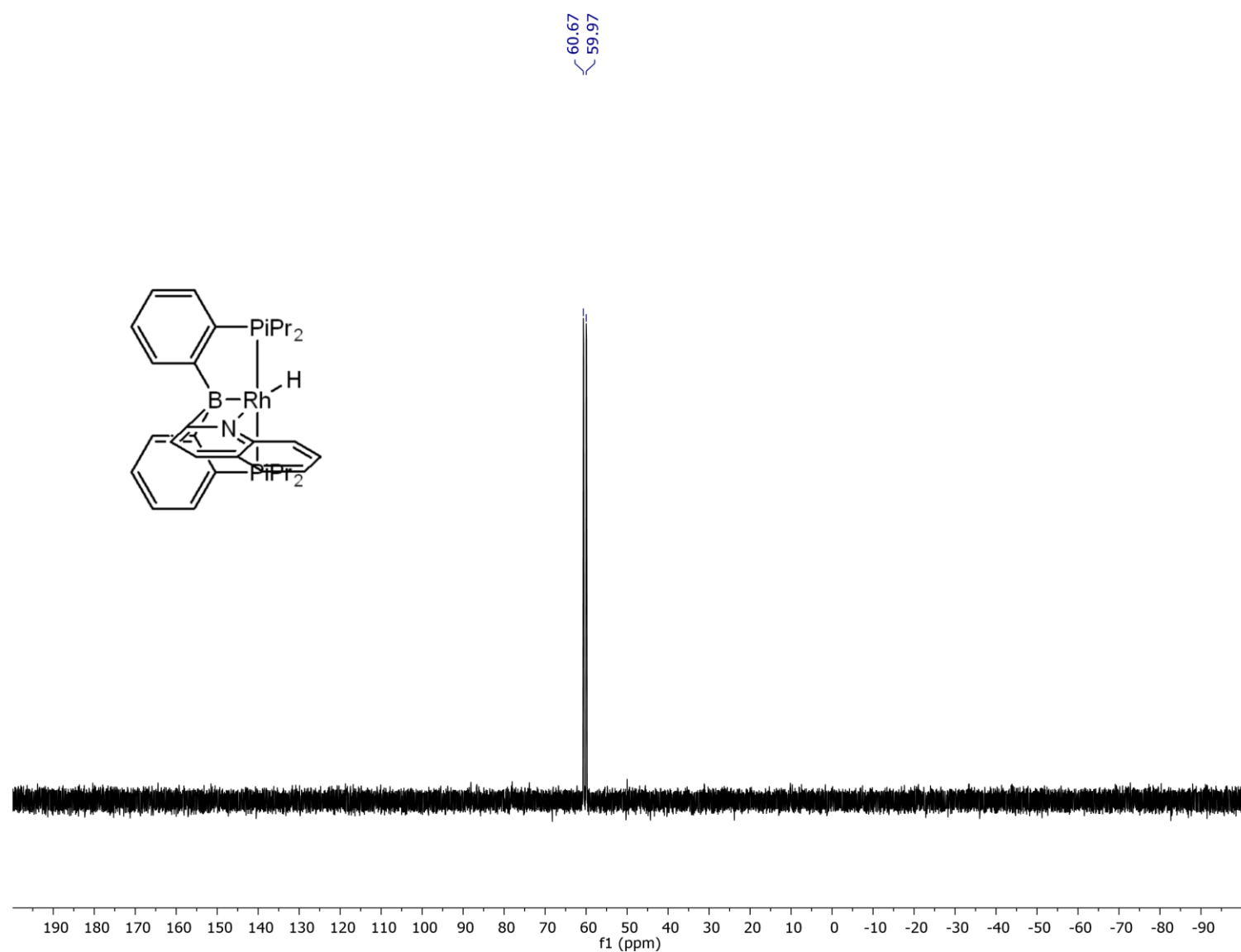


**Figure S11.**  $^{31}\text{P}\{^1\text{H}\}$  NMR spectrum of **1RhNq** in  $\text{C}_6\text{D}_6$  measured on a 300 MHz Mercury NMR

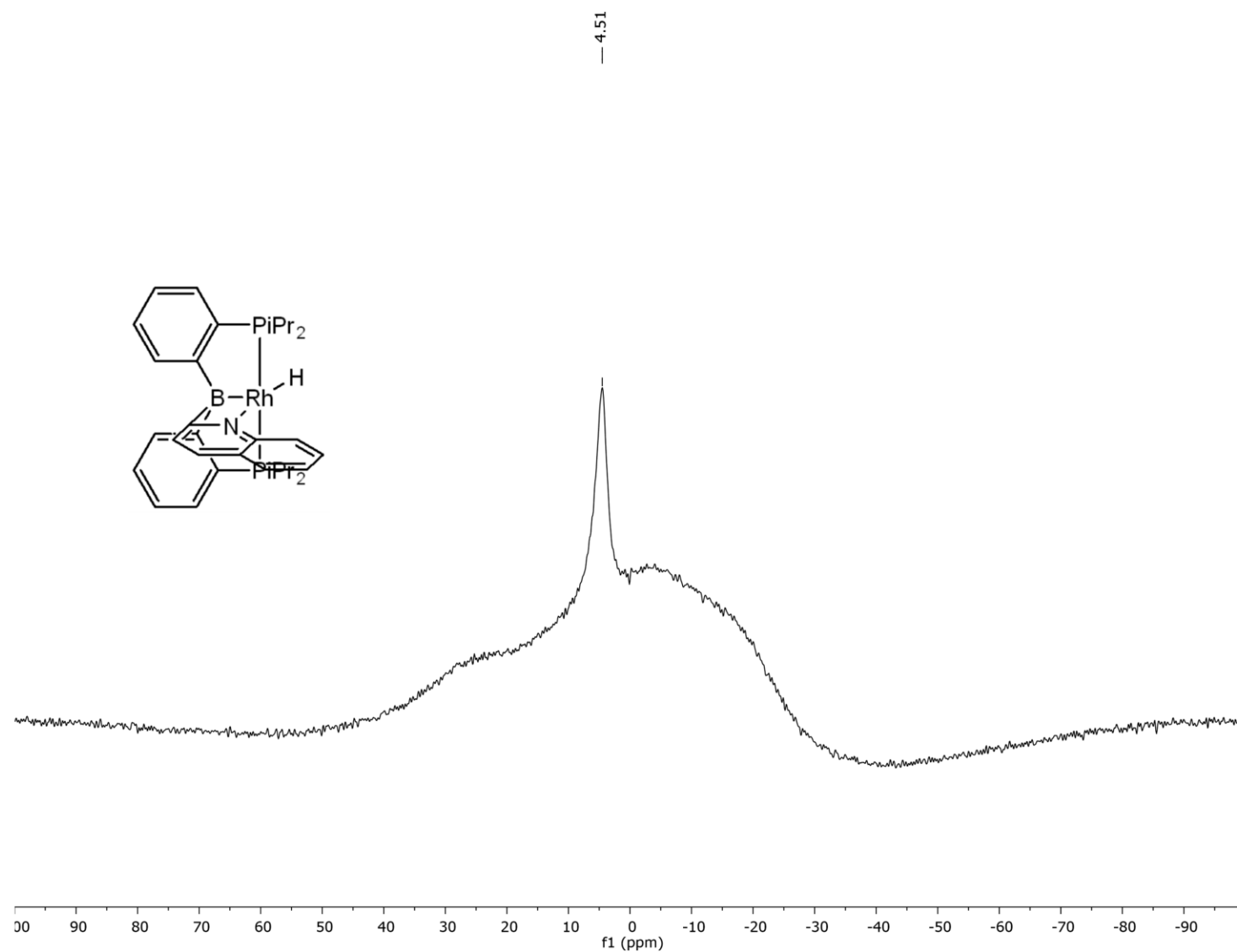


**Figure S12.**  $^{11}\text{B}\{^1\text{H}\}$  NMR spectrum of **1RhNq** in  $\text{C}_6\text{D}_6$  measured on a 400 MHz Varian NMR

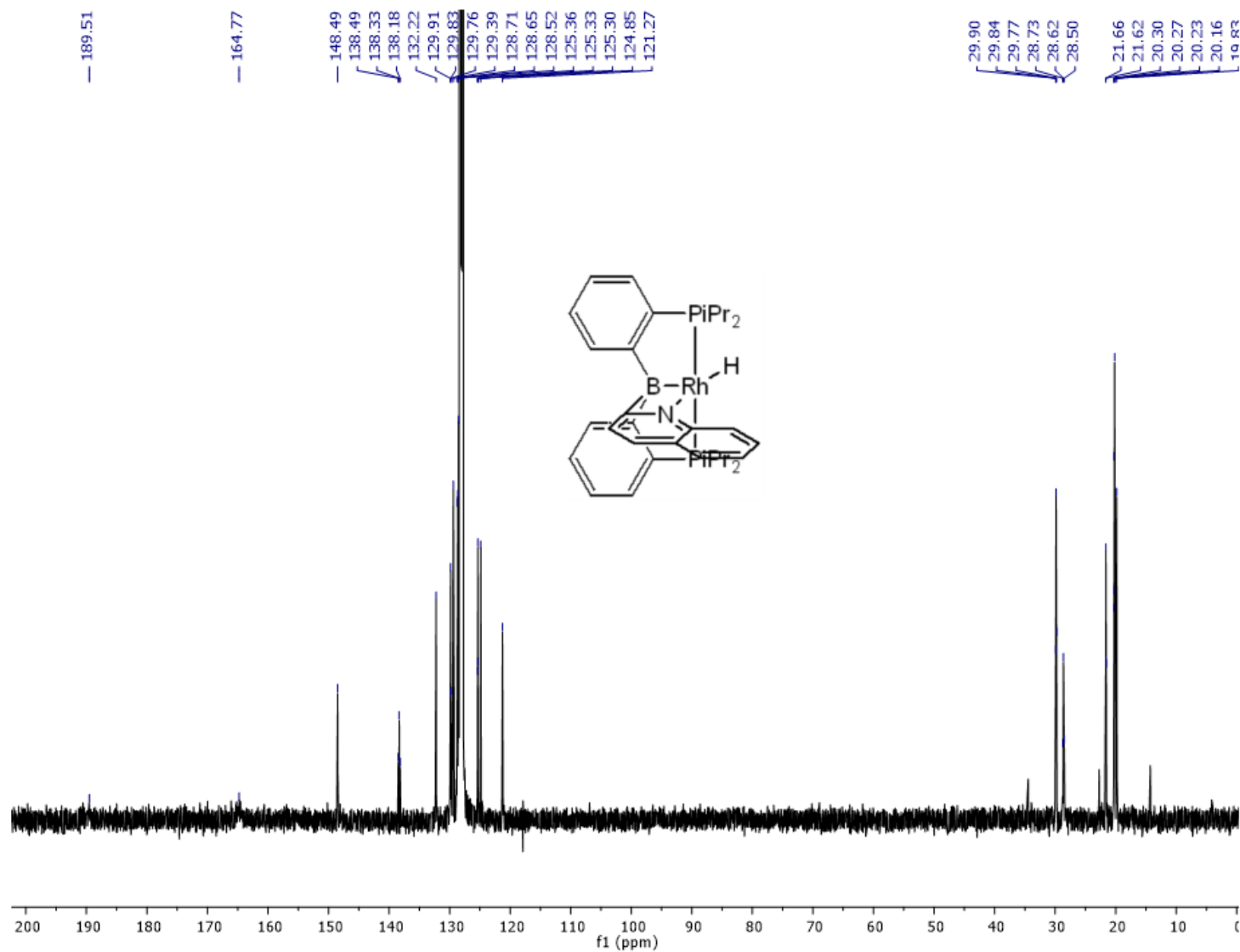


**Figure S13.**  $^{13}\text{C}\{^1\text{H}\}$  NMR of **1RhNq** in  $\text{C}_6\text{D}_6$  measured on a 500 MHz Varian NMR

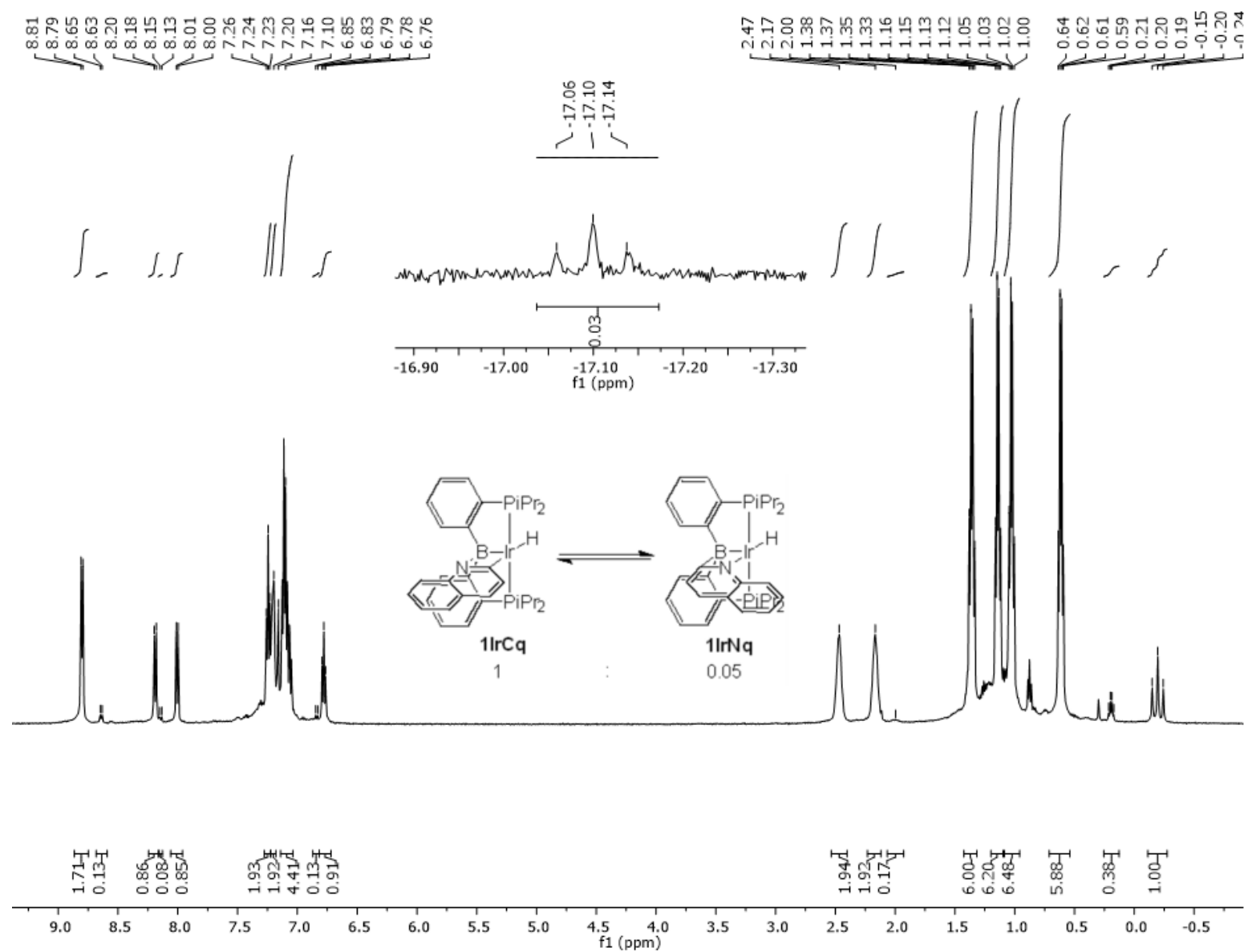


**Figure S14.**  $^1\text{H}$  NMR spectrum of **1IrCq/1IrNq** in  $\text{C}_6\text{D}_6$  measured on a 500 MHz Varian NMR

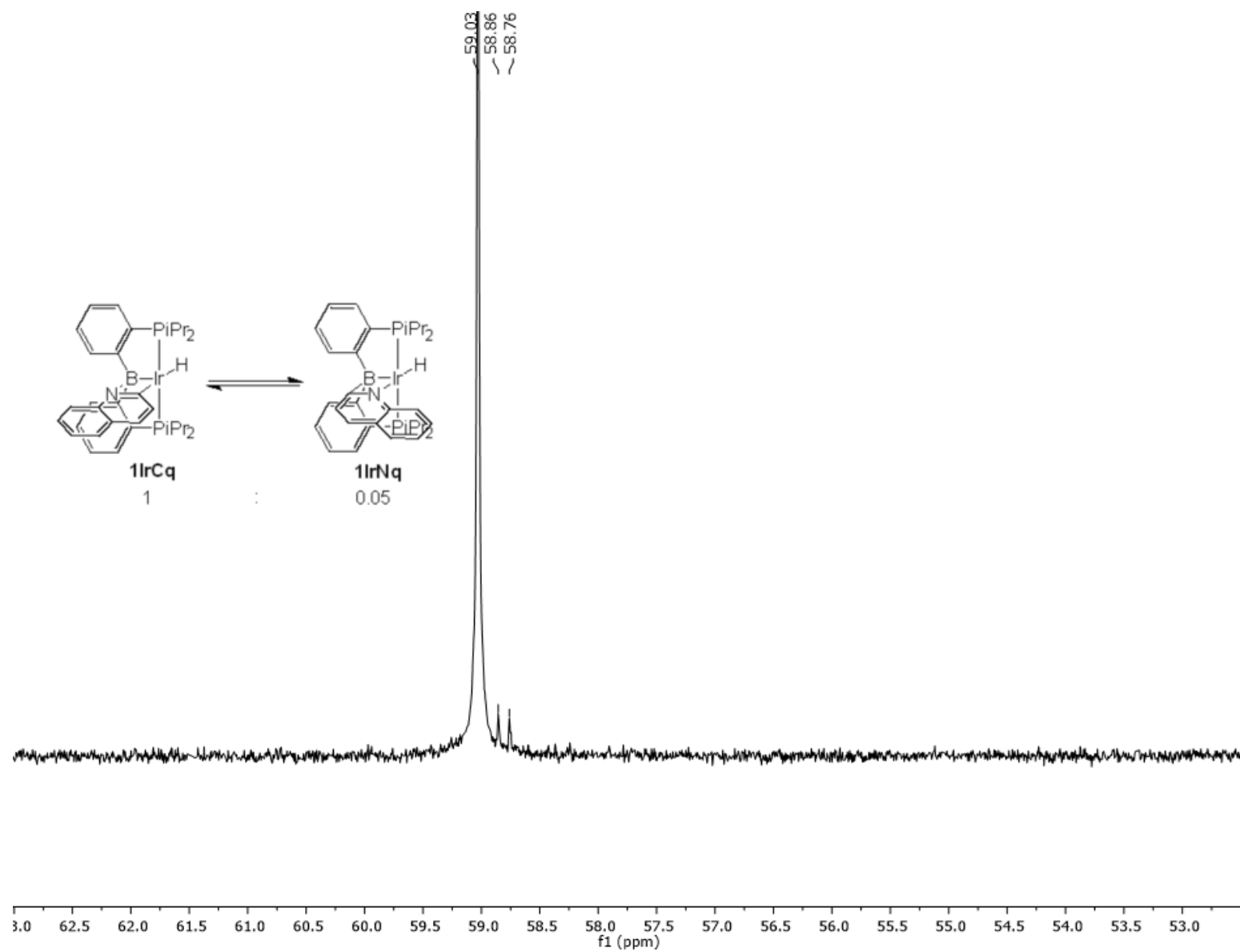


**Figure S15.**  $^{31}\text{P}$  NMR spectrum (with selected  $^1\text{H}$  decoupled) of  $1\text{IrCq}/1\text{IrNq}$  in  $\text{C}_6\text{D}_6$  measured on a 500 MHz Varian NMR

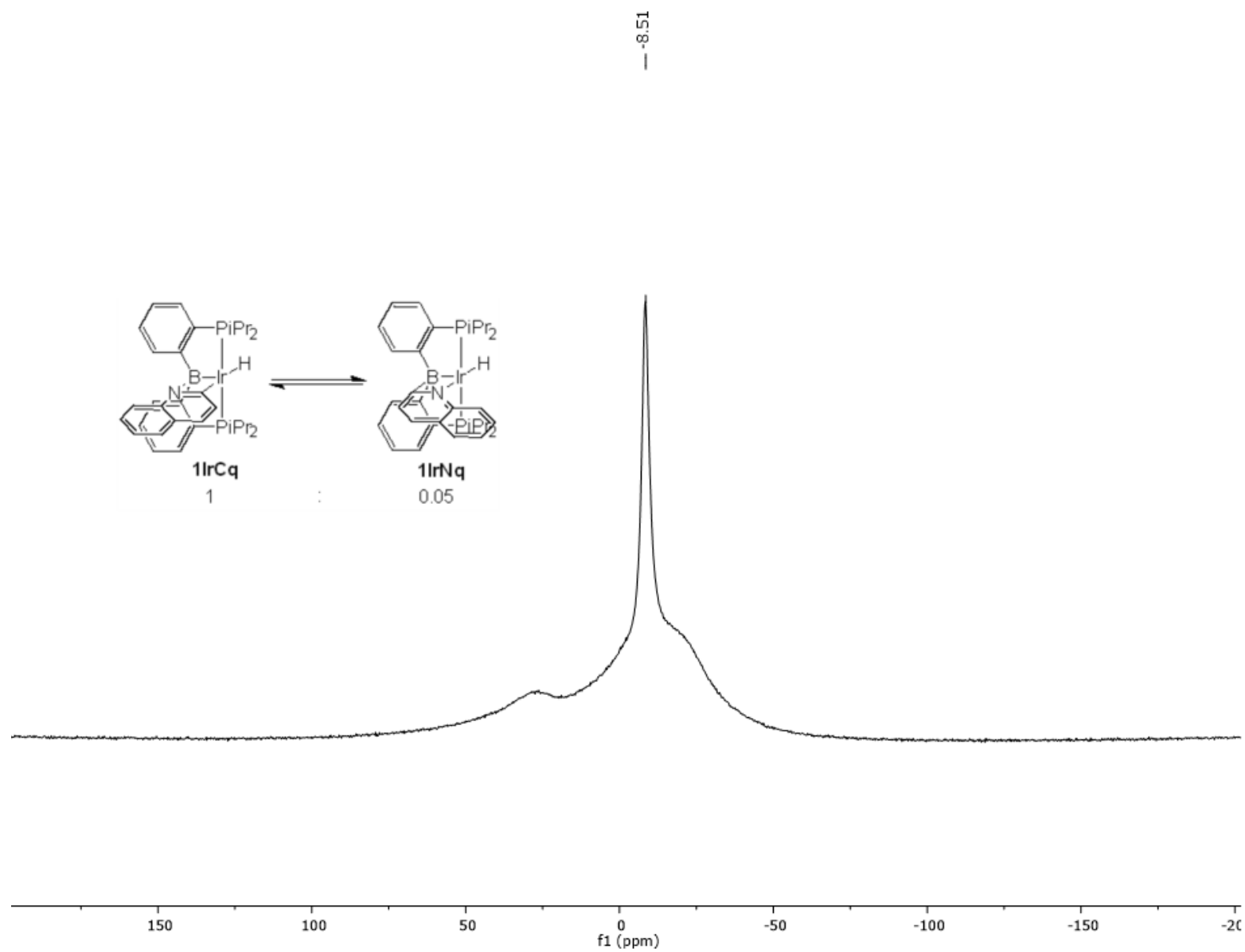


**Figure S16.**  $^{11}\text{B}\{^1\text{H}\}$  NMR spectrum of **1IrCq/1IrNq** in  $\text{C}_6\text{D}_6$  measured on a 400 MHz Bruker NMR

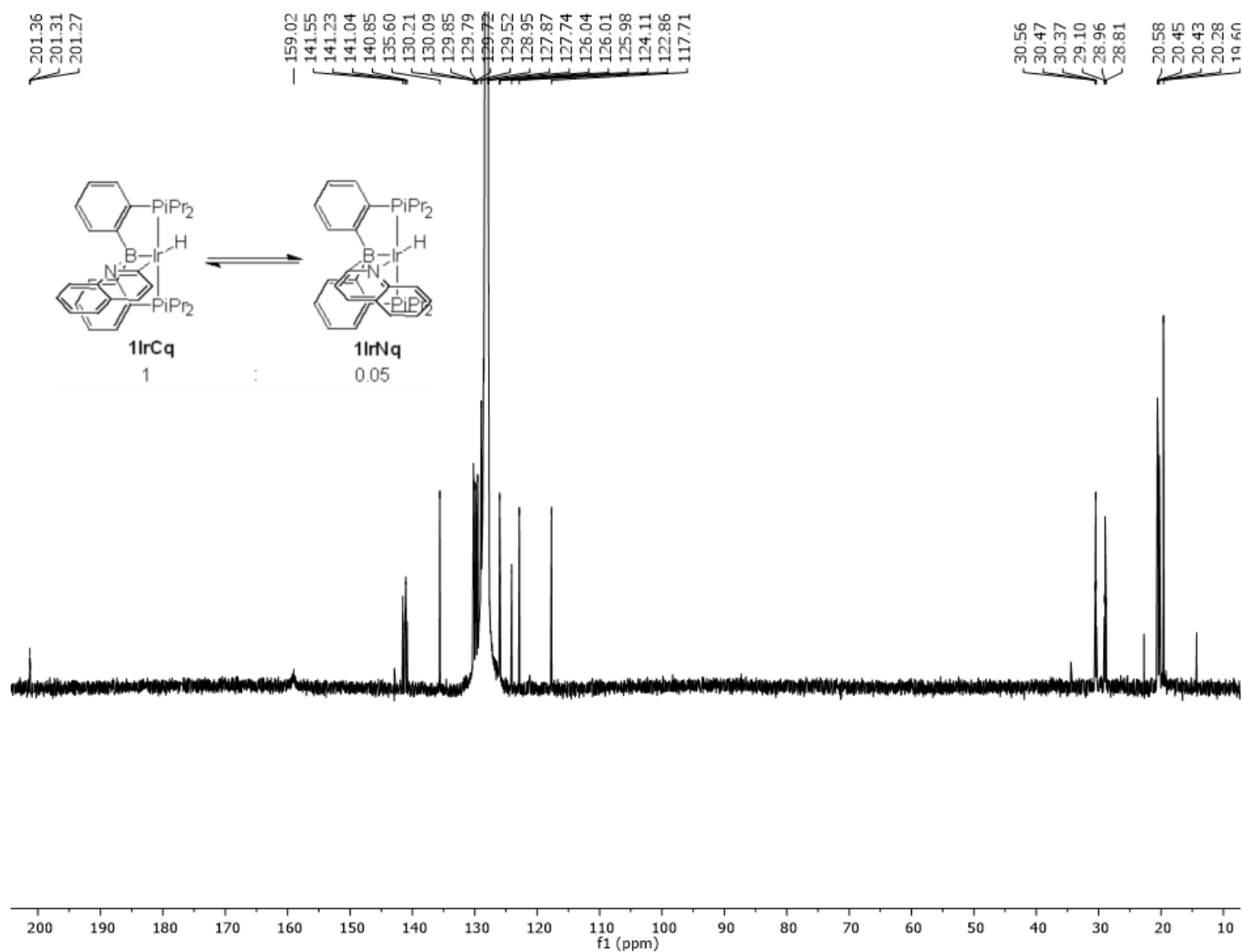


**Figure S17.**  $^{13}\text{C}\{^1\text{H}\}$  NMR spectrum of **1IrCq/1IrNq** in  $\text{C}_6\text{D}_6$  measured on a 500 MHz Varian NMR

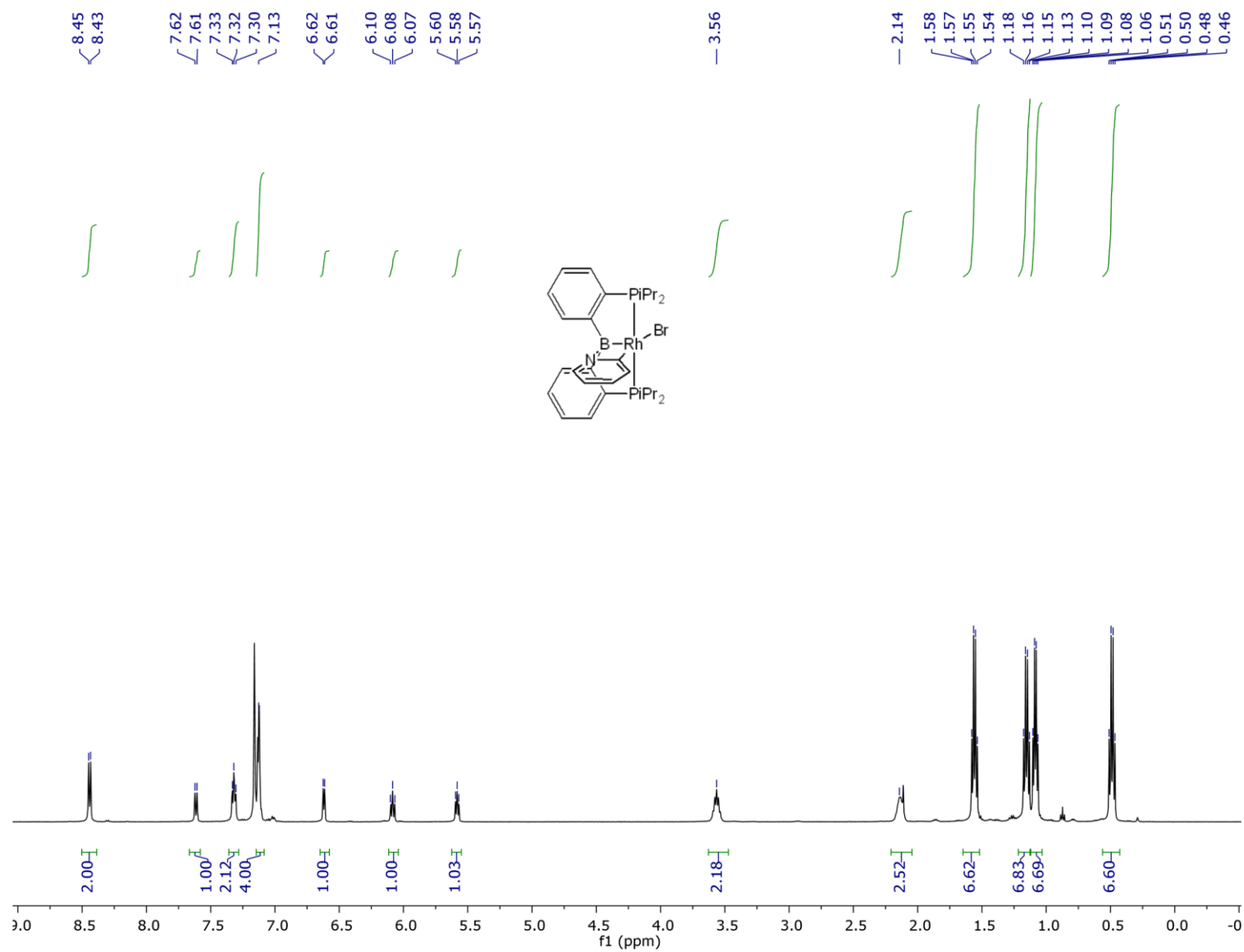


**Figure S18.**  $^1\text{H}$  NMR spectrum of **2RhC** in  $\text{C}_6\text{D}_6$  measured on a 500 MHz Varian NMR



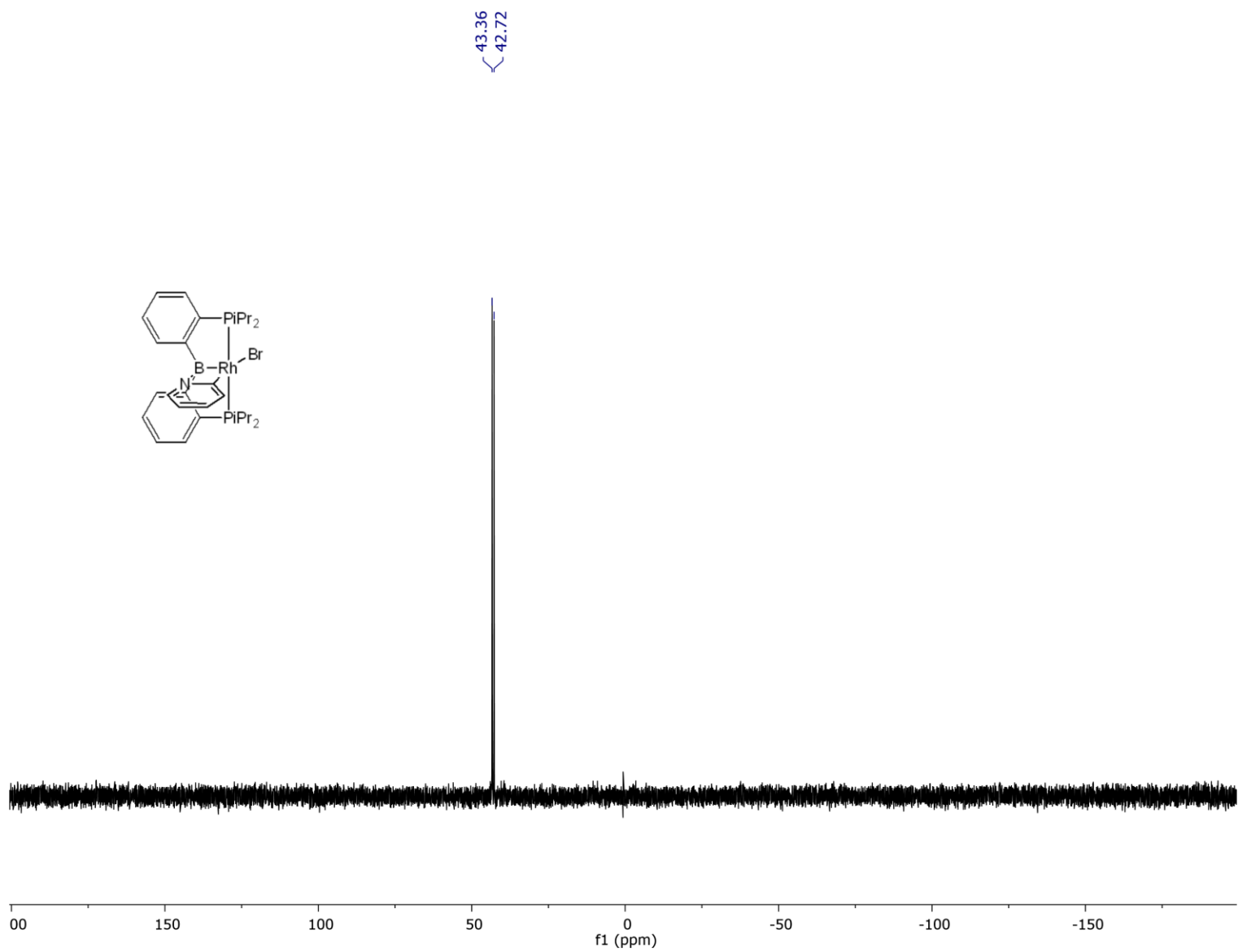


**Figure S19.**  $^{31}\text{P}\{^1\text{H}\}$  NMR spectrum of **2RhC** in  $\text{C}_6\text{D}_6$  measured on a 500 MHz Varian NMR

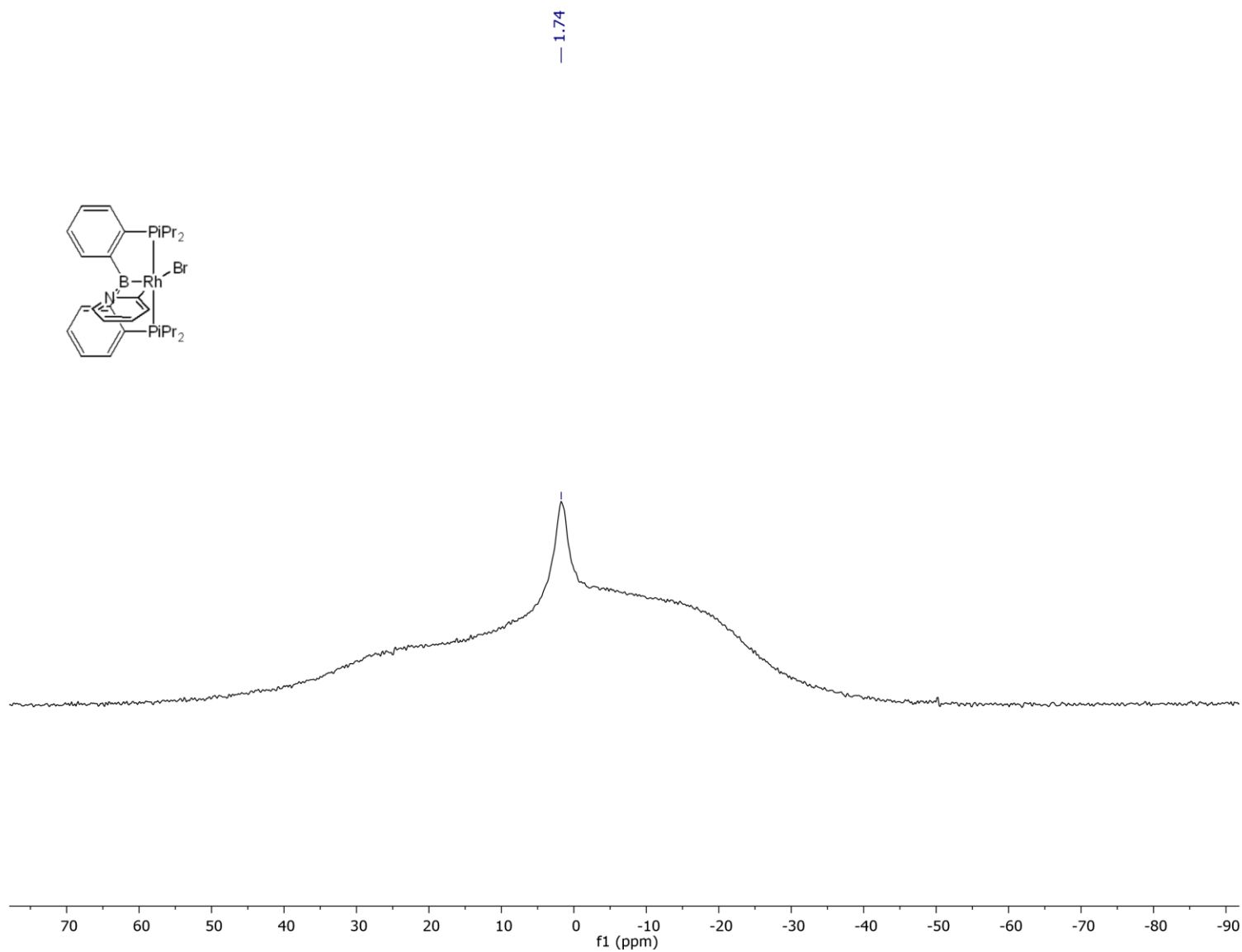


**Figure S20.**  $^{11}\text{B}\{^1\text{H}\}$  NMR spectrum of **2RhC** in  $\text{C}_6\text{D}_6$  measured on a 400 MHz Varian NMR

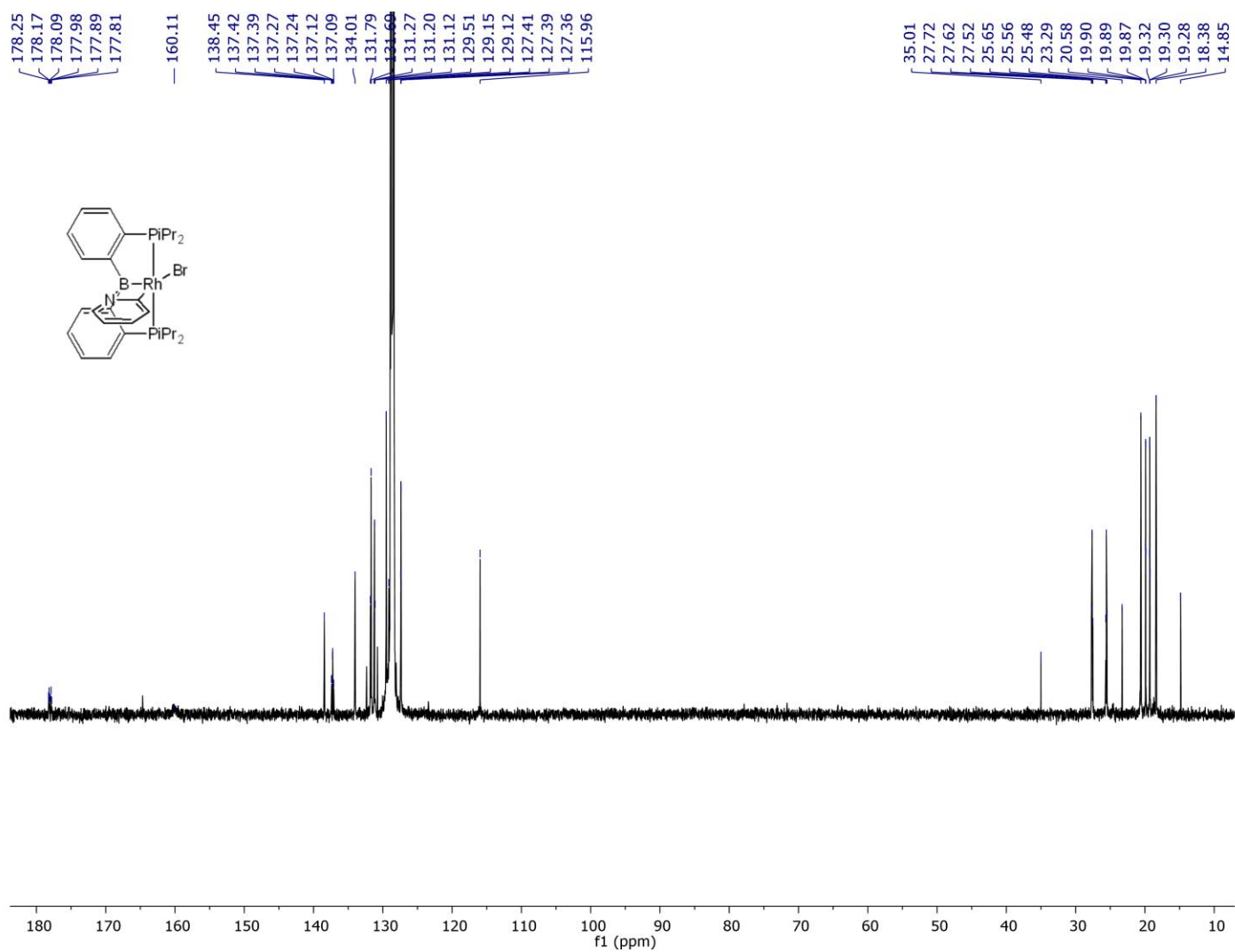


**Figure S21.**  $^{13}\text{C}\{^1\text{H}\}$  NMR of 2RhC in  $\text{C}_6\text{D}_6$  measured on a 500 MHz Varian NMR.

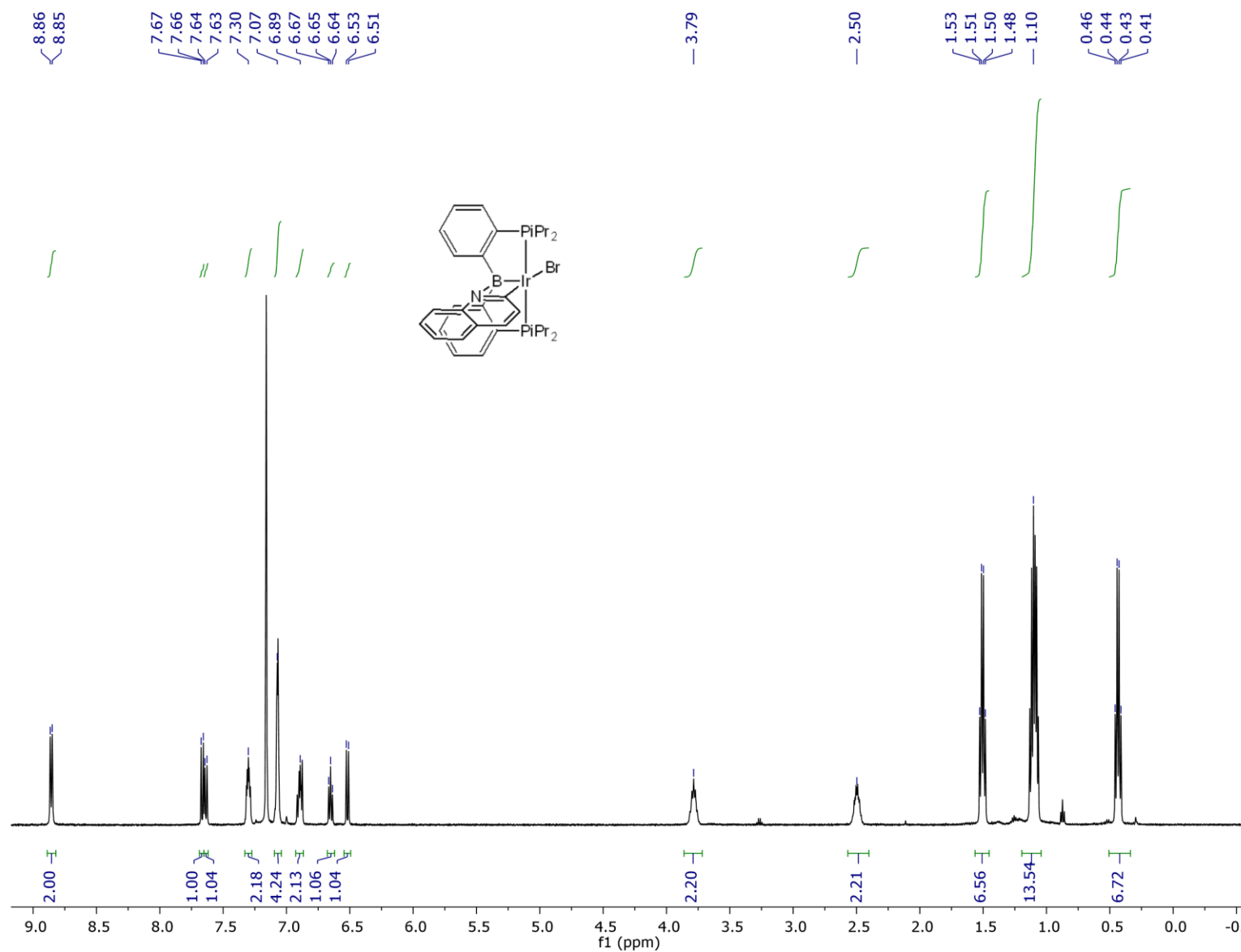


**Figure S22.**  $^1\text{H}$  NMR spectrum of **2IrCq** in  $\text{C}_6\text{D}_6$  measured on a 500 MHz Varian NMR

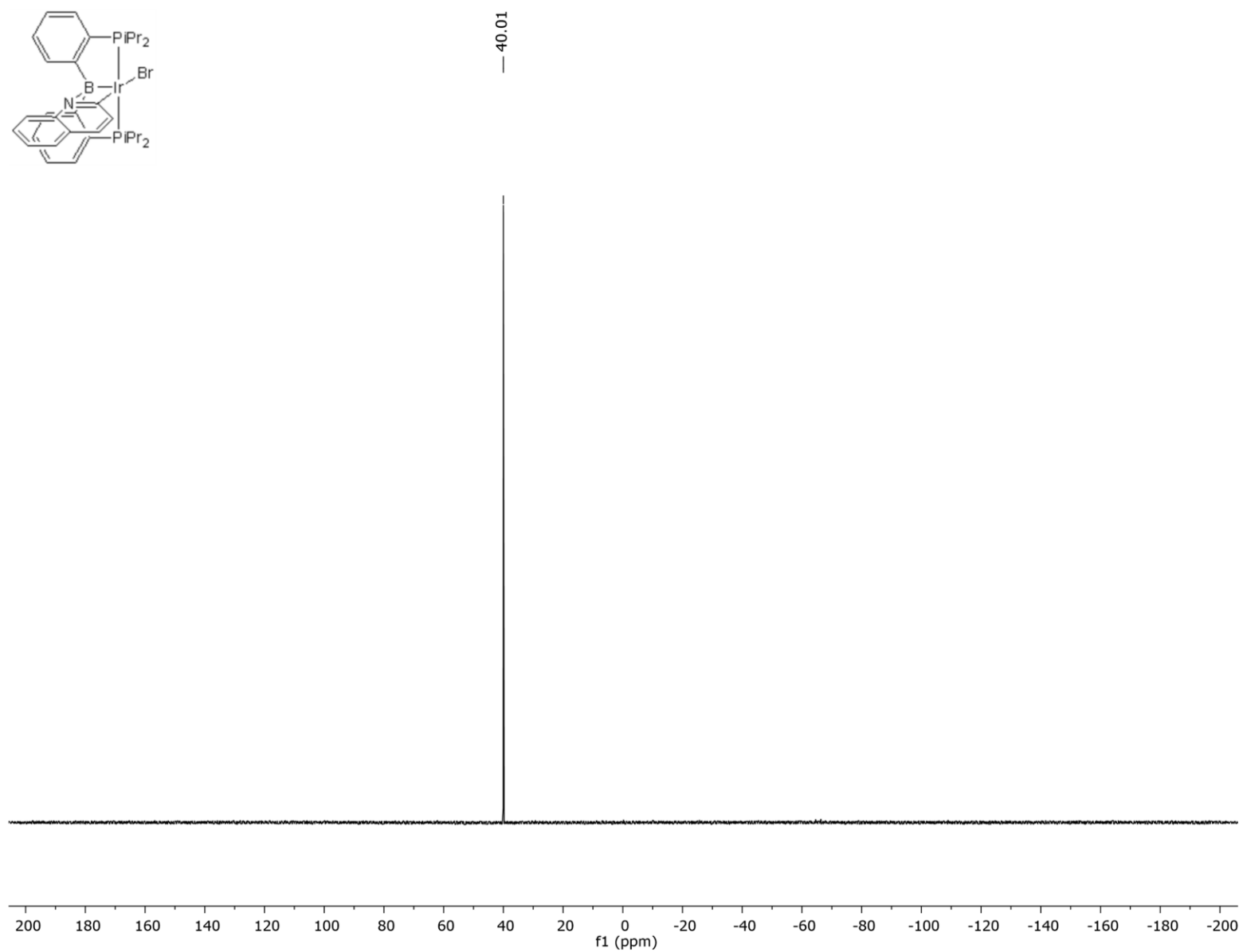


**Figure S23.**  $^{31}\text{P}\{^1\text{H}\}$  NMR spectrum of **2IrCq** in  $\text{CDCl}_3$  measured on a 500 MHz Varian NMR

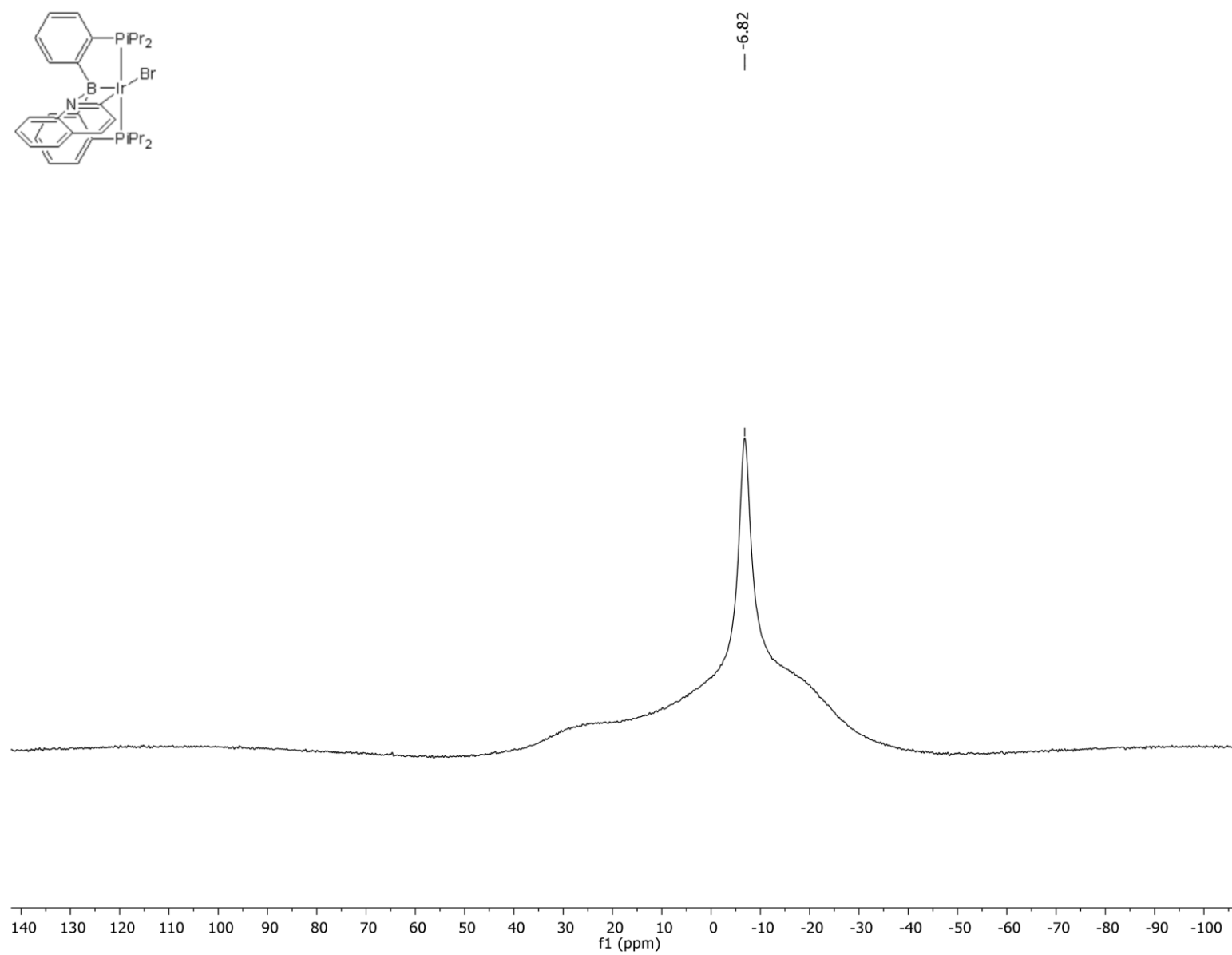


**Figure S24.**  $^{11}\text{B}\{^1\text{H}\}$  NMR spectrum of **2IrCq** in  $\text{CDCl}_3$  measured on a 400 MHz Varian NMR

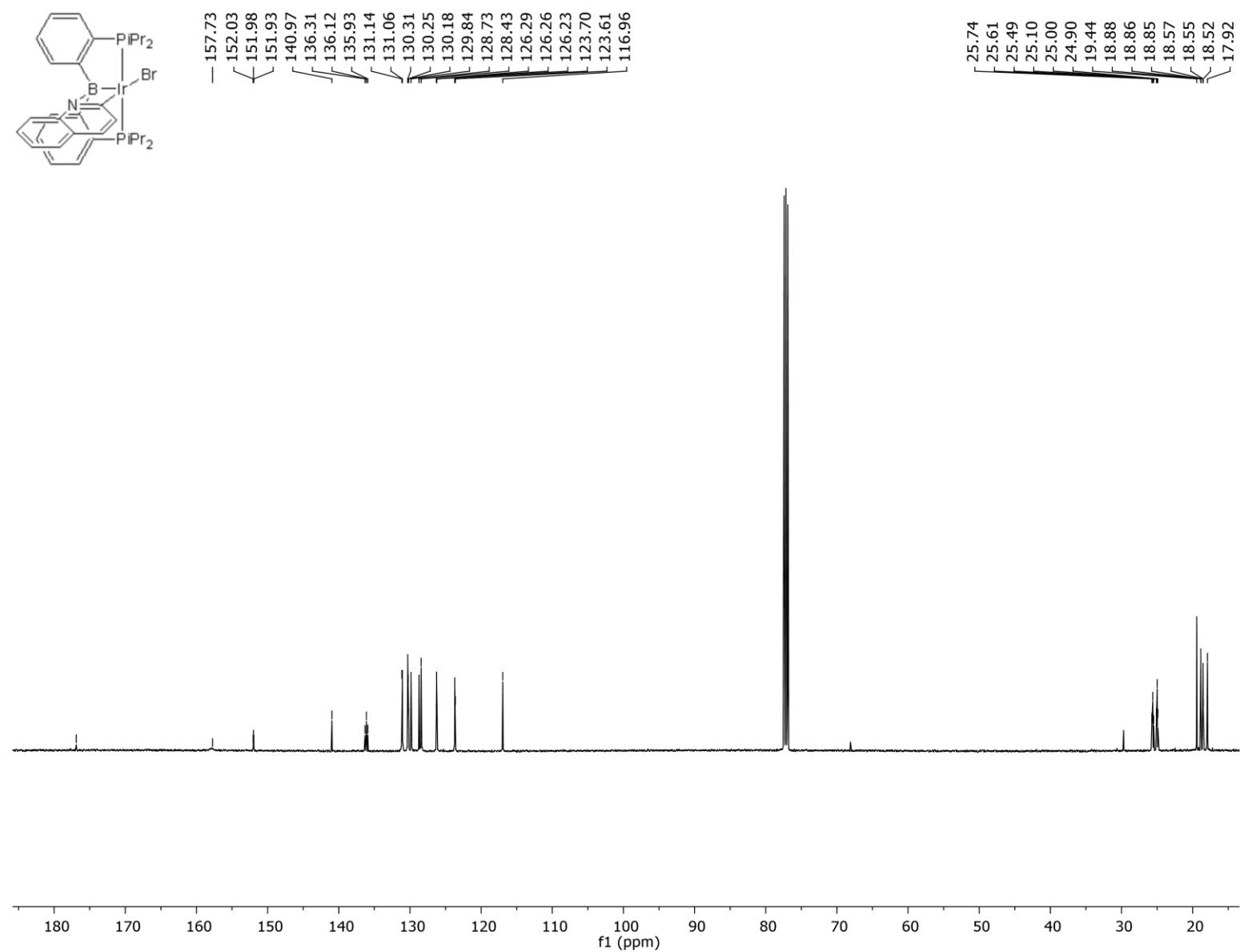


**Figure S25.** <sup>13</sup>C{<sup>1</sup>H} NMR spectrum of **2IrCq** in CDCl<sub>3</sub> measured on a 500 MHz Varian NMR

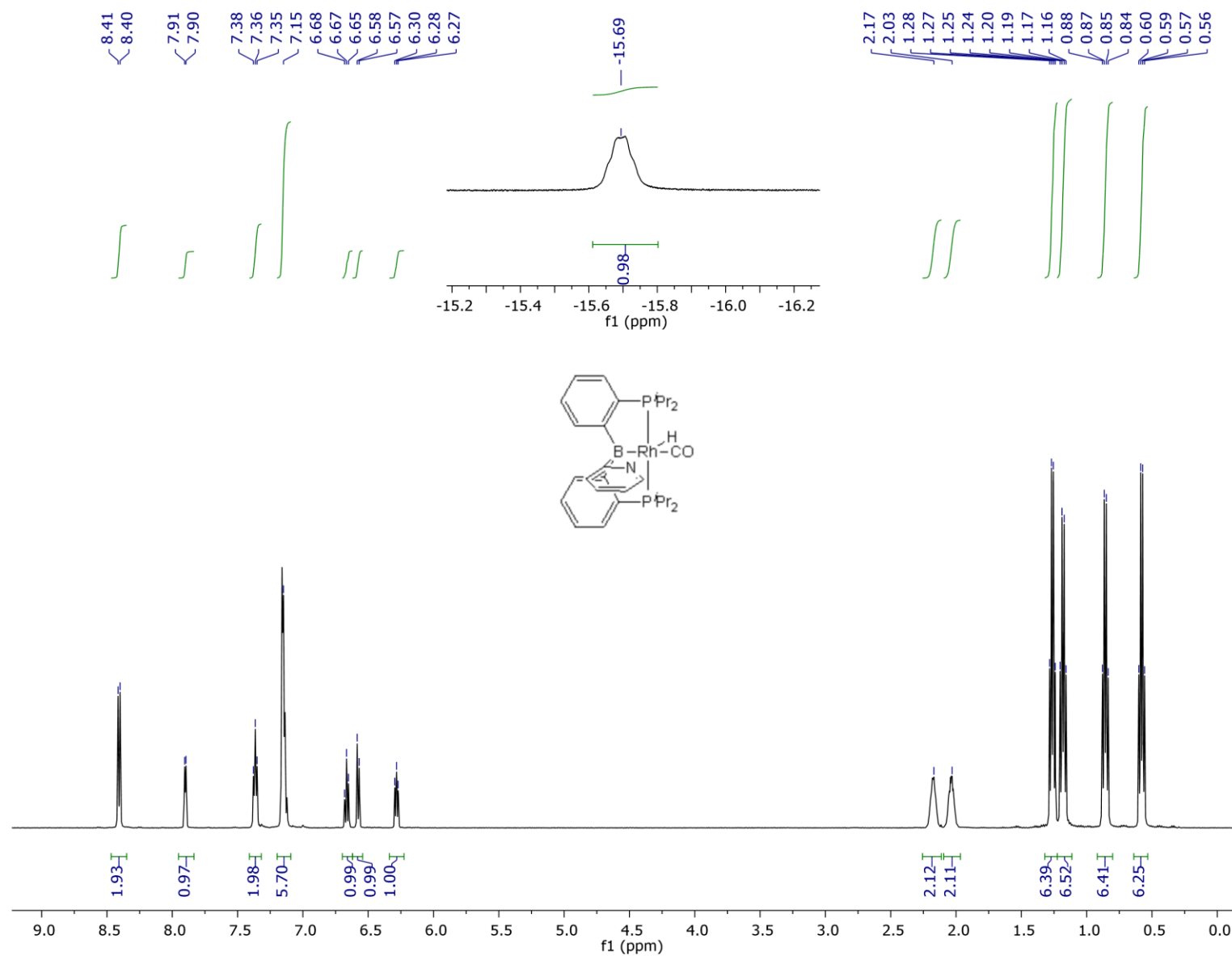


**Figure S26.**  $^1\text{H}$  NMR spectrum of **3RhN** in  $\text{C}_6\text{D}_6$  measured on a 500 MHz Varian NMR



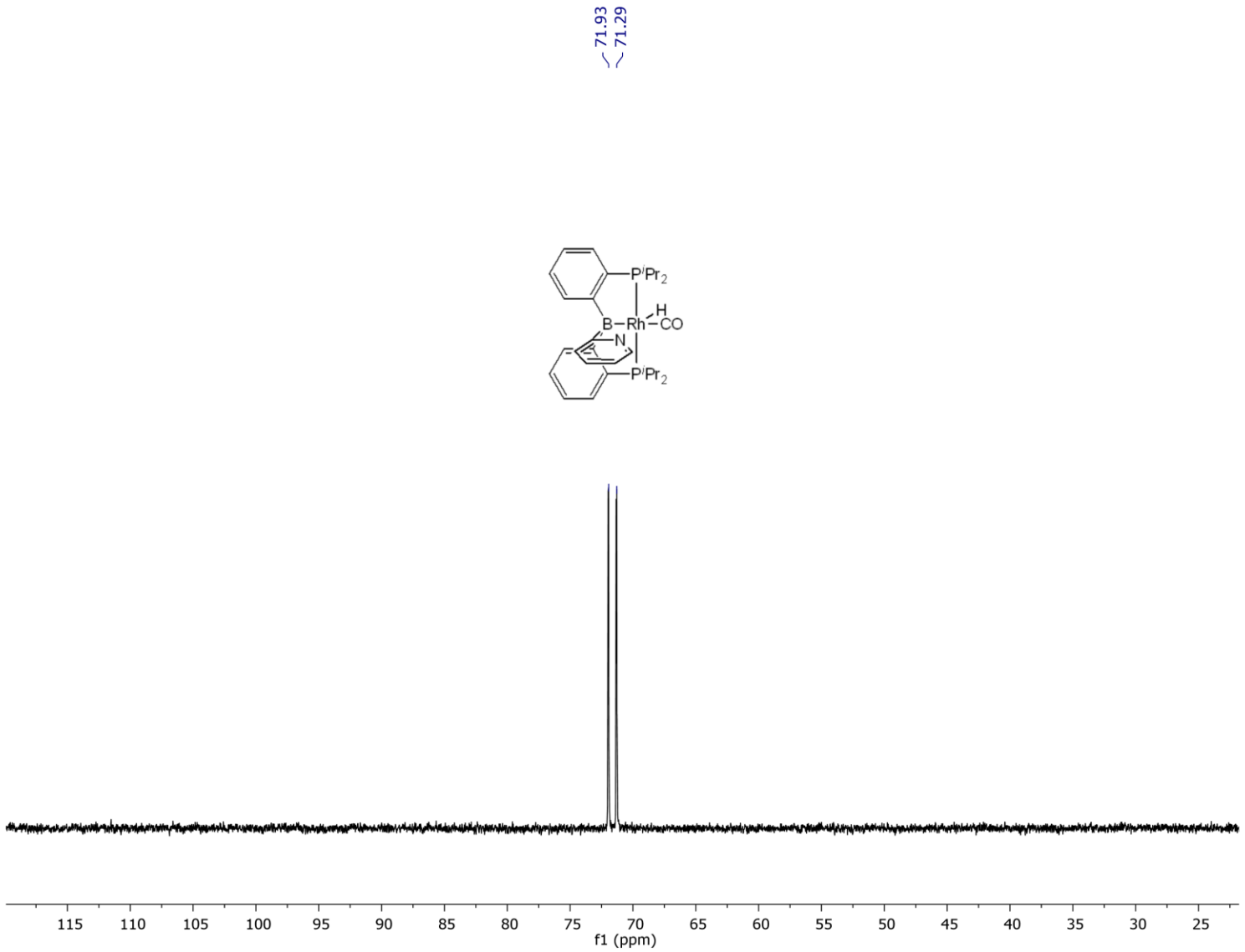


**Figure S27.**  $^{31}\text{P}\{^1\text{H}\}$  NMR spectrum of **3RhN** in  $\text{C}_6\text{D}_6$  measured on a 500 MHz Varian NMR

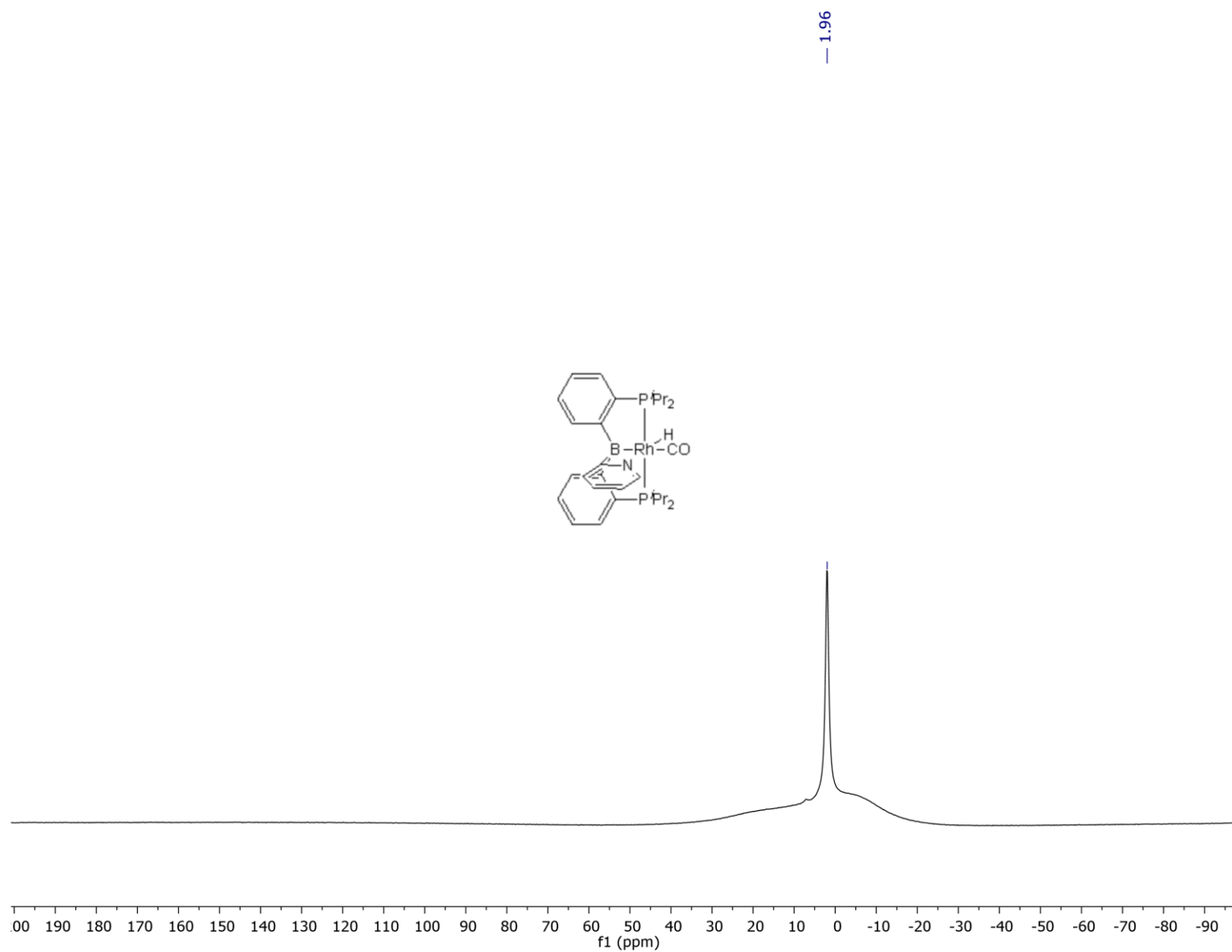


**Figure S28.**  $^{11}\text{B}\{^1\text{H}\}$  NMR spectrum of **3RhN** in  $\text{C}_6\text{D}_6$  measured on a 500 MHz Bruker NMR

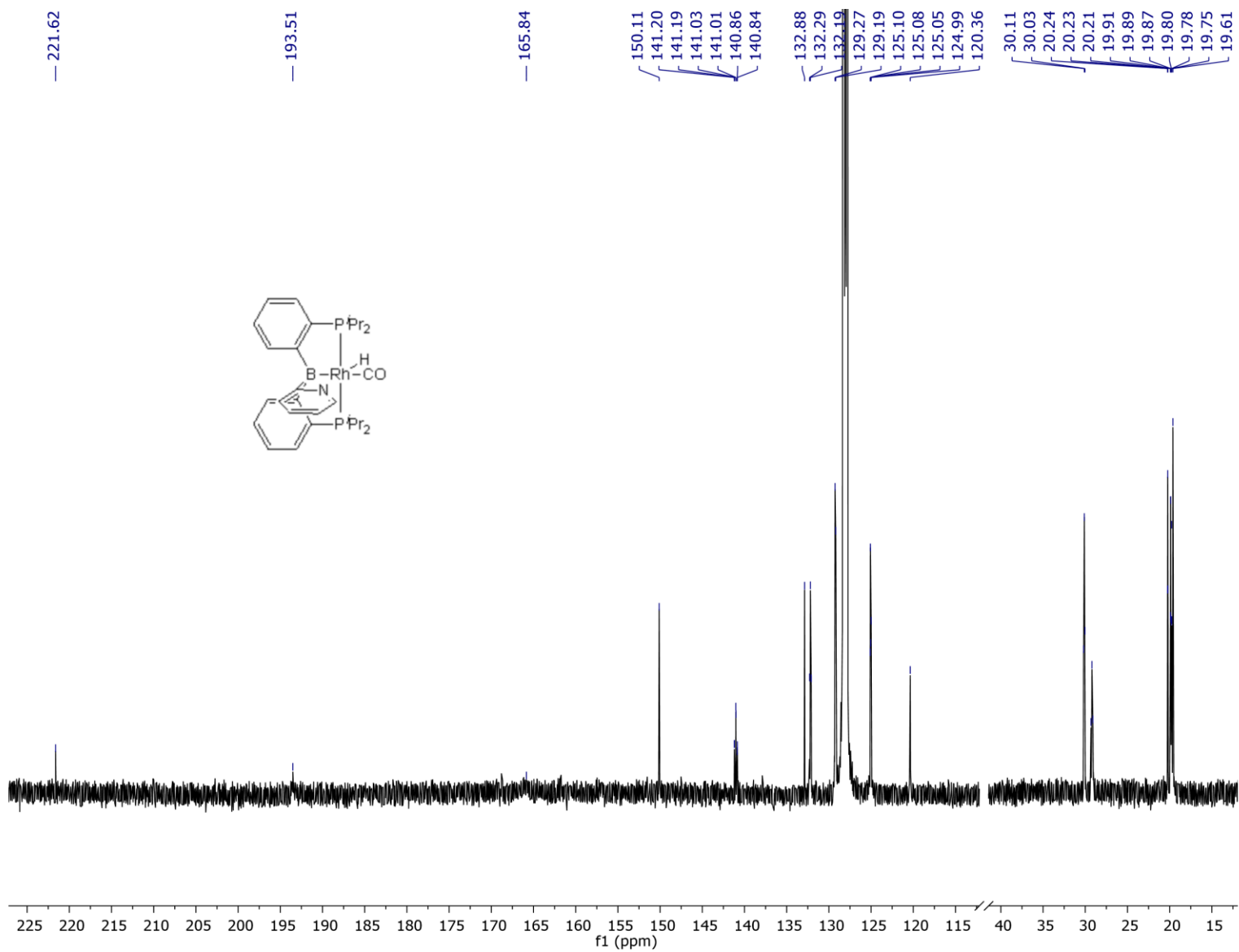


**Figure S29.**  $^{13}\text{C}\{^1\text{H}\}$  NMR spectrum of **3RhN** in  $\text{C}_6\text{D}_6$  measured on a 500 MHz Varian NMR

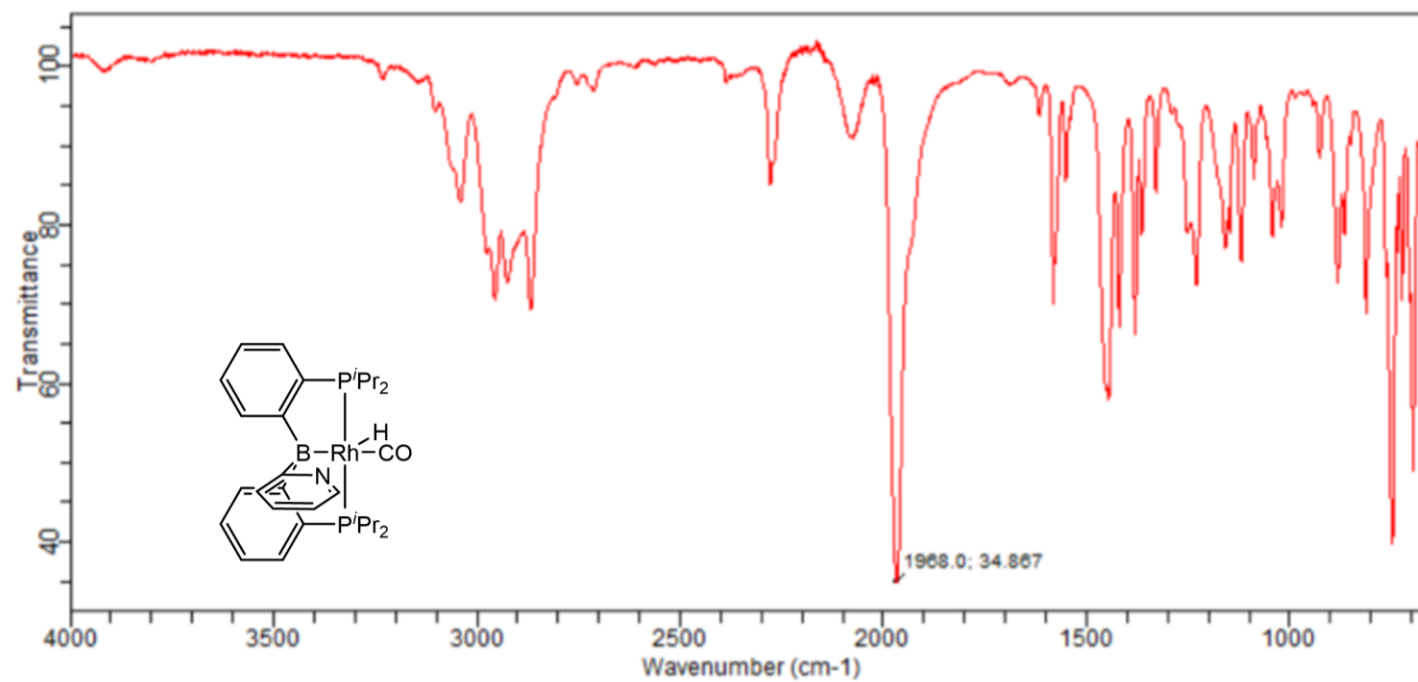


**Figure S30.** IR spectrum of **3RhN** measured on an Agilent ATR-IR spectrometer.

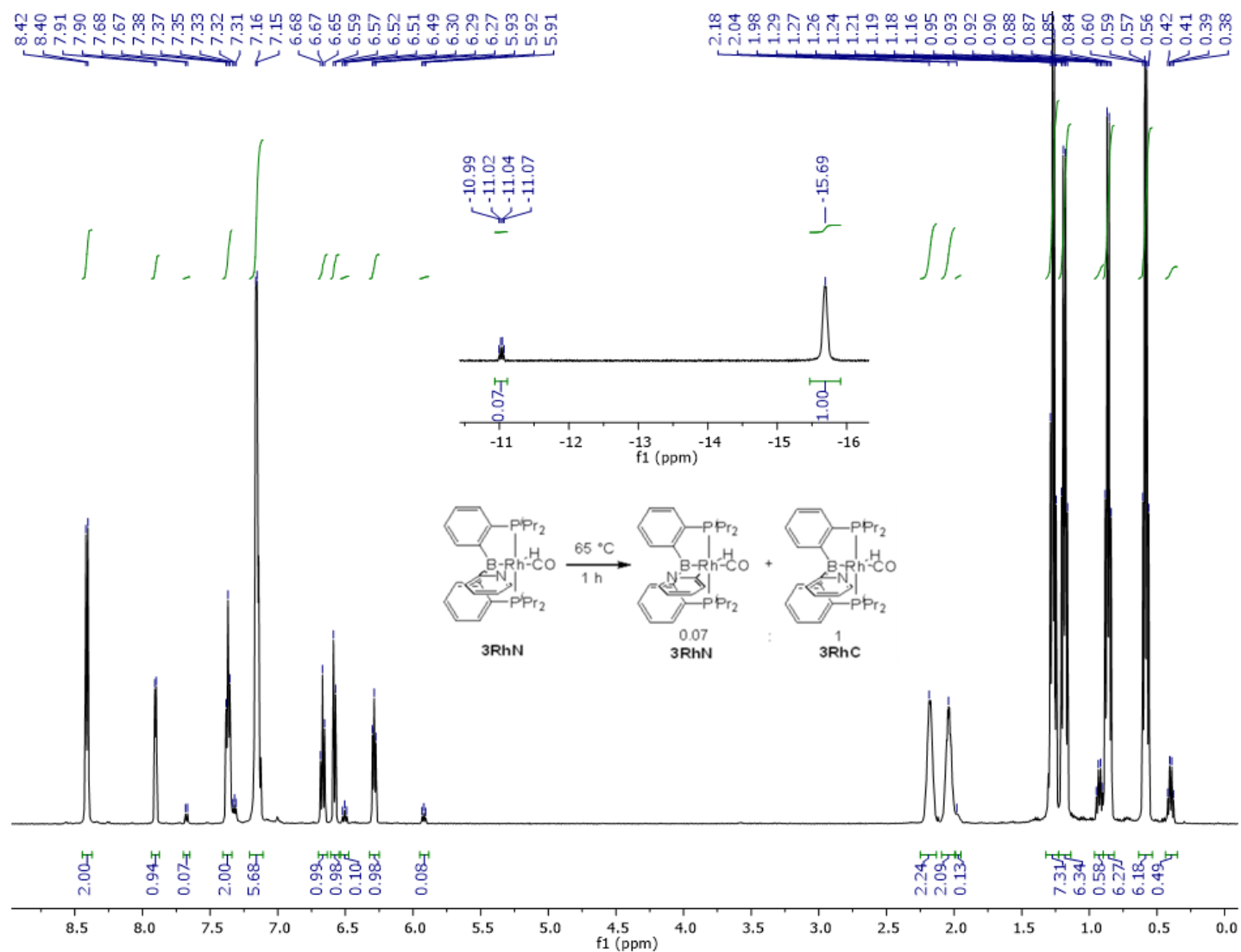


**Figure S31.**  $^1\text{H}$  NMR spectrum of **3RhN** in  $\text{C}_6\text{D}_6$  measured at room temperature on a 500 MHz Varian NMR after heating at  $65\text{ }^\circ\text{C}$  for 1 h. The sample contains a mixture of **3RhN**/**3RhC** (1:0.07)

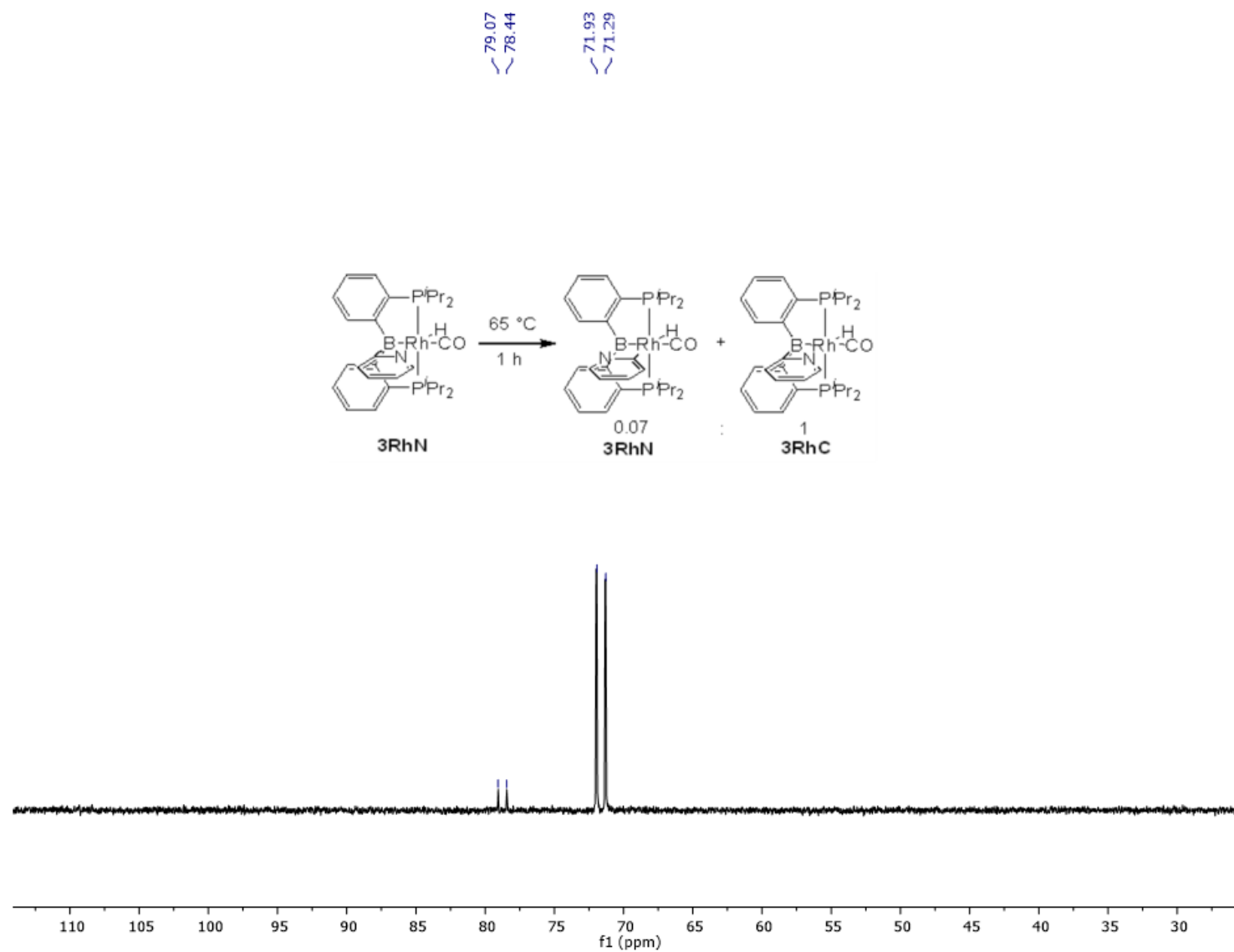


**Figure S32.**  $^{31}\text{P}\{^1\text{H}\}$  NMR spectrum of **3RhN** in  $\text{C}_6\text{D}_6$  measured at room temperature on a 500 MHz Varian NMR after heating at 65  $^\circ\text{C}$  for 1 h. The sample contains a mixture of **3RhN/3RhC** (1:0.07)

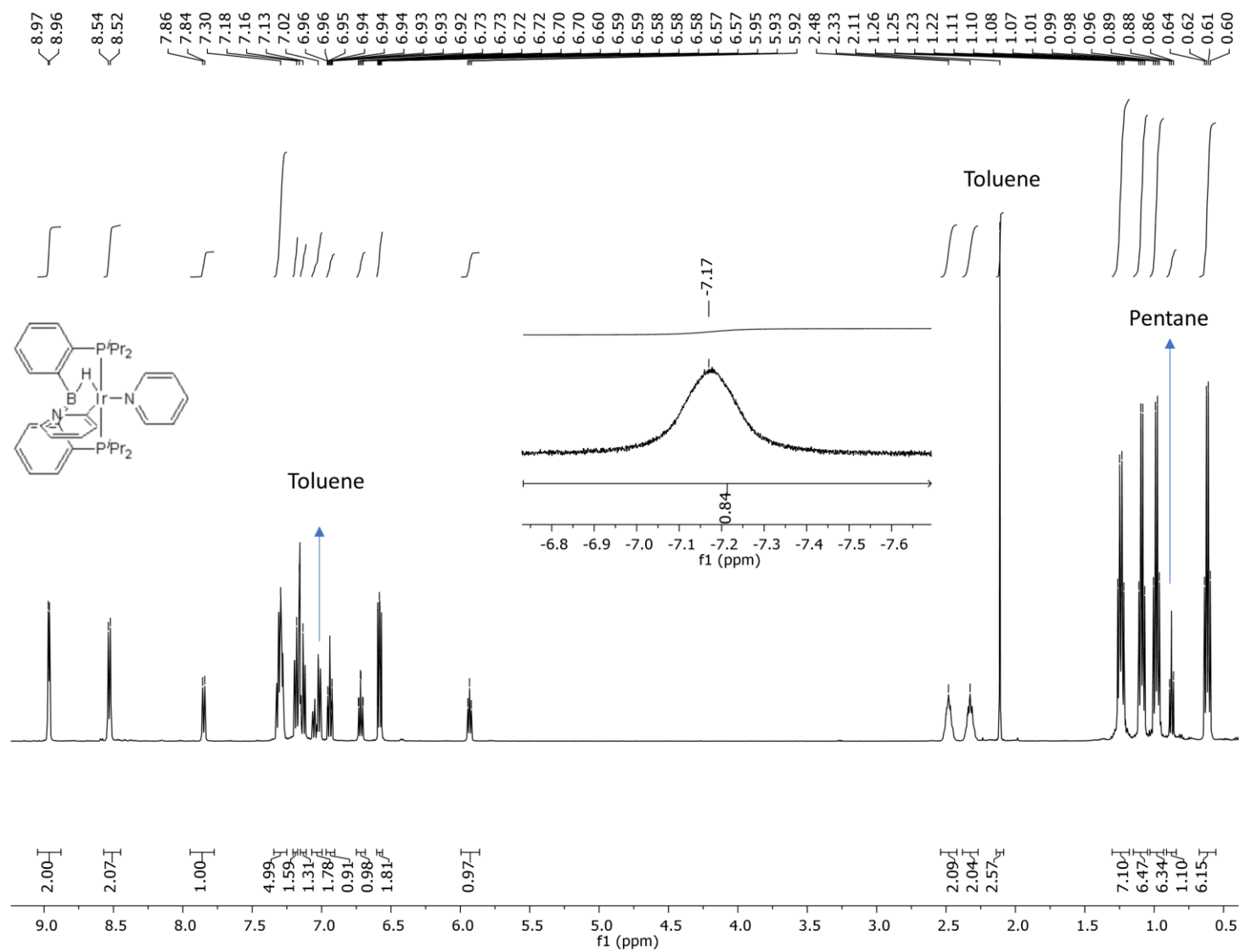


**Figure S33.** <sup>1</sup>H NMR spectrum of **7** in C<sub>6</sub>D<sub>6</sub> measured on a 500 MHz Varian NMR

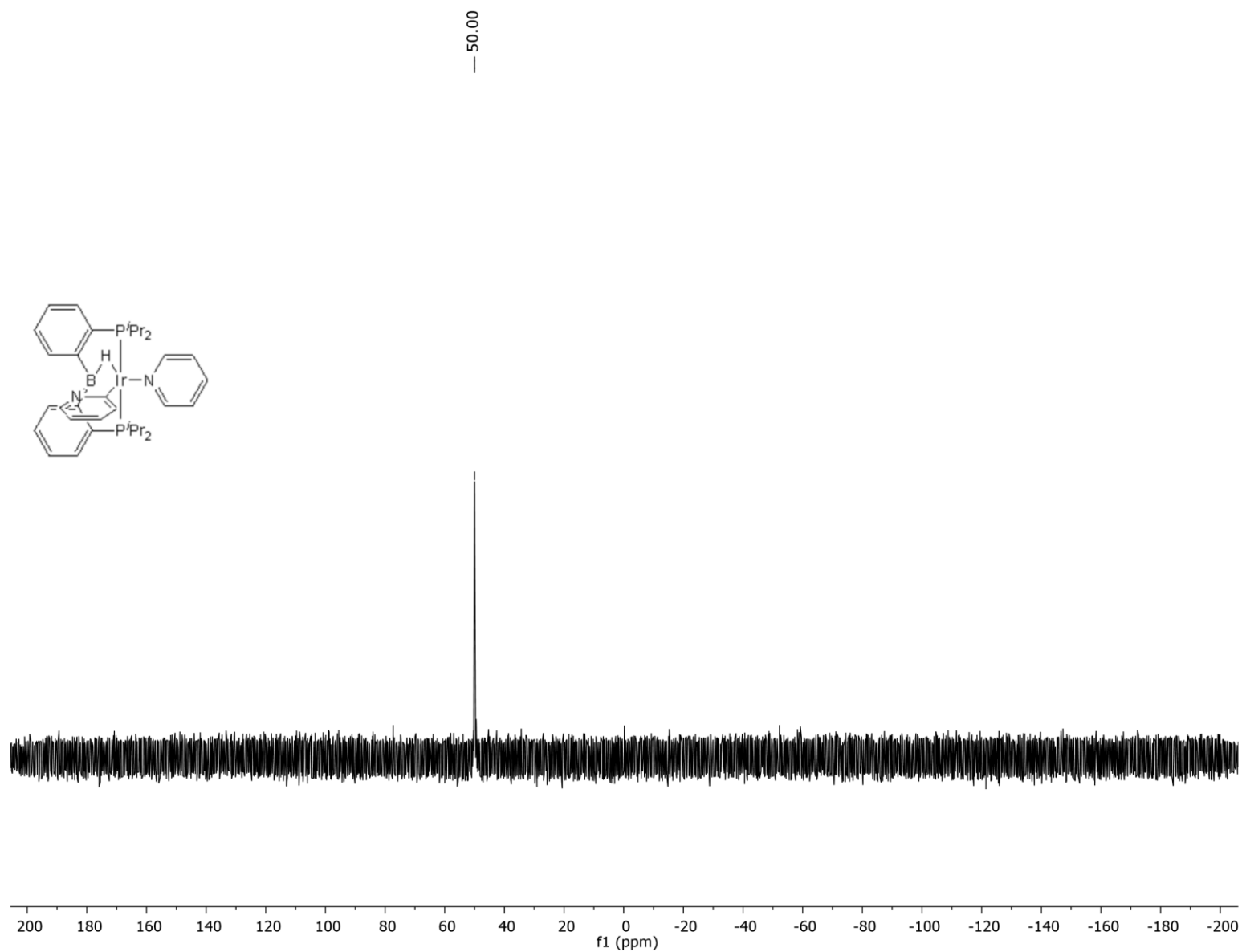


**Figure S34.**  $^{31}\text{P}\{^1\text{H}\}$  NMR spectrum of **7** in  $\text{C}_6\text{D}_6$  measured on a 500 MHz Varian NMR



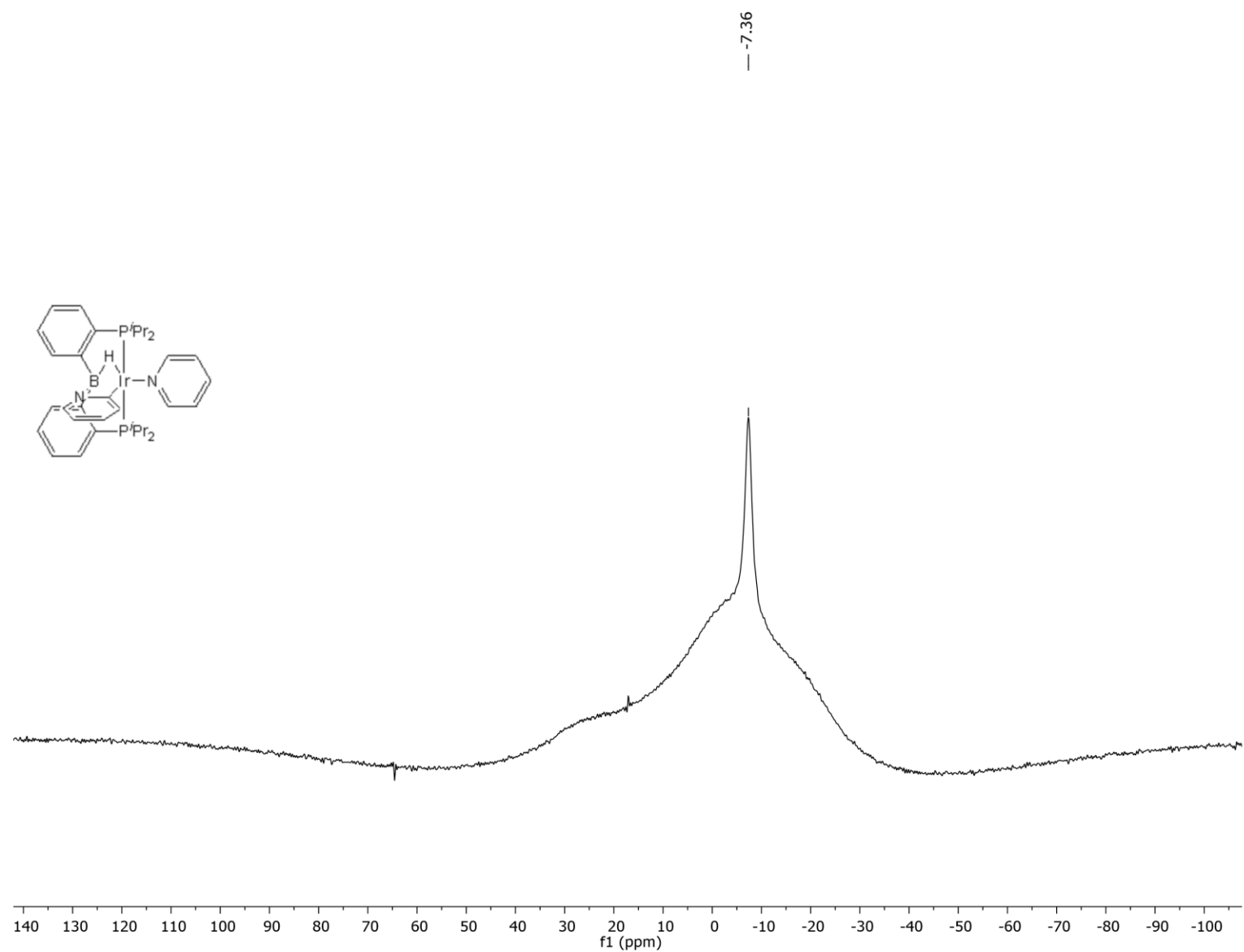
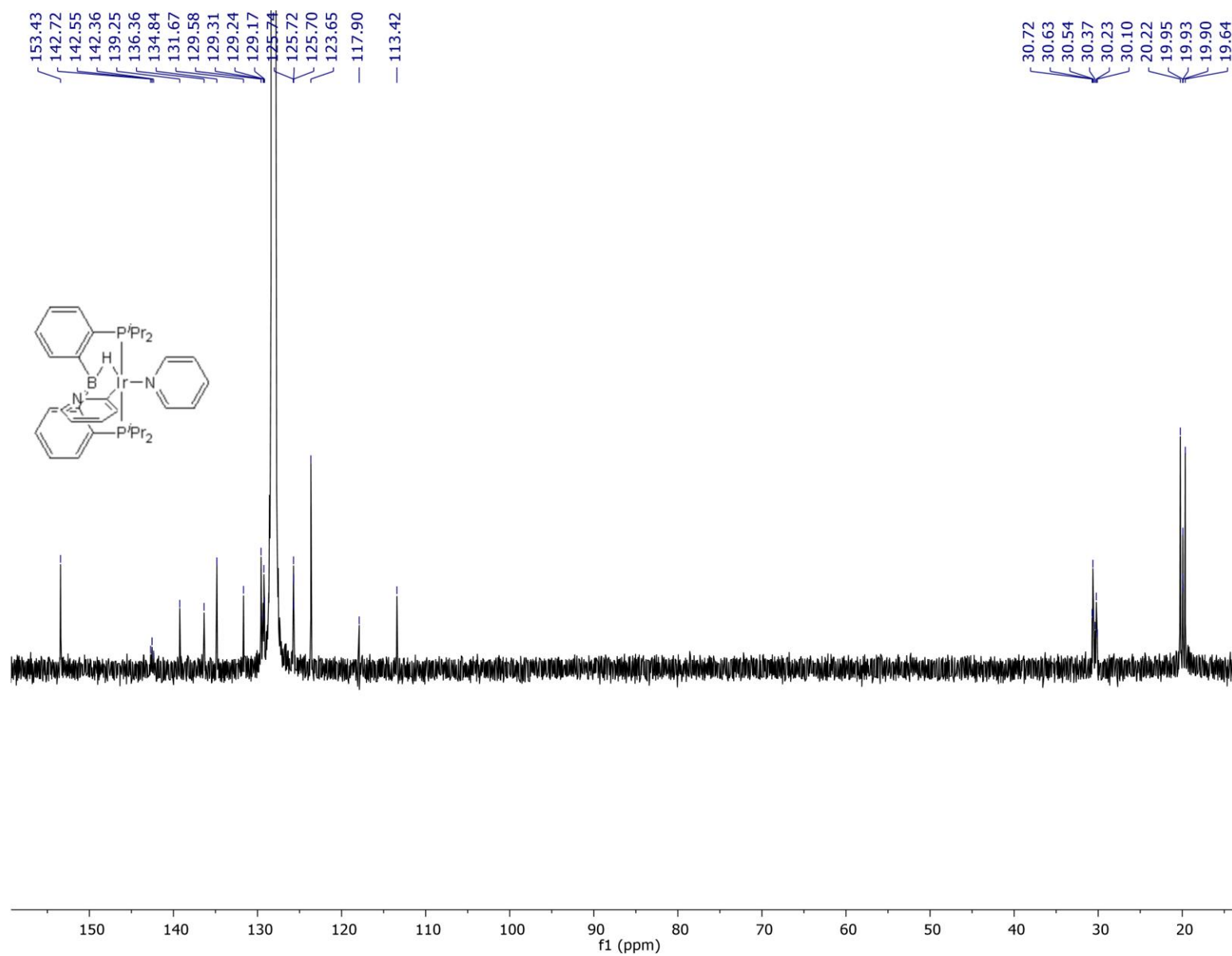


**Figure S35.**  $^{11}\text{B}\{^1\text{H}\}$  NMR spectrum of **7** in  $\text{C}_6\text{D}_6$  measured on a 400 MHz Bruker NMR



## 6. SI References.

- <sup>1</sup> W.-C. Shih, W. Gu, M. C. MacInnis, S. D. Timpa, N. Bhuvanesh, J. Zhou, and O. V. Ozerov, *J. Am. Chem. Soc.*, 2016, **138**, 2086-2089.
- <sup>2</sup> APEX2 “*Version 2 User Manual, M86-E01078*”, BRUKER AXS Inc., 5465 East Cheryl Parkway, Madison, WI 53711-5373 USA
- <sup>3</sup> SADABS, Sheldrick, G.M. “*Program for Absorption Correction of Area Detector Frames*”, BRUKER AXS Inc., 5465 East Cheryl Parkway, Madison, WI 53711-5373 USA.
- <sup>4</sup> (a) G. M. Sheldrick, *Acta Cryst.*, 2008, **A64**, 112-122. (b) G. M. Sheldrick, *Acta Cryst.*, 2015, **A71**, 3-8. (c) G. M. Sheldrick, *Acta Cryst.*, 2015, **C71**, 3-8. (d) XT, XS, BRUKER AXS Inc., 5465 East Cheryl Parkway, Madison, WI 53711-5373 USA.
- <sup>5</sup> A. L. Spek, *J. Appl. Crystallogr.*, 2003, **36**, 7–13.
- <sup>6</sup> APEX2 “*Program for Data Collection on Area Detectors*”, BRUKER AXS Inc., 5465 East Cheryl Parkway, Madison, WI 53711-5373 USA
- <sup>7</sup> O. V. Dolomanov, L. J. Bourhis, R. J. Gildea, J. A. K. Howard, and H. Puschmann, *H. J. Appl. Cryst.*, 2009, **42**, 339-341.
- <sup>8</sup> APEX3 “*Program for Data Collection on Area Detectors*” BRUKER AXS Inc., 5465 East Cheryl Parkway, Madison, WI 53711-5373 USA
- <sup>9</sup> L. J. Farrugia, *J. Appl. Cryst.*, 2012, **45**, 849.
- <sup>10</sup> POV-Ray Home page, <http://www.povray.org/>, (accessed December 2, 2020).
- <sup>11</sup> M. J. Frisch, G. W. Trucks, H. B. Schlegel, G. E. Scuseria, M. A. Robb, J. R. Cheeseman, G. Scalmani, V. Barone, B. Mennucci, G. A. Petersson, H. Nakatsuji, M. Caricato, X. Li, H. P.

Hratchian, A. F. Izmaylov, J. Bloino, G. Zheng, J. L. Sonnenberg, M. Hada, M. Ehara, K. Toyota, R. Fukuda, J. Hasegawa, M. Ishida, T. Nakajima, Y. Honda, O. Kitao, H. Nakai, T. Vreven, J. A. Montgomery, Jr., J. E. Peralta, F. Ogliaro, M. Bearpark, J. J. Heyd, E. Brothers, K. N. Kudin, V. N. Staroverov, R. Kobayashi, J. Normand, K. Radhachari, A. Rendell, J. C. Burant, S. S. Iyengar, J. Somasi, M. Cossi, N. Rega, N. J. Millam, M. Klene, J. E. Knox, J. B. Cross, V. Bakken, C. Adamo, J. Jaramillo, R. Gomperts, R. E. Stratmann, O. Yazyev, A. J. Austin, R. Cammi, C. Pomelli, J. W. Ochterski, R. L. Martin, K. Morokuma, V. G. Zakrzewski, G. A. Voth, P. Salvador, J. J. Dannenberg, S. Dapprich, A. D. Daniels, Ö. Farkas, J. B. Foresman, J. V. Ortiz, J. Cioslowski and D. J. Fox, Gaussian 09 (Revision D.01), Gaussian, Inc., Wallingford, CT, 2009.

<sup>12</sup> S. Grimme, S. Ehrlich, and L. Goerigk, *L. J. Comp. Chem.*, 2011, **32**, 1456-1465.

<sup>13</sup> M. P. Mitoraj, A. Michalak, and T. A. Ziegler, *J. Chem. Theory Comput.*, 2009, **5**, 962-975.

<sup>14</sup> F. Neese, *WIREs Comput. Mol. Sci.* 2018, **8**, e1327.

<sup>15</sup> T. Lu, and F. Chen, *J. Comput. Chem.*, 2012, **33**, 580–592.